

Electronic Supplementary Information

Self-Assembly of Metal–Organosilicate on Porous Silica Substrates for Efficient CO₂ Hydrogenation to Methanol

Yu Shao and Hua Chun Zeng*

Integrative Sciences and Engineering Program, NUS Graduate School and Department of Chemical and Biomolecular Engineering, College of Design and Engineering, National University of Singapore, 10 Kent Ridge Crescent, Singapore 119260

*Email: chezhc@nus.edu.sg

Table of Contents

Supporting Tables (Table S1 and Table S2)	Page S-2 to S-3
Supporting Figures (Figure S1 to Figure S61).....	Page S-4 to S-53
References	Page S-53 to S-54

Table S1. Detailed Synthetic Parameters in Supplement to Sections 2.3 and 2.4 and Their ICP-OES Measurement Results.

Entry No.	Sample Denotation	Synthetic Parameters		ICP-OES Results	
	MSS-SiRNH ₂ -Cu	Cu(NO ₃) ₂ ·3H ₂ O (Section 2.3)	Zn(NO ₃) ₂ ·6H ₂ O (Section 2.4)	Cu (wt %)	Zn (wt %)
1	MSS-SiRNH ₂ -Cu	80	-	3.4	-
2	MSS-SiRNH ₂ -Cu	160	-	4.5	-
3	MSS-SiRNH ₂ -Cu	240	-	3.8	-
4	MSS-SiRNH ₂ -Cu	320	-	6.2	-
5	MSS-SiRNH ₂ -Cu	400	-	6.1	-
	MSS-Si-Cu-Zn				
6	MSS-Si-4.6Cu-0.0Zn	160	0	4.6	0
7	MSS-Si-4.7Cu-3.2Zn	160	50	4.7	3.2
8	MSS-Si-4.3Cu-4.6Zn	160	250	4.3	4.6
9	MSS-Si-3.8Cu-5.5Zn	160	500	3.8	5.5
10	MSS-Si-3.2Cu-6.0Zn	160	750	3.2	6.0
11	MSS-Si-2.6Cu-6.7Zn	160	1000	2.6	6.7
12	MSS-Si-2.2Cu-6.7Zn	160	1250	2.2	6.7
13	MSS-Si-2.5Cu-6.1Zn	80	750	2.5	6.1
14	MSS-Si-2.4Cu-5.3Zn	240	750	2.4	5.3
15	MSS-Si-4.0Cu-4.2Zn	320	750	4.0	4.2
16	MSS-Si-4.1Cu-3.5Zn	400	750	4.1	3.5

Table S2. Summary of specific MeOH yields of different CuZn/SiO₂ catalysts.

Catalyst ^{Ref}	Temperature (°C)	Pressure (bar)	Space Velocity*	MeOH Yield (mg _{MeOH} ·g _{Cu} ⁻¹ ·h ⁻¹)
Cu/ZnO@m-SiO ₂ ¹	240	30	(W) 6000	1163
Cu/ZnO/SiO ₂ ²	220	30	(W) 2000	242
CuZnO/SiO ₂ ³	240	30	(W) 18000	73
CuZnO/mSiO ₂ ³	240	30	(W) 18000	210
CuZnO/MVmSiO ₂ ³	240	30	(W) 18000	460
CuO-ZnO/SiO ₂ ⁴	250	30	(G) 3600	2069
CuO-ZnO/SiO ₂ ⁴	250	30	(G) 3600	1406
Zn ₄₃ -CuSiNT ⁵	240	30	(W) 9600	391
Zn ₃₄ -CuSiNT ⁵	240	30	(W) 9600	370
CuZnSi-StM ⁶	240	20	(W) 4000	75
CuZnSi-SGM ⁶	240	20	(W) 4000	317
CuZnSi-AEM ⁶	240	20	(W) 4000	567
CuZn-350 ⁷	230	30	(W) 38000	725
Cu-Zn/SiO ₂ ⁸	230	25	(W) 24000	1600
CuZn/Al ₂ O ₃ ⁹	250	40	(W) 20400**	51
CuZn/SiO ₂ ⁹	250	40	(W) 20400**	22
AE-Cu/SiO ₂ ¹⁰	250	30	(G) 2040	132
FSP-Cu/SiO ₂ ¹⁰	250	30	(G) 2040	234
5Cu-1CyZn-5s/SiO ₂ ¹¹	250	40	(W) 9600	240
5Cu-1CyZn-30s/SiO ₂ ¹¹	250	40	(W) 9600	341
5Cu-5CyZn-5s/SiO ₂ ¹¹	250	40	(W) 9600	156
Cu/ZnO/Al₂O₃ (This work)	240	30	(W) 15000	256
MSS-2.7Cu4.0Zn (This work)	240	30	(W) 15000	456
MSS-Si-3.2Cu-6.0Zn (This work)	240	30	(W) 15000	823
MSS-Si-2.2Cu-6.7Zn (This work)	240	30	(W) 15000	1224

* (W) denotes Weight Hourly Space Velocity (WHSV, mL·g_{cat}⁻¹·h⁻¹).

(G) denotes Gas Hourly Space Velocity (GHSV, h⁻¹).

H₂:CO₂ ratio in feed gas is 3:1.

** Feed gas is 10% CO, 4% CO₂, 72% H₂, and 14% He.

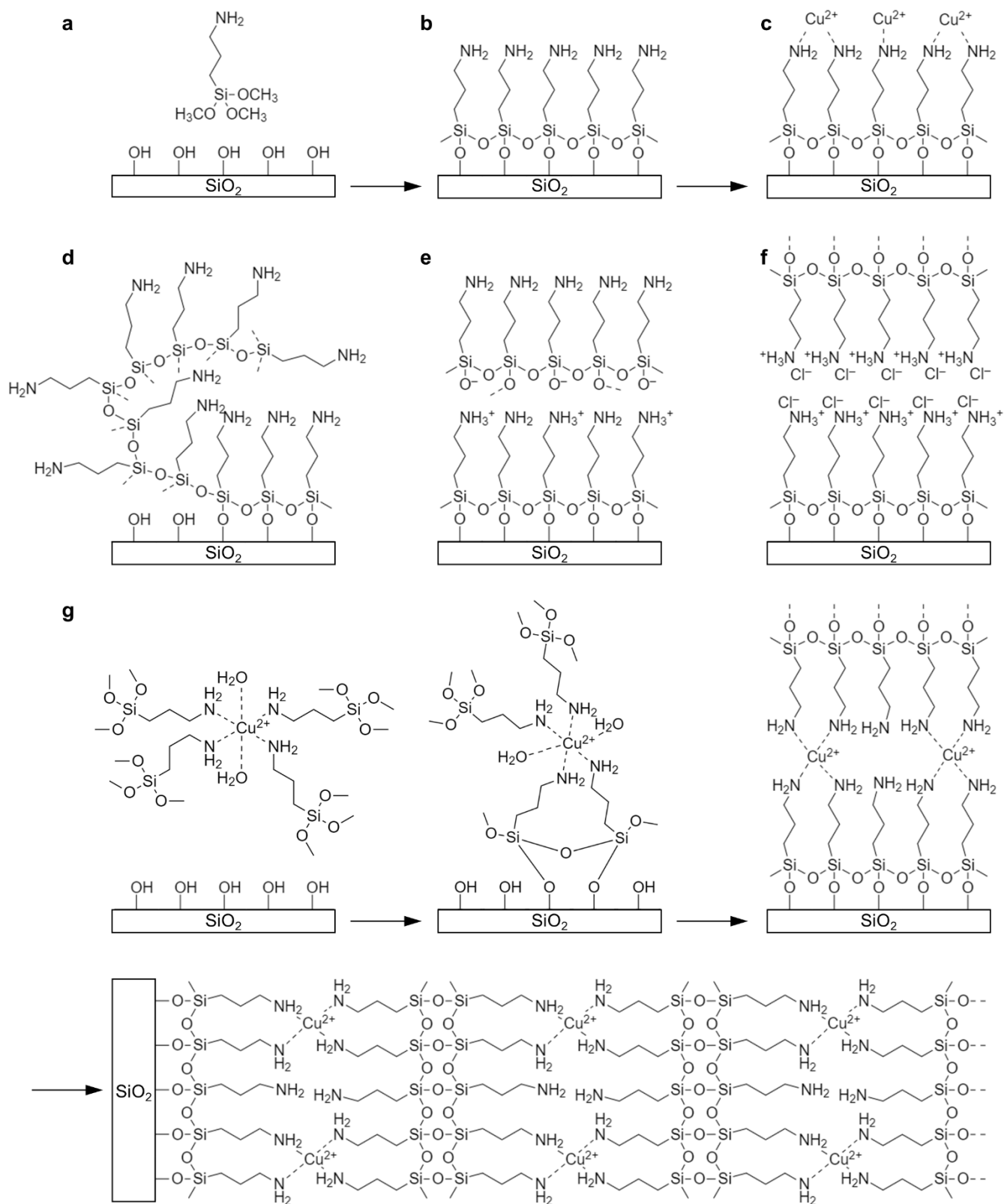


Figure S1. Schematic illustration of APTMS self-assembly on silica substrates. (a, b) Self-assembled monolayer under anhydrous conditions. (c) Incipient wetness impregnation of Cu^{2+} facilitated by APTMS monolayer. (d) APTMS polymerization into “mounds” under moist conditions. (e) Self-assembled multilayer with “head-to-tail” configuration. (f) Self-assembled multilayer with “head-to-head” configuration. (g) Self-assembly from Cu^{2+} -amine complexes into multilayered structure.

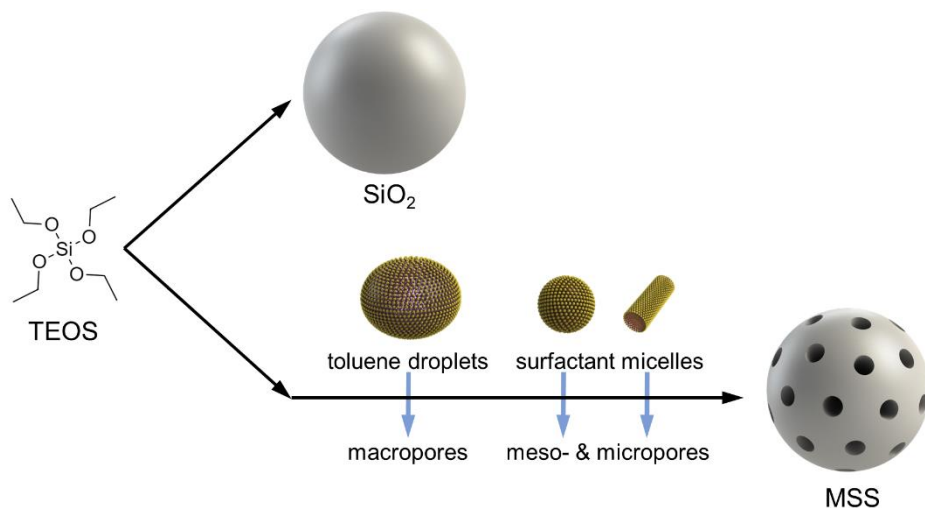


Figure S2. Schematic illustration of the syntheses of SiO₂ and MSS supports.

Synthetic Procedures for Stöber SiO₂ NS: The synthetic procedure was adopted from one of our previous studies,¹² with appropriate modifications to yield SiO₂ NS with similar dimension to the prepared MSS. In a typical synthesis, 16 mL of 25 wt % NH₃ aq solution was mixed with 90 mL of ethanol and stirred for 5 min. 5 mL of TEOS was added under stirring and the mixture was further stirred for another 4 h. The product was collected via centrifugation and washed with ethanol twice. The sample was then dried in an electric oven at 60 °C overnight.

Synthetic Procedures for MSS: Please refer to Section 2.2 of the main text.

Comment: Rigid SiO₂ spheres are prepared via a typical Stöber process. The macro-, meso-, and micropores in MSS are resultant from CTAB-stabilized toluene droplets and ethanol micelles.

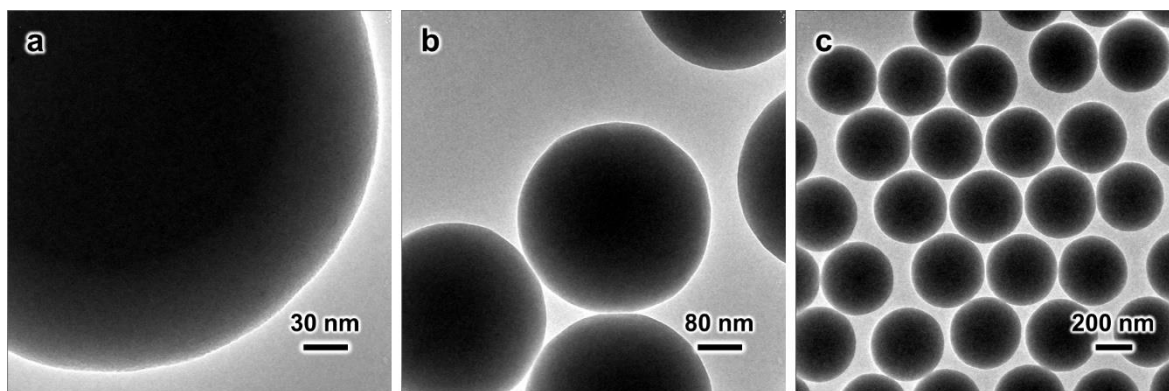


Figure S3. (a–c) TEM images of Stöber SiO₂ NS.

Comment: Rigid SiO₂ NS were prepared into comparable dimensions (*ca.* 500 nm diameter) of the MSS after the calcination treatment, to facilitate our subsequent comparison with MSS supported nanocatalysts.

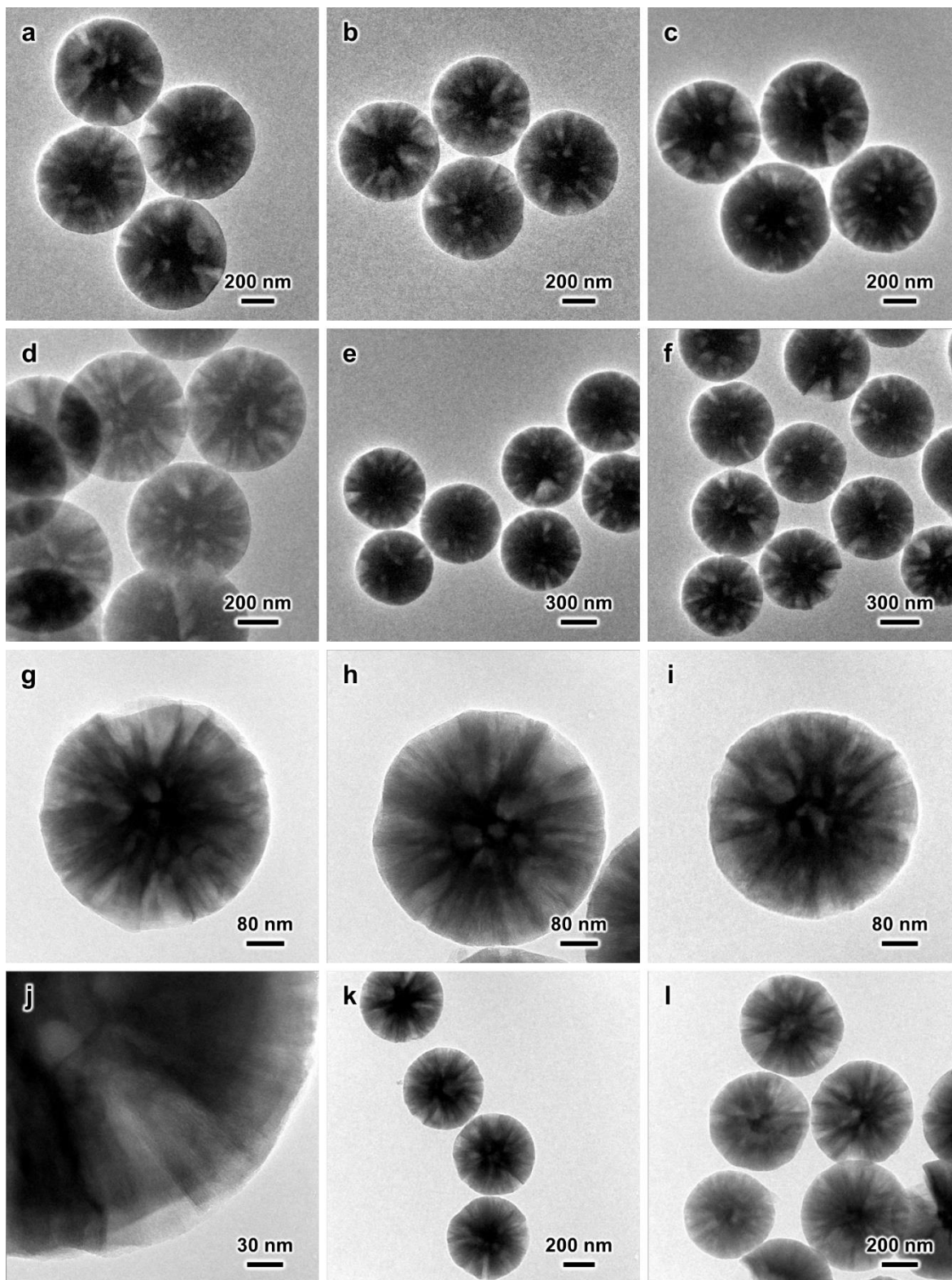


Figure S4. TEM images of (a-f) the prepared MSS (raw) before calcination and (g-l) the prepared MSS after calcination.

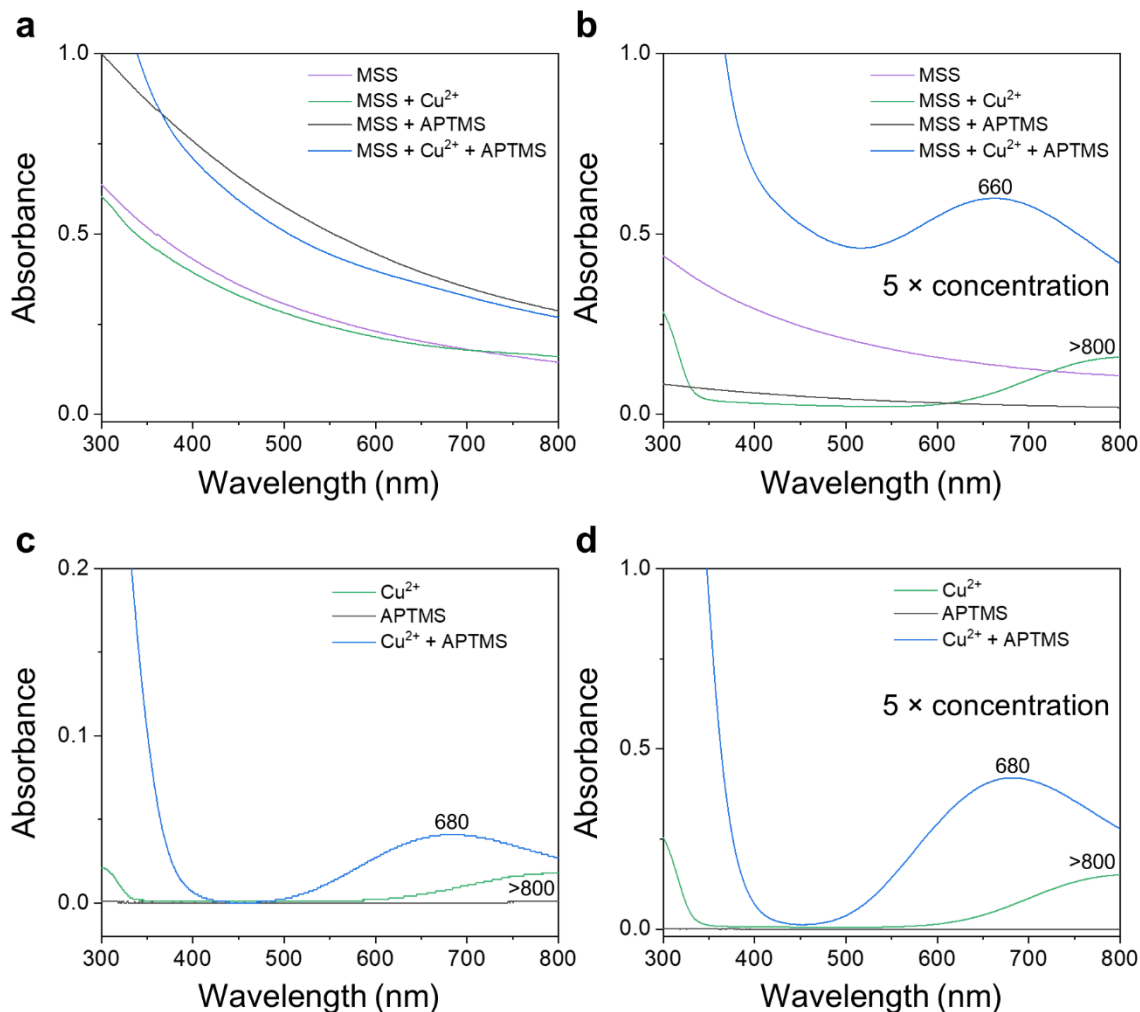


Figure S5. (a–d) UV–Vis spectra of $\text{Cu}(\text{NO}_3)_2$, APTMS, and MSS in the $\text{H}_2\text{O}/\text{EtOH}$ mixture.

Comment: Spectra in (a) were measured at substrate concentrations similar to the synthesis of MSS–SiRNH₂–Cu; spectra in (b) were measured with 5 times of concentration of Cu^{2+} and APTMS; similar measurements are performed in absence of MSS nanoparticles, with original (c) and 5 times (d) substrate concentrations, respectively.

In Figure S5a, the absorbances observed are attributed to suspended MSS nanoparticles and no absorbance due to Cu^{2+} and APTMS can be distinguished due to their relatively low concentrations.

In Figure S5b, after increasing the $\text{Cu}(\text{NO}_3)_2$ and APTMS to 5 times the original concentrations, the MSS + APTMS mixture exhibits minimal difference to the MSS suspension. A characteristic absorbance band (>800 nm) for $[\text{Cu}(\text{H}_2\text{O})_6]^{2+}$ complex is observed in the MSS + Cu^{2+} mixture. A blue shift to 660 nm is detected in the MSS + Cu^{2+} + APTMS mixture, due to the ligand exchange and formation of $[\text{Cu}(\text{RNH}_2)_x(\text{H}_2\text{O})_{6-x}]^{2+}$ ($2 \leq x \leq 4$) complex.^{13, 14}

To discard the influence of suspended MSS nanoparticles, similar measurements were performed in absence of MSS (Figure S5c, d). The same blue shift can be observed with better visual clarity, signifying the transition from $[\text{Cu}(\text{H}_2\text{O})_6]^{2+}$ to $[\text{Cu}(\text{RNH}_2)_x(\text{H}_2\text{O})_{6-x}]^{2+}$ ($2 \leq x \leq 4$).^{13, 14}

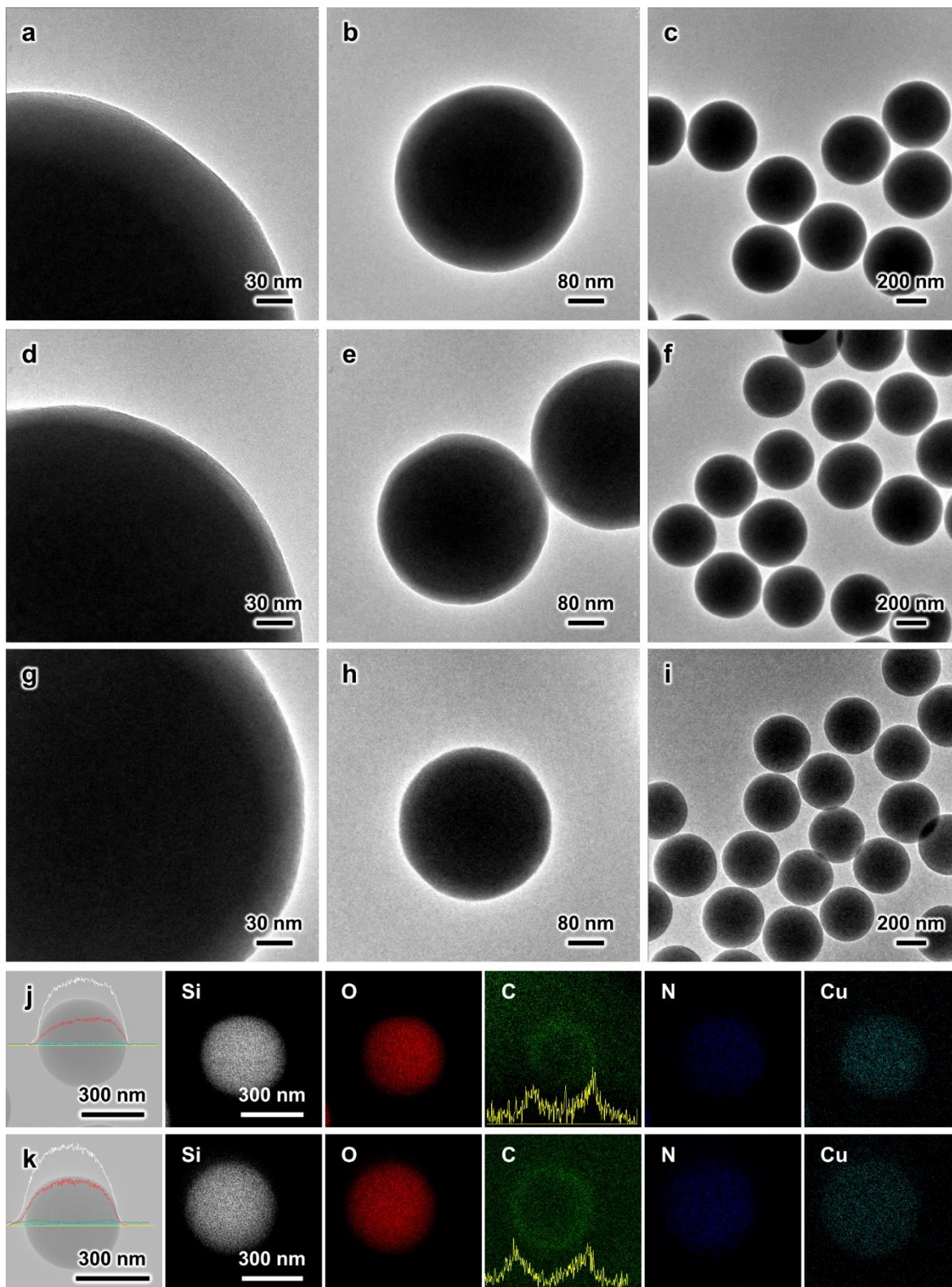


Figure S6. (a-i) TEM images of $\text{SiO}_2\text{-SiRNH}_2\text{-Cu}$ samples prepared with 3 different synthetic protocols (will be discussed on the next page). (j, k) The corresponding EDX elemental mappings of $\text{SiO}_2\text{-SiRNH}_2\text{-Cu}$ samples prepared with 2 of the 3 synthetic protocols. Color codes: white represents silicon, red represents oxygen, blue represents nitrogen, cyan represents copper, and orange represents zinc.

Synthetic Procedures for SiO₂-SiRNH₂-Cu:

Protocol A (Figure S6a-c): The synthesis process is in general the same as that described in Section 2.3, except that SiO₂ NS was used instead of MSS. 400 mg of SiO₂ NS was dispersed in 50 mL of deionized water via ultrasonication. 160 mg of Cu(NO₃)₂·3H₂O was dissolved into another 50 mL of deionized water. The SiO₂ NS suspension and Cu(NO₃)₂ solution were then added to 100 mL of deionized water and 160 mL of ethanol inside a 500 mL round-bottom flask. The mixture was heated at 55 °C for 15 min and 520 μL of APTMS was subsequently added. The mixture was further heated at 55 °C with stirring for another 20 h. The product was collected via centrifugation and washed with ethanol three times. The sample was then dried in an electric oven at 60 °C overnight.

Protocol B (Figure S6d-f, j): The synthetic process was the same as *protocol A* except that 2 mL of 25 wt % NH₃ aq solution was added. 400 mg of SiO₂ NS was dispersed in 50 mL of deionized water via ultrasonication. 160 mg of Cu(NO₃)₂·3H₂O was dissolved into another 50 mL of deionized water. The SiO₂ NS suspension and Cu(NO₃)₂ solution were then added to 80 mL of ethanol inside a 500 mL round-bottom flask. The mixture was heated at 55 °C for 15 min and 520 μL of APTMS was subsequently added. 2 mL of 25 wt % NH₃ aq solution was added after stirring the mixture for 5 min. The mixture was further heated at 55 °C with stirring for another 20 h. The product was collected via centrifugation and washed with ethanol three times. The sample was then dried in an electric oven at 60 °C overnight.

Protocol C (Figure S6g-i, k): The SiO₂ NS was added in 10 times amount compared to that in *protocol A*. 4000 mg of SiO₂ NS was dispersed in 50 mL of deionized water via ultrasonication. 160 mg of Cu(NO₃)₂·3H₂O was dissolved into another 50 mL of deionized water. The SiO₂ NS suspension and Cu(NO₃)₂ solution were then added to 100 mL of deionized water and 160 mL of ethanol inside a 500 mL round-bottom flask. The mixture was heated at 55 °C for 15 min and 520 μL of APTMS was subsequently added. The mixture was further heated at 55 °C with stirring for another 20 h. The product was collected via centrifugation and washed with ethanol three times. The sample was then dried in an electric oven at 60 °C overnight.

Comments: As discussed in Section 3.1, we attempted the self-assembly/synthesis of the SiRNH₂-Cu phase on rigid SiO₂ NS with three different synthetic protocols. *Protocol A* was identical to the synthetic procedure applied to MSS substrates (Section 2.3). However, it only yielded a low SiRNH₂-Cu content (0.32 wt % Cu, Figure S6a-c). It is attributed to the low surface area of SiO₂ NS (8.7 m²·g⁻¹), in comparison to MSS (774 m²·g⁻¹).

We repeated the synthesis with the addition of ammonia solution to promote the polycondensation (*Protocol B*, Figure S6d-f). As revealed by EDX elemental mapping and line scan (Figure S6j), a SiRNH₂-Cu shell clearly forms after the addition of ammonia solution. However, the Cu content is similar to *Protocol A*, at a low level of 0.35 wt %. Thus, addition of ammonia solution does trigger the polycondensation of APTMS. Nonetheless, the polycondensation resulted in formation of an organosilica shell with very low Cu content, instead of the desired metal-organosilicate.

Considering the huge difference in surface area between MSS (774 m²·g⁻¹) and SiO₂ NS (8.7 m²·g⁻¹), we then propose that the abundant surface silanol groups of MSS shall be responsible of facilitating the shell formation. In this regard, *Protocol C* employed 10 times the amount of SiO₂ NS and SiRNH₂-Cu phase could be loaded up to 0.74 wt % Cu (Figure S6d-f). The SiRNH₂-Cu shell could be clearly identified with EDX (Figure S6k). Thus, the coating process of SiRNH₂-Cu is strongly related to the surface area of the substrate.

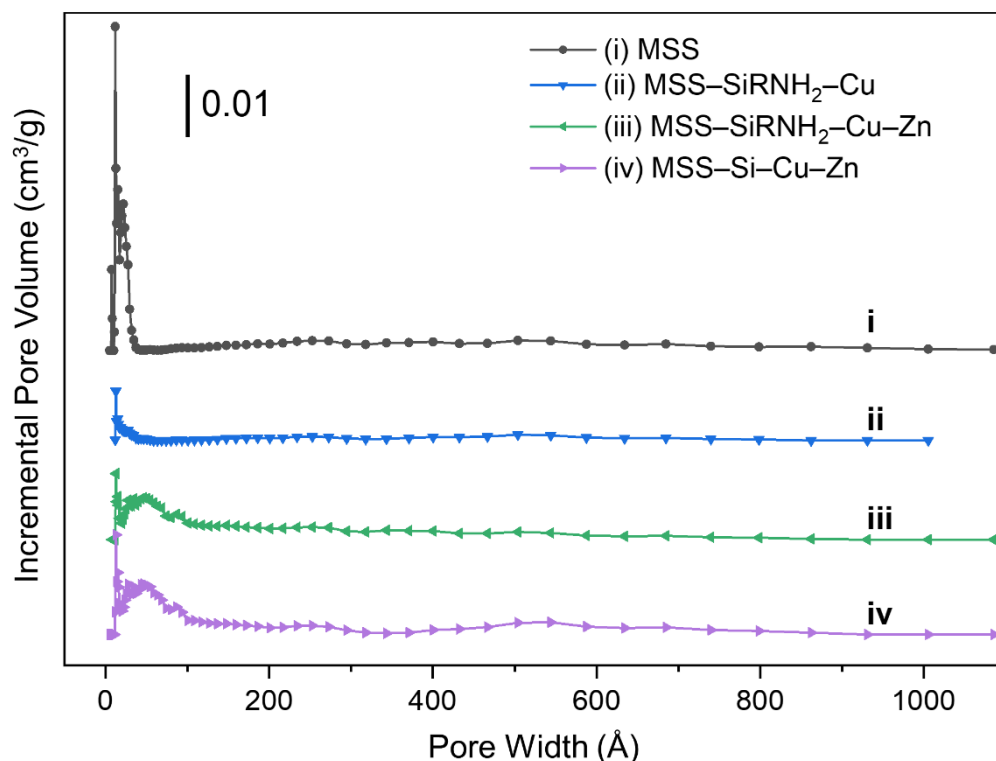


Figure S7. Full-scale (0–1000 Å) NLDFT pore size distribution of MSS, MSS–SiRNH₂–Cu, MSS–SiRNH₂–Cu–Zn, and MSS–Si–Cu–Zn.

Comment: Figure S7 presents the full-scale NLDFT calculated pore size distribution of MSS, MSS–SiRNH₂–Cu, MSS–SiRNH₂–Cu–Zn, and MSS–Si–Cu–Zn, which were zoomed in to certain region in the main text to emphasize on specific features (Figure 2b, c).

It is obvious that the pristine MSS support possesses the highest amount of pore structures, which has an estimated BET surface area of 774 m²·g⁻¹.

Upon coating with the SiRNH₂–Cu shell, the surface texture was largely replaced and represented by the SiRNH₂–Cu phase, leading to significantly diminished micropores and small mesopores (<5 nm). Larger pores, however, were mostly retained as the thin layer was coated along the shell walls. Nevertheless, it resulted in a considerable decrease in the surface area to 96 m²·g⁻¹.

Introduction of Zn species via heat treatment led to an increment in the surface area (236 m²·g⁻¹). As some of the Zn²⁺ was taken up by the SiRNH₂–M phase, the remainder ended up as hydroxides on the surface and decomposed into ZnO nanoparticles due to the heat applied. A mesopore peak located around 4.7 nm emerged during this step, which were inferred to be the slit-shaped voids enclosed between nanoparticles.

The final calcination step led to another increment in the surface area (349 m²·g⁻¹) and the micropore volume. As discovered by our previous study and illustrated in Scheme 1a, the SiRNH₂–M phase takes a laminar structure and the gallery space turned into slit-shape micropores upon the removal of alkylamine ligands by calcination.¹⁵

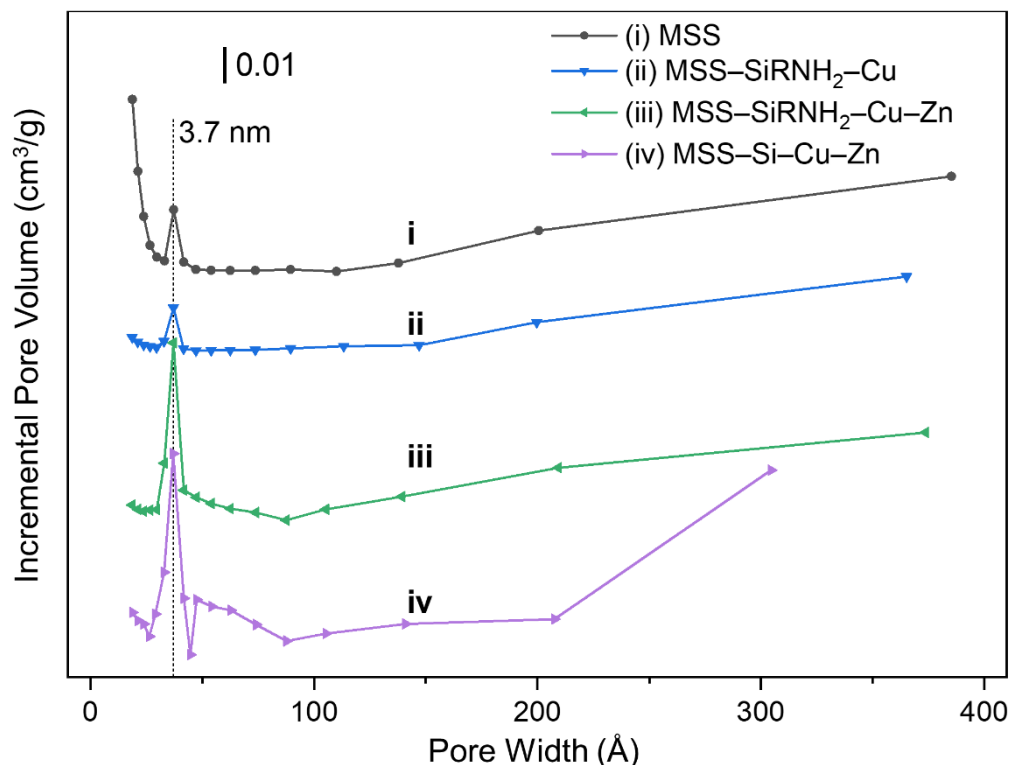


Figure S8. Pore size distribution calculated with BJH method on desorption data for MSS, MSS-SiRNH₂-Cu, MSS-SiRNH₂-Cu-Zn, and MSS-Si-Cu-Zn samples.

Comment: As mentioned in the main text discussion (Figure 2), for the MSS support and derived supported nanocatalyst possessing a hierarchical macro-meso-micropore structure, traditional BJH method fails to cover the wide range of pore dimension compared to NLDFT method. Nevertheless, we present the BJH method estimated pore size distribution in complementary. Similarly, it suggests that the pristine MSS owns the highest amount of micropores and the micropore volume increased upon calcination, in agreement to our discussion in Section 3.2 and Figure S7. In addition, based on the evident Type H4 hysteresis loop presented in all the N₂ physisorption isotherms (Figure 2a), it indicates a unimodal mesopore structure with pore width of 3.7 nm, and similar increased mesopore volume observed in MSS-SiRNH₂-Cu-Zn, and MSS-Si-Cu-Zn samples (Figure S7).

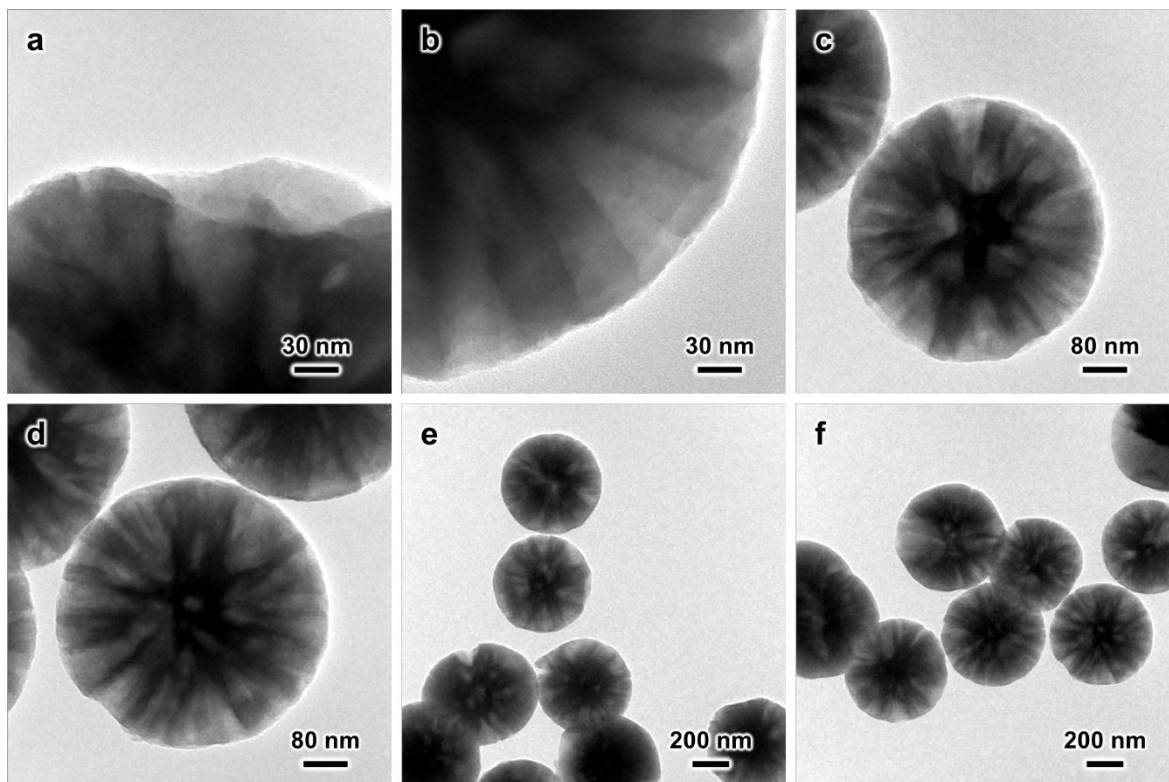


Figure S9. (a-f) TEM images of the synthesized MSS-SiRNH₂-Cu prepared according to Table S1, entry 1.

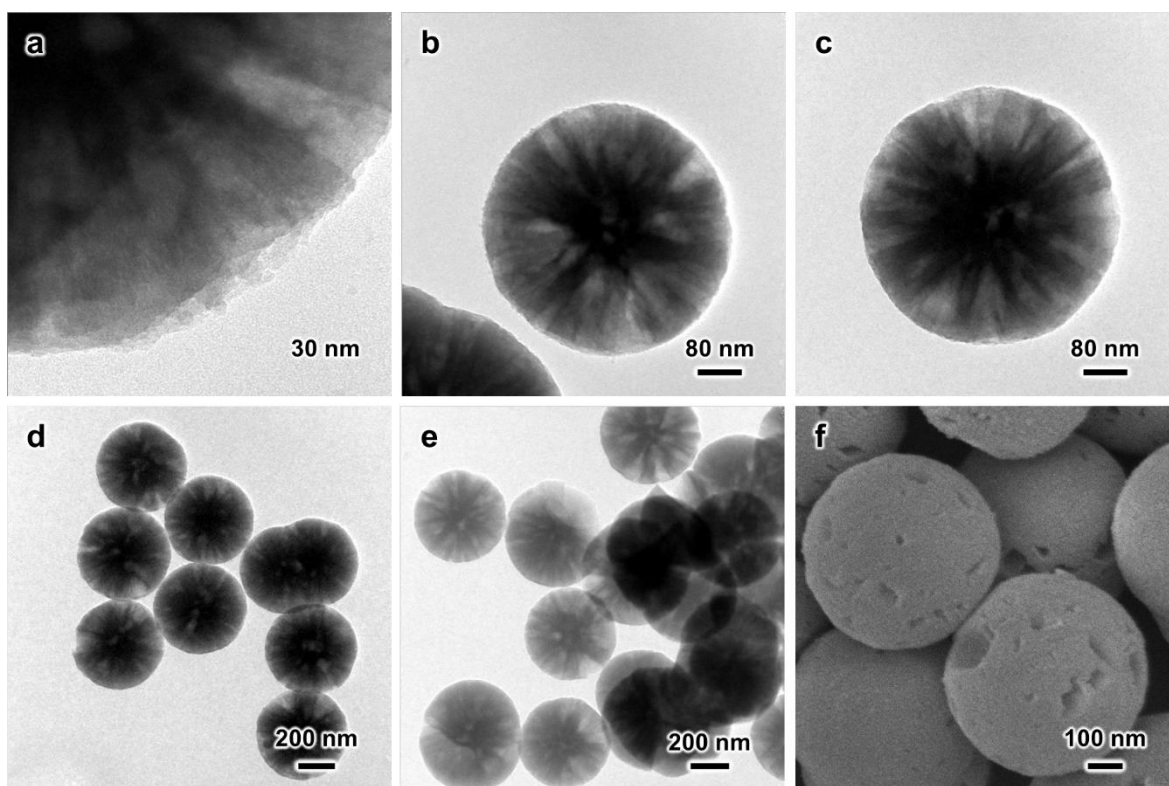


Figure S10. (a-e) TEM and (f) SEM images of the synthesized MSS-SiRNH₂-Cu prepared according to Table S1, entry 2.

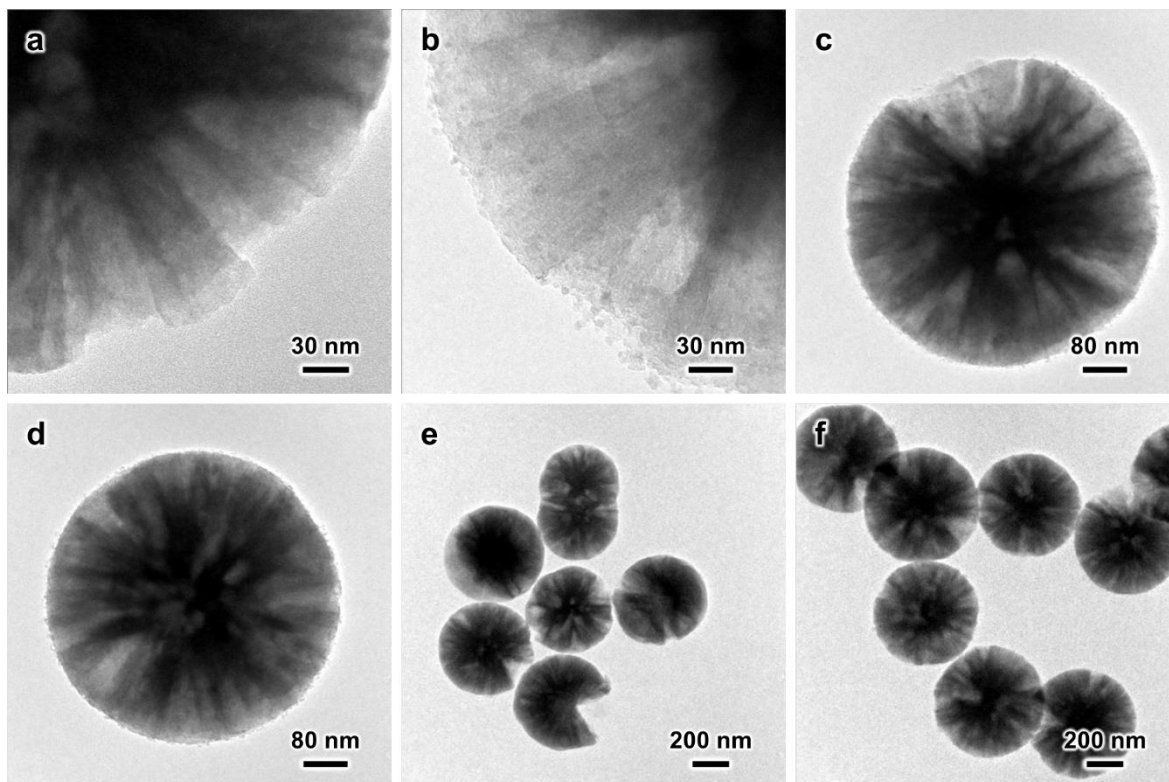


Figure S11. (a-f) TEM images of the synthesized MSS-SiRNH₂-Cu prepared according to Table S1, entry 3.

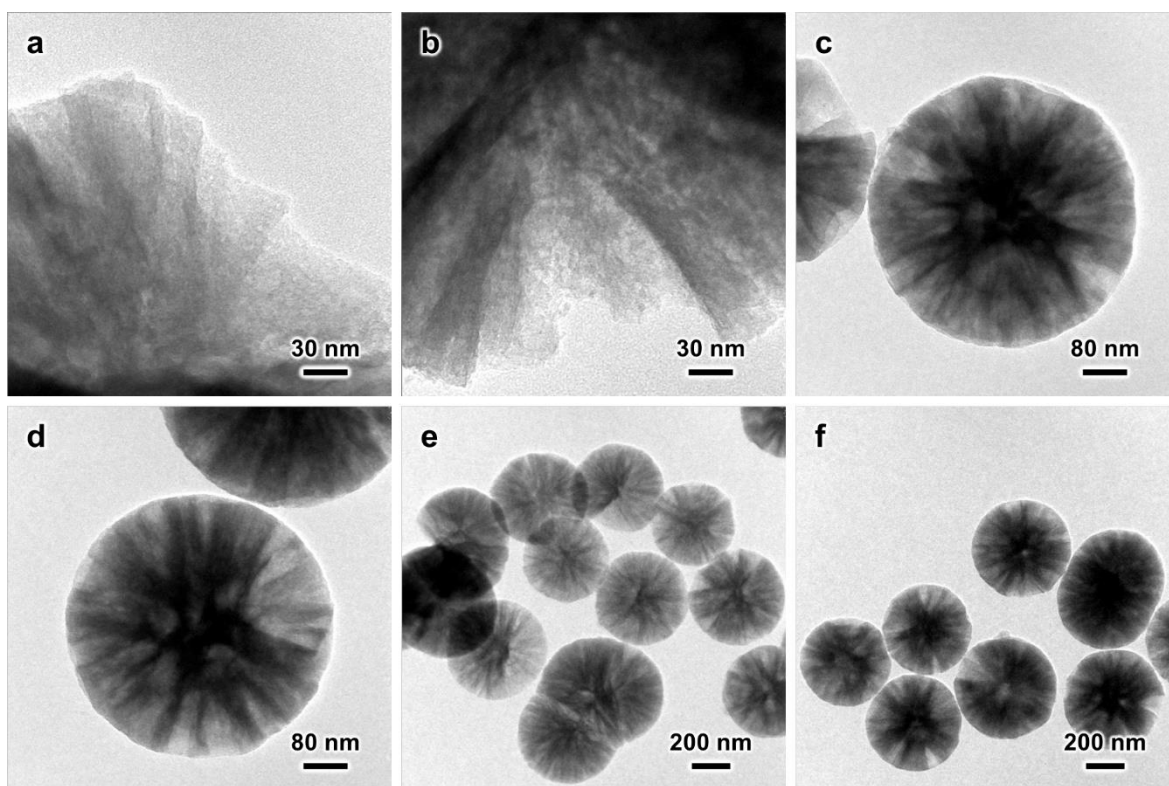


Figure S12. (a-f) TEM images of the synthesized MSS-SiRNH₂-Cu prepared according to Table S1, entry 4.

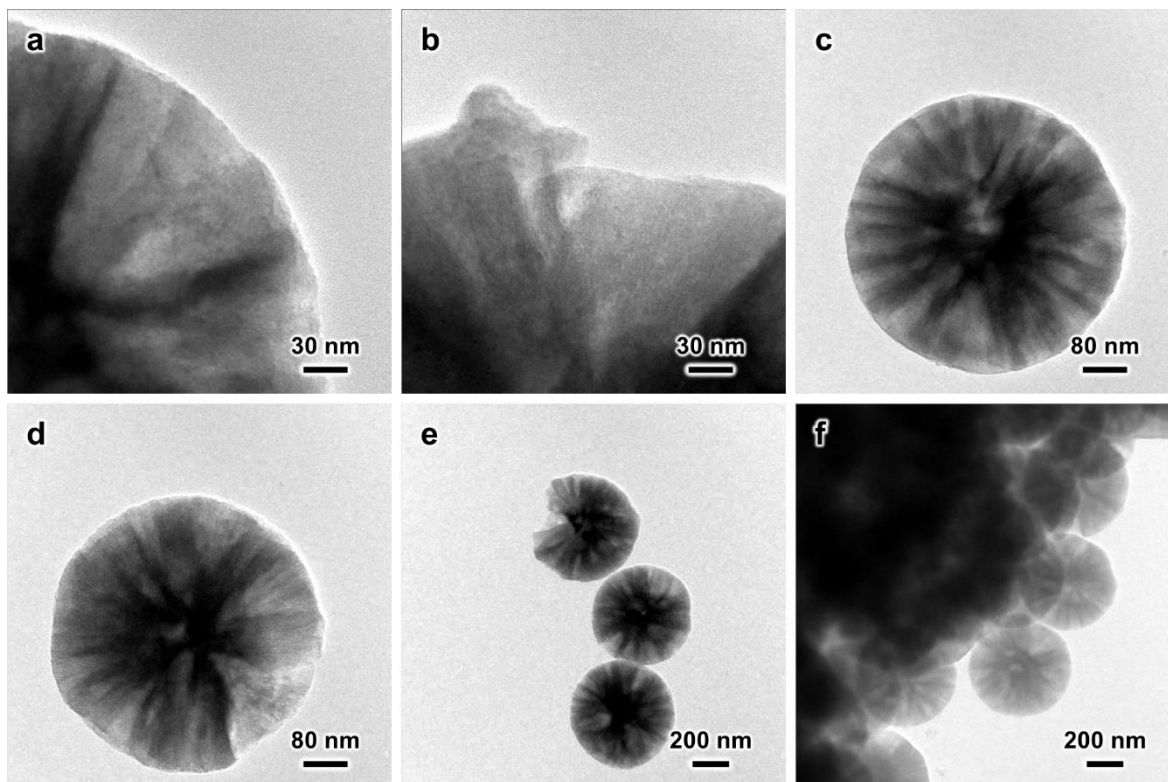


Figure S13. (a–f) TEM images of the synthesized MSS-SiRNH₂-Cu prepared according to Table S1, entry 5.

Comment: Figures S9–S13 showcase MSS-SiRNH₂-Cu samples prepared with various amounts of Cu(NO₃)₂·3H₂O but a fixed amount of APTMS precursors (Section 2.3, Table S1).

It is clear from the TEM images that the surface texture becomes rougher as the Cu content increases. In Figure S9, nearly no thread of SiRNH₂-Cu nanowires could be identified, and the surface texture appears similar to the pristine MSS. When the Cu content gets higher, more nanowire threads are observed yet the dimension does not increase.

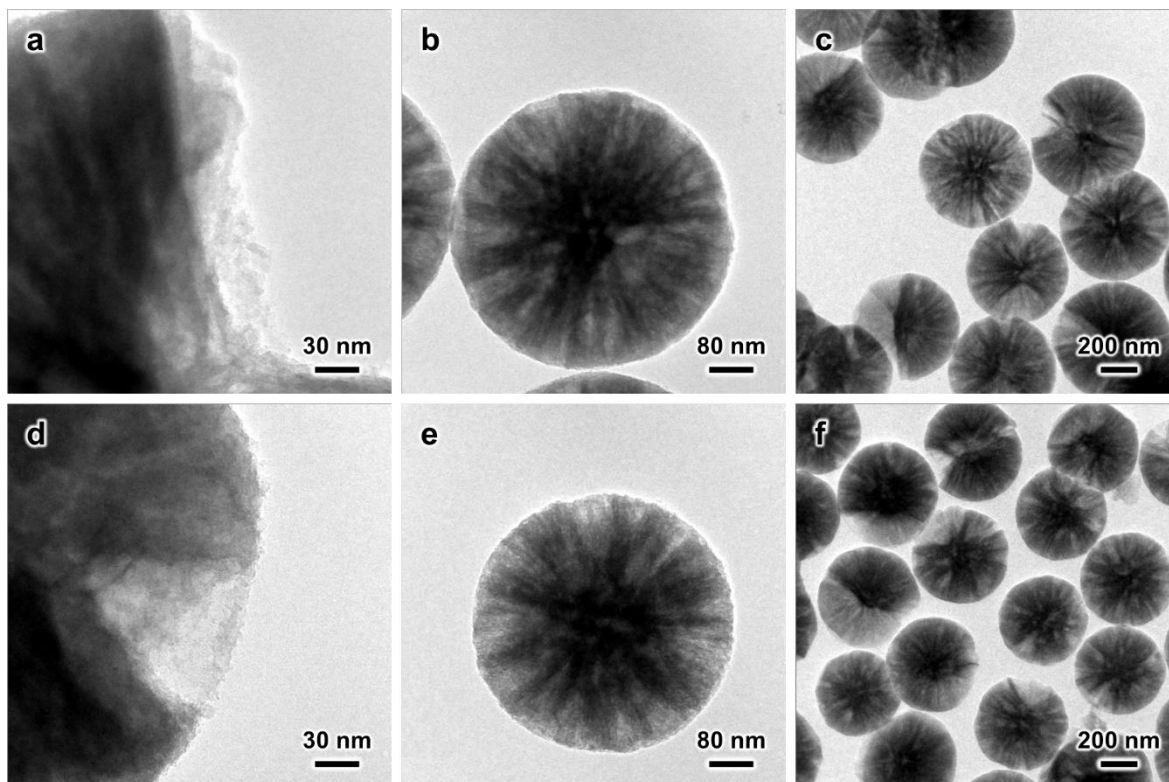


Figure S14. TEM images of the synthesized (a-c) MSS-SiRNH₂-Cu-Zn and (d-f) MSS-Si-Cu-Zn (after calcination) prepared according to Table S1, entry 6.

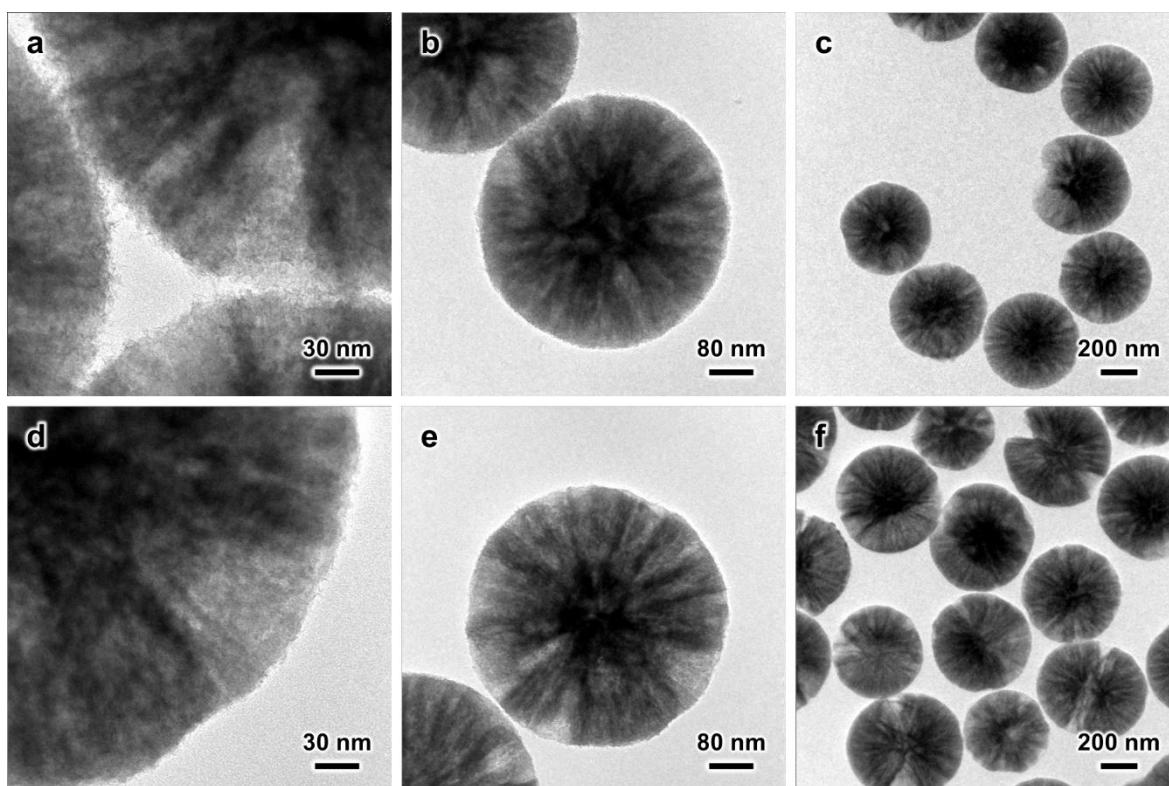


Figure S15. TEM images of the synthesized (a-c) MSS-SiRNH₂-Cu-Zn and (d-f) MSS-Si-Cu-Zn (after calcination) prepared according to Table S1, entry 7.

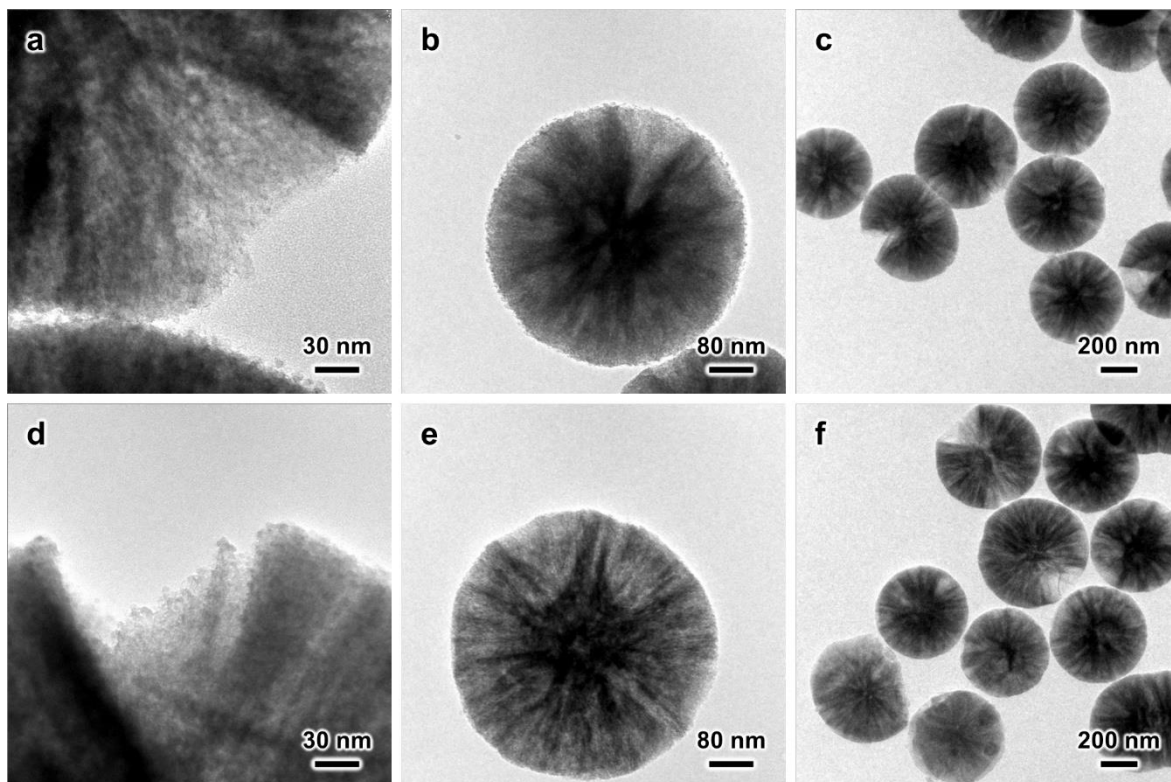


Figure S16. TEM images of the synthesized (a-c) MSS-SiRNH₂-Cu-Zn and (d-f) MSS-Si-Cu-Zn (after calcination) prepared according to Table S1, entry 8.

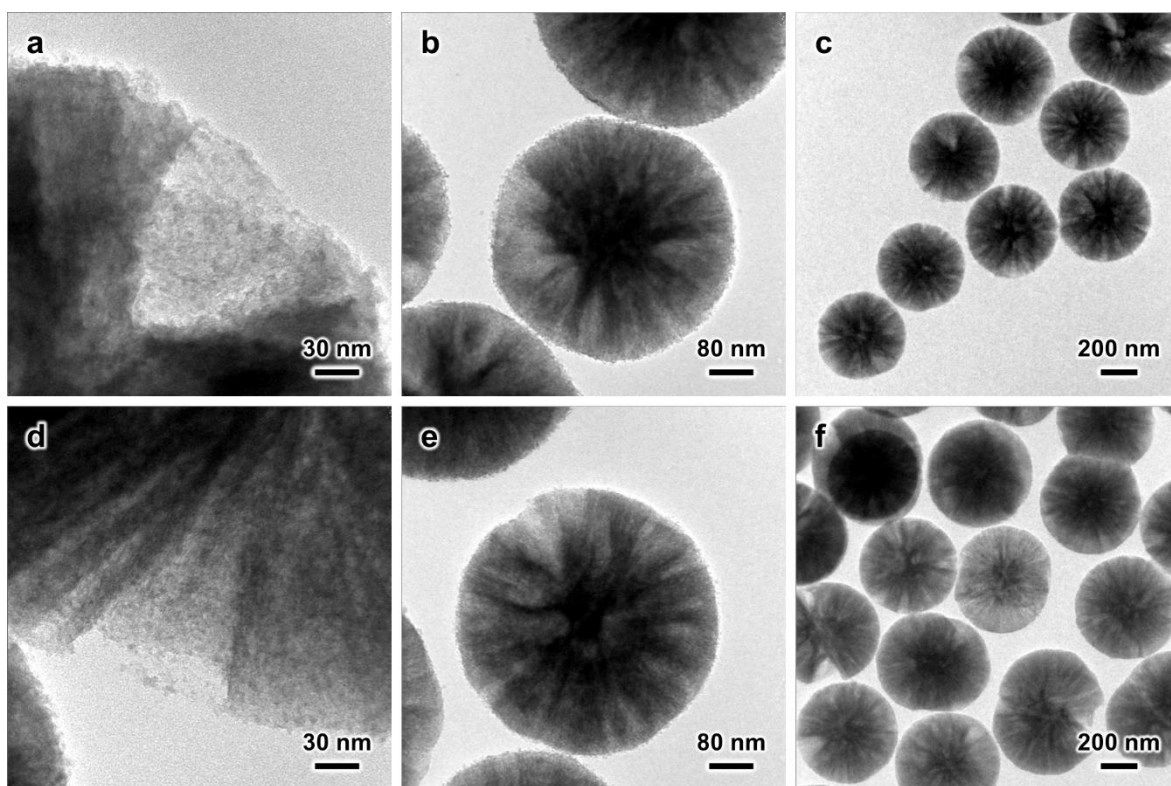


Figure S17. TEM images of the synthesized (a-c) MSS-SiRNH₂-Cu-Zn and (d-f) MSS-Si-Cu-Zn (after calcination) prepared according to Table S1, entry 9.

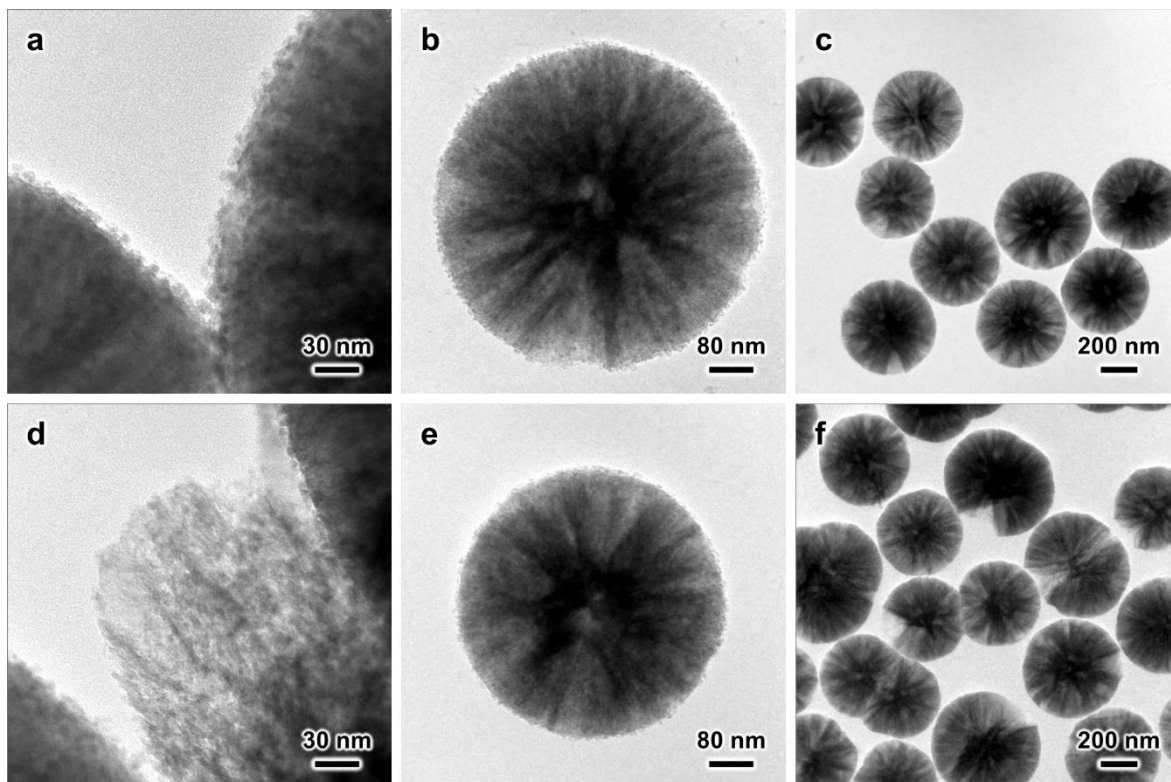


Figure S18. TEM images of the synthesized (a-c) MSS-SiRNH₂-Cu-Zn and (d-f) MSS-Si-Cu-Zn (after calcination) prepared according to Table S1, entry 10.

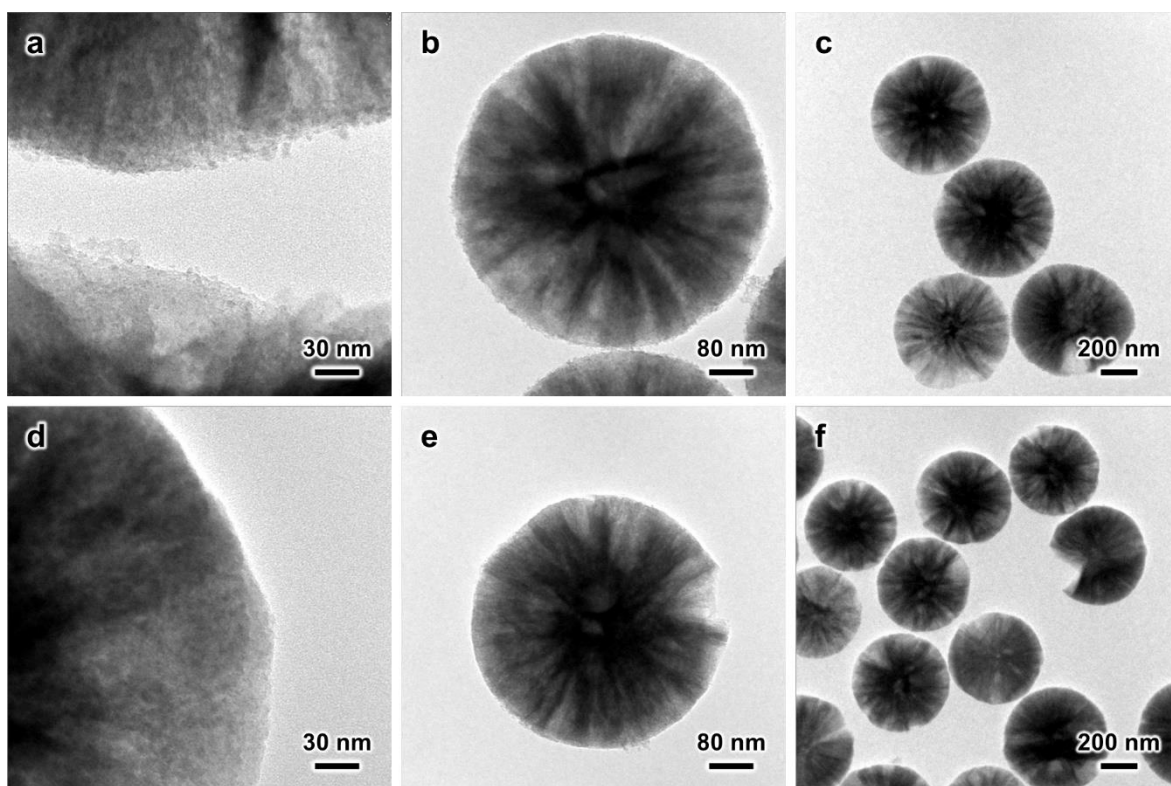


Figure S19. TEM images of the synthesized (a-c) MSS-SiRNH₂-Cu-Zn and (d-f) MSS-Si-Cu-Zn (after calcination) prepared according to Table S1, entry 11.

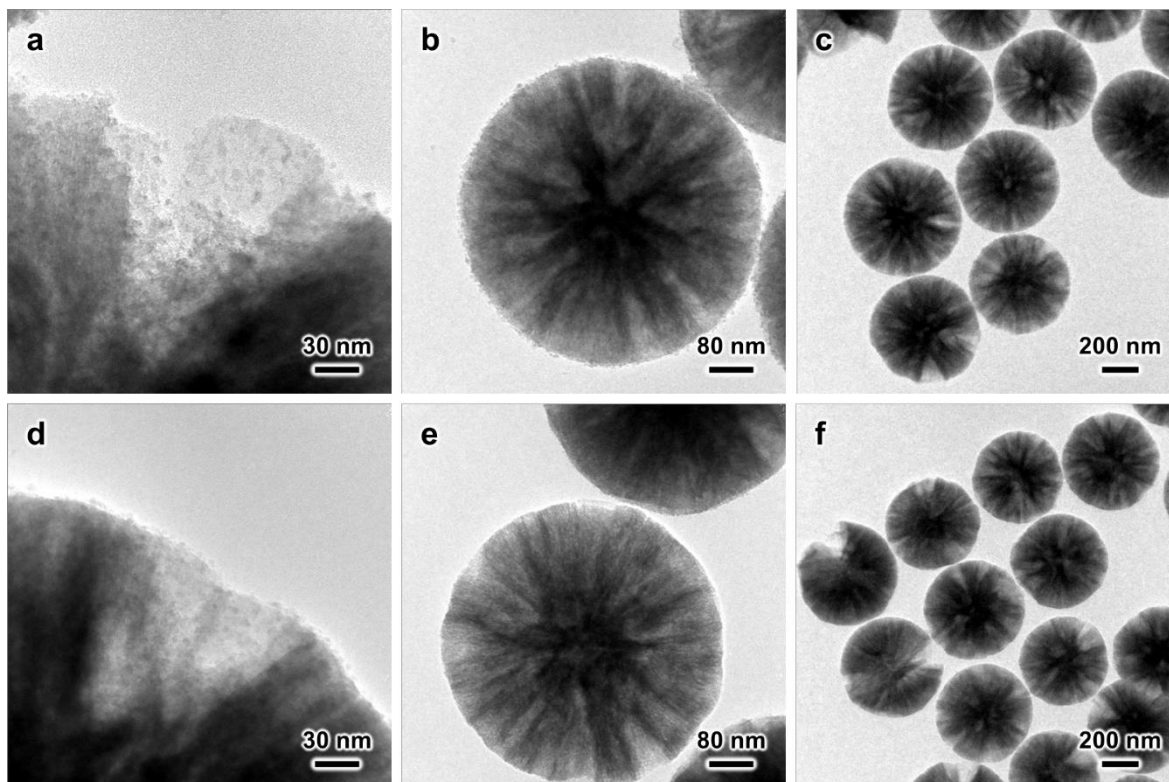


Figure S20. TEM images of the synthesized (a-c) MSS-SiRNH₂-Cu-Zn and (d-f) MSS-Si-Cu-Zn (after calcination) prepared according to Table S1, entry 12.

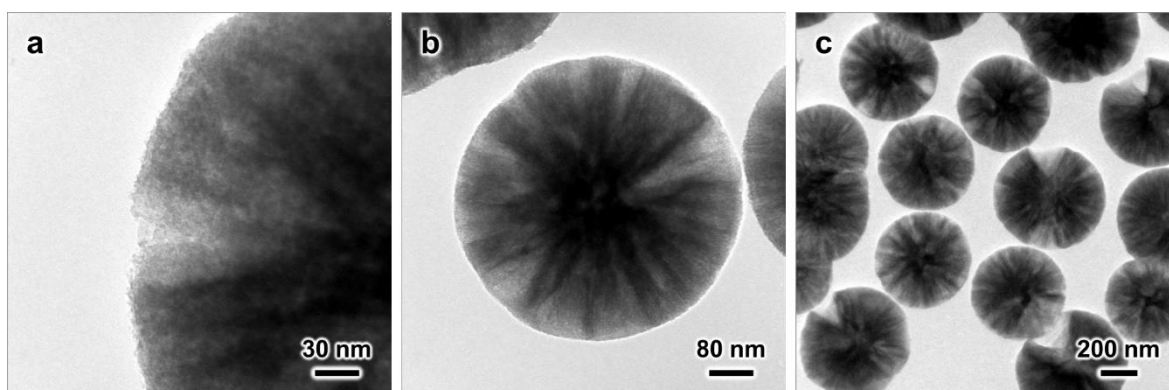


Figure S21. (a-c) TEM images of the synthesized MSS-Si-Cu-Zn (after calcination) prepared according to Table S1, entry 13.

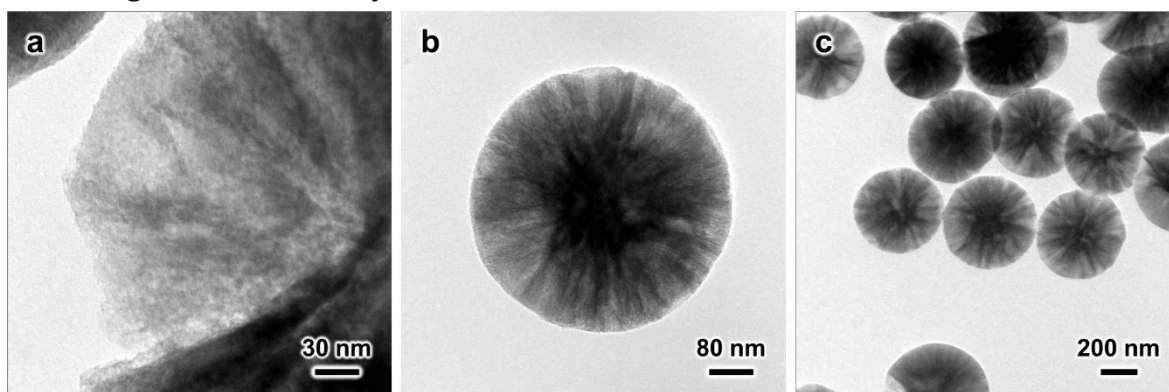


Figure S22. (a-c) TEM images of the synthesized MSS-Si-Cu-Zn (after calcination) prepared according to Table S1, entry 14.

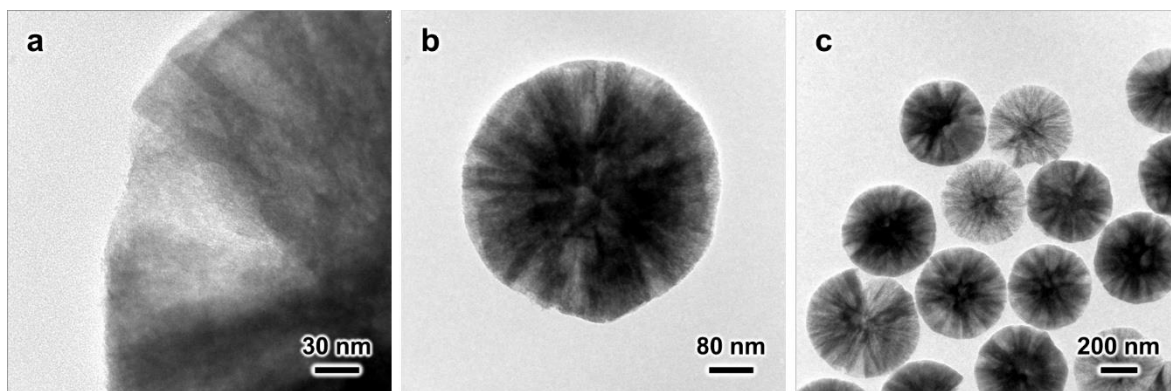


Figure S23. (a–c) TEM images of the synthesized MSS–Si–Cu–Zn (after calcination) prepared according to Table S1, entry 15.

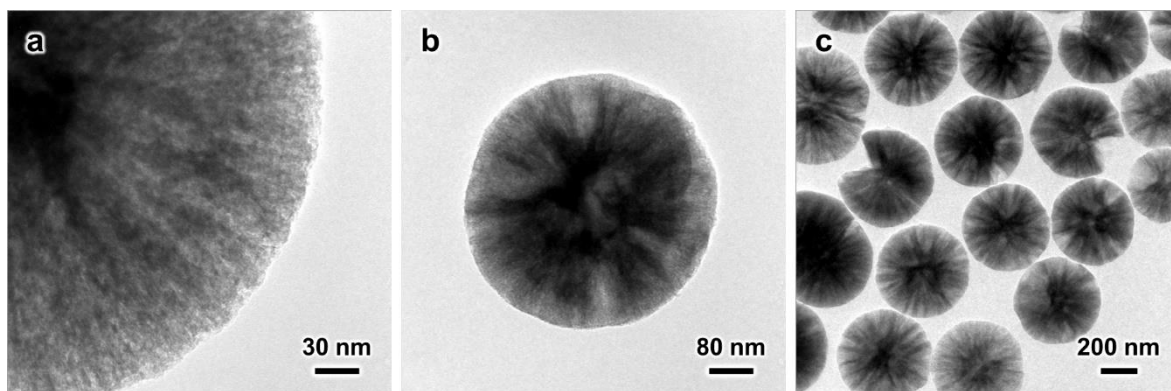


Figure S24. (a–c) TEM images of the synthesized MSS–Si–Cu–Zn (after calcination) prepared according to Table S1, entry 16.

Comments: The first rows of TEM images in Figures S14–S20 show different MSS–SiRNH₂–Cu–Zn samples prepared with various Cu and Zn loadings (different precursor amounts, Table S1). Upon the introduction of Zn(NO₃)₂ and heat treatment, the surface texture became rather coarse, with numerous nanoparticles. As proposed in the main text, these are ZnO nanoparticles resultant from decomposition of zinc hydroxides. Although the ZnO crystallites cannot be readily resolved with XRD technique (Figures S30, S37), it was discovered in our previous study that this method leads to formation of ZnO nanoparticles with identifiable XRD reflections.¹⁵ The reason the ZnO XRD peaks are missing is perhaps due to the low Zn content and the improved dispersion. This hypothesis is verified with FETEM investigation of the lattice fringes of these nanoparticles, revealing their identity to be ZnO (Figure 3e, f).

The second rows of TEM images in Figures S14–S20 and TEM images in Figures S21–S24 show different MSS–Si–Cu–Zn samples after the calcination treatment, which removed the alkylamine ligands. According to the TEM observation, the large ZnO nanoparticles observed in the uncalcined samples turned into smaller nanocrystallites with improved dispersion. According to our previous work, after the calcination treatment, a mixed oxide of ZnO and CuO was formed and the ZnO phase becomes better dispersed and less crystalline.^{16, 17} Despite that no ZnO or CuO XRD reflections could be observed (Figures S30, S37), FETEM observation disclosed ZnO crystallites and metallic Cu reduced from highly disperse CuO by electron beam (Figure 4e, f).

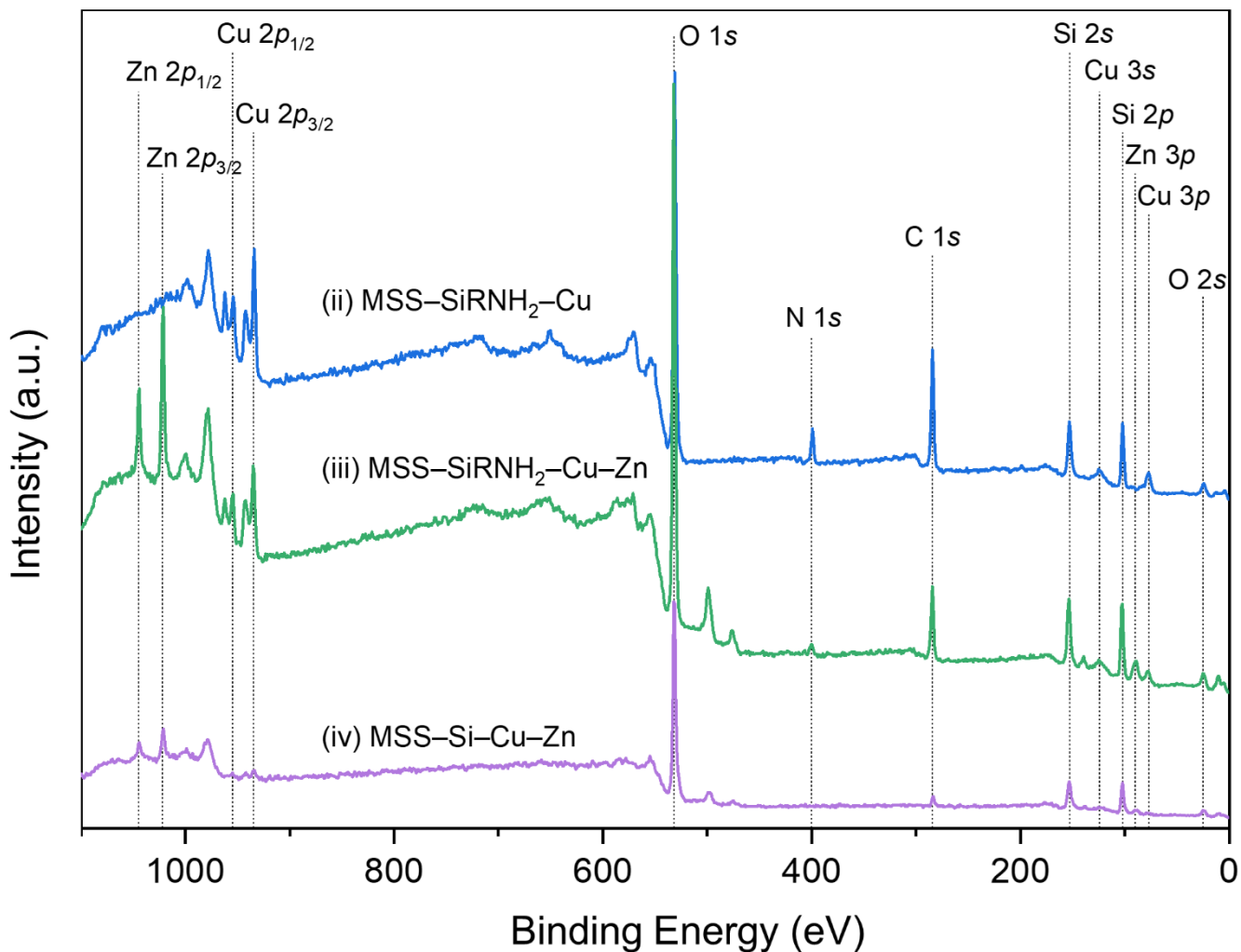


Figure S25. XPS survey scans of MSS-SiRNH₂-Cu, MSS-SiRNH₂-Cu-Zn, and MSS-Si-Cu-Zn samples.

Comment: The incorporation of SiRNH₂-Cu phase is reflected by the N 1s and Cu 2p signals, corresponding to nitrogen in the alkylamine ligands and the coordinated Cu²⁺ ions (MSS-SiRNH₂-Cu, blue line).

The introduction of Zn species is reflected by the emerging Zn 2p signals, accompanied by the weakened N 1s signal. The O 1s signal was greatly enhanced due to the numerous ZnO nanoparticles on the surface (MSS-SiRNH₂-Cu-Zn, green line).

After the calcination treatment, the alkylamine groups are completely removed (at least within the detection limit of XPS technique, *ca.* 10 nm beneath the surface), reflected by the complete diminishment of N 1s signal (MSS-Si-Cu-Zn, purple line).

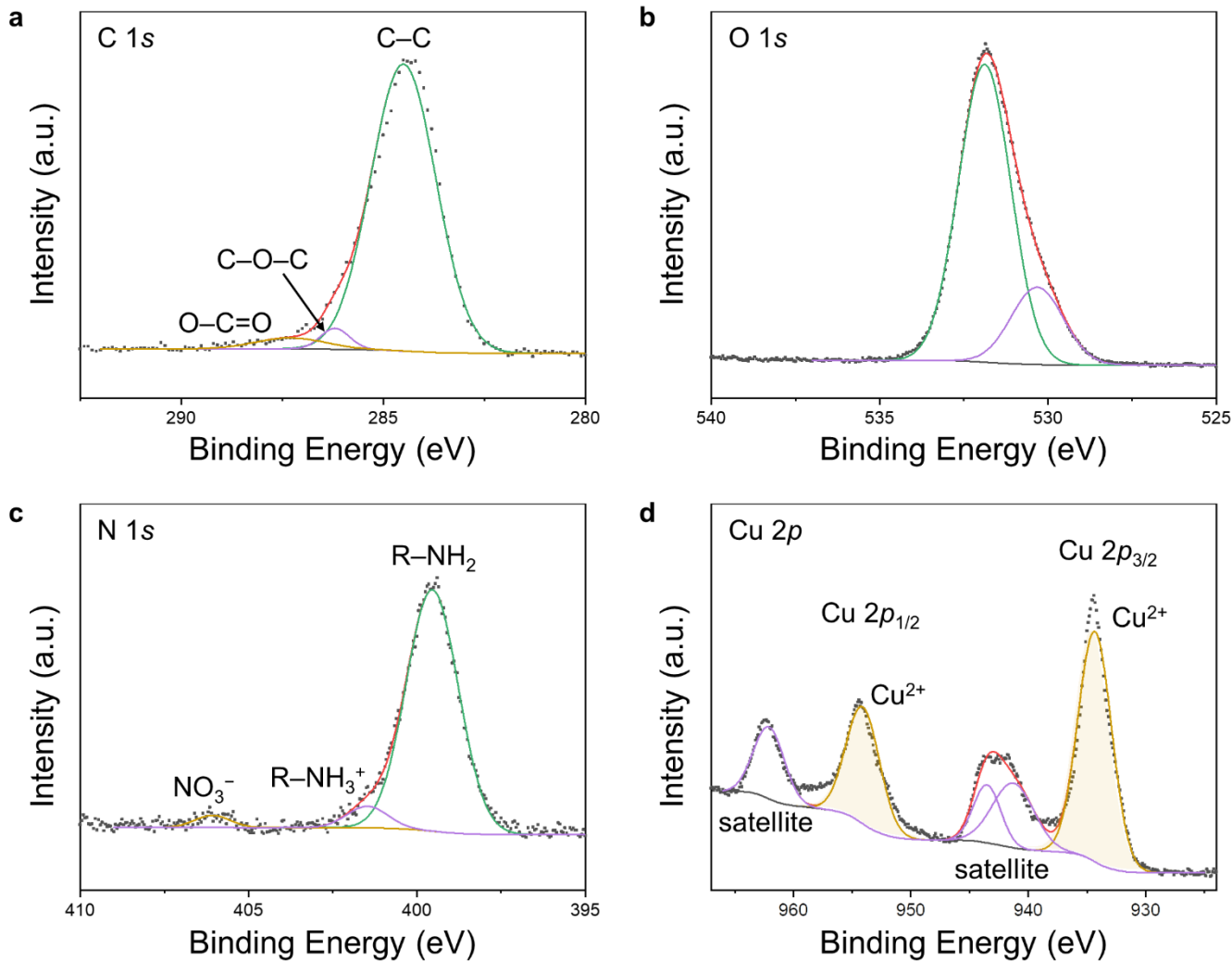


Figure S26. XPS profiles of the MSS-SiRNH₂-Cu sample in (a) C 1s, (b) O 1s, (c) N 1s, and (d) Cu 2p regions, respectively.

Comment: The C 1s region of MSS-SiRNH₂-Cu sample (Figure S26a) is characteristic of adventitious carbon contamination, with binding energies of 284.5, 286.2, and 287.3 eV corresponding to C-C, C-O-C, and O-C=O species, respectively.

The O 1s region of MSS-SiRNH₂-Cu sample (Figure S26b) is composed of SiO₂ (531.9 eV) and silanol groups (Si-OH, 530.3 eV). The 530.3 eV peak could be as well attributed to surface oxidized CuO or CuCO₃ due to adventitious carbon contamination.

The N 1s region of MSS-SiRNH₂-Cu sample (Figure S26c) consists of R-NH₂ (399.5 eV), protonated R-NH₃⁺ (401.5 eV), and remainder NO₃⁻ (406.1 eV) from the Cu(NO₃)₂ precursor.

The Cu 2p region of MSS-SiRNH₂-Cu sample (Figure S26d) is characteristic of Cu²⁺, with Cu 2p_{3/2} peak located at 934.3 eV, with characteristic satellite features.

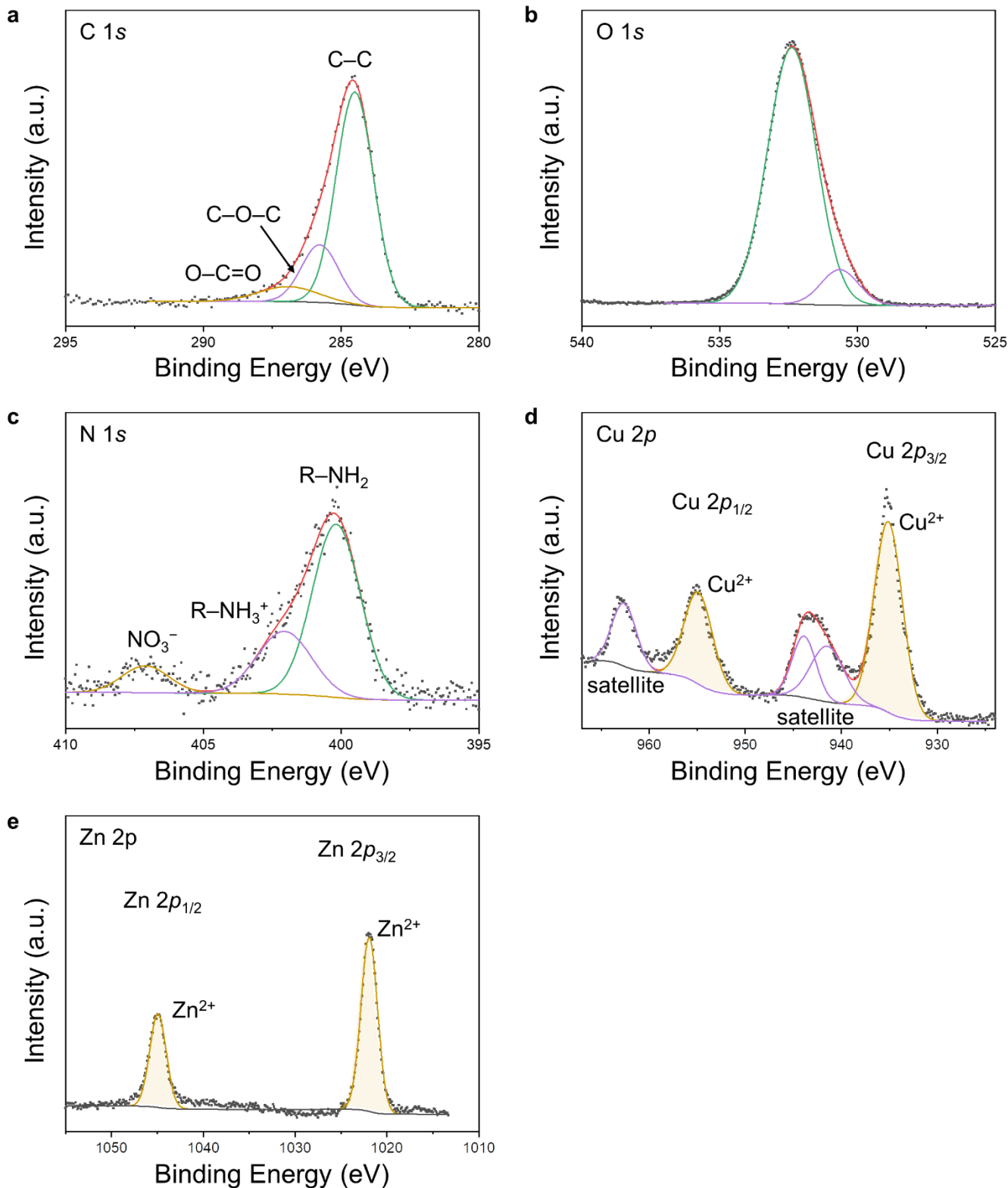


Figure S27. XPS profiles of the MSS-SiRNH₂-Cu-Zn sample in (a) C 1s, (b) O 1s, (c) N 1s, (d) Cu 2p, and (e) Zn 2p regions, respectively.

Comment: The C 1s region of MSS-SiRNH₂-Cu-Zn sample (Figure S27a) is typical of adventitious carbon contamination, with binding energies of 284.5, 285.8, and 286.9 eV corresponding to C-C, C-O-C, and O-C=O species, respectively.

The O 1s region of MSS-SiRNH₂-Cu-Zn sample (Figure S27b) is composed of SiO₂ (532.4 eV) and ZnO species (Si-OH, 530.6 eV).

The N 1s region of MSS-SiRNH₂-Cu-Zn sample (Figure S27c) consists of R-NH₂ (400.2 eV), protonated R-NH₃⁺ (402.1 eV), and remainder NO₃⁻ (407.1 eV) from the Zn(NO₃)₂ precursor.

The Cu 2p region of MSS-SiRNH₂-Cu-Zn sample (Figure S27d) is characteristic of Cu²⁺, with Cu 2p_{3/2} peak located at 935.1 eV, with characteristic satellite features.

The Zn 2p region of MSS-SiRNH₂-Cu-Zn sample (Figure S27e) shows a unimodal doublet with Zn 2p_{3/2} located at 1021.9 eV and is representative for ZnO.

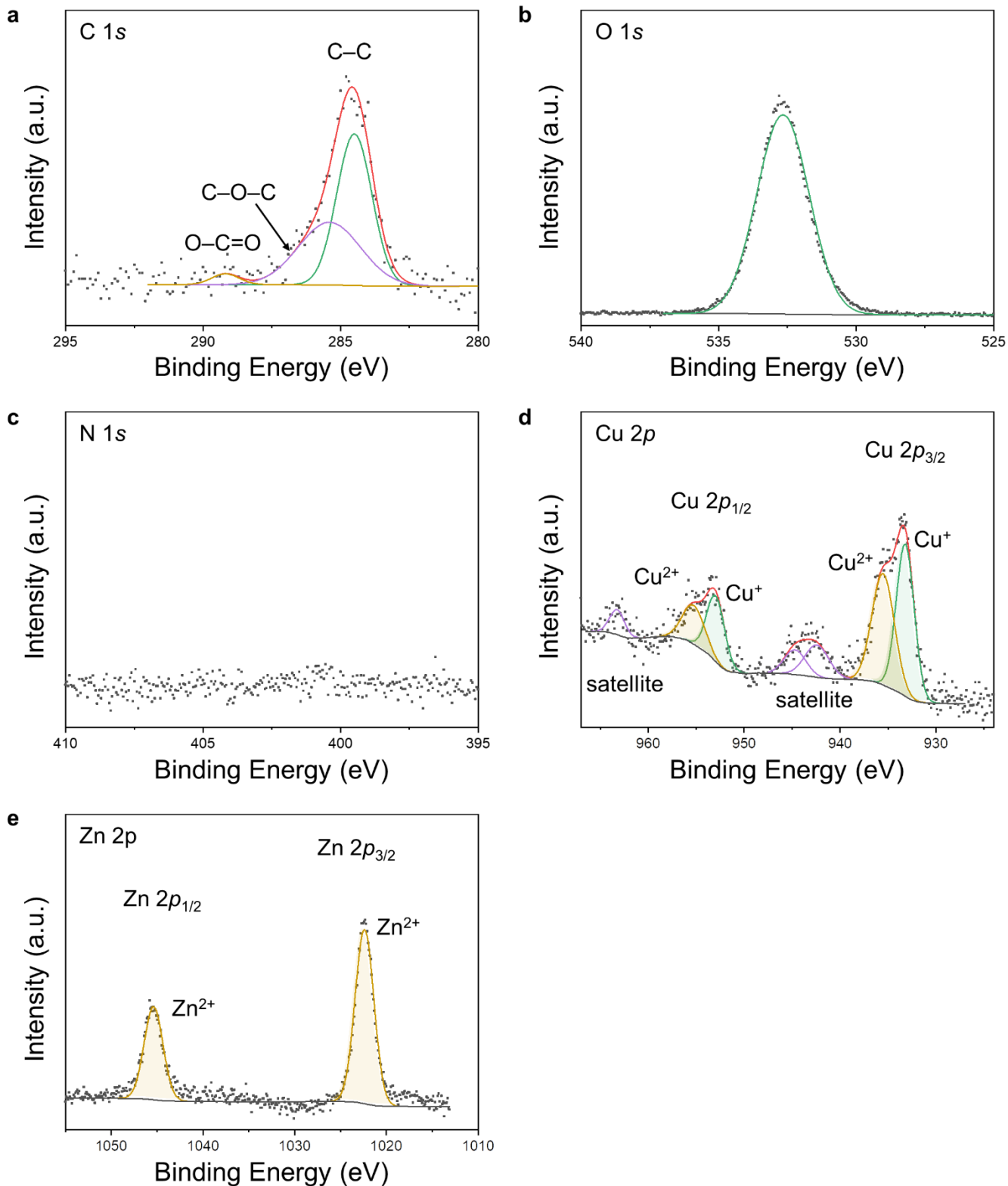


Figure S28. XPS profiles of the MSS-Si-Cu-Zn sample in (a) C 1s, (b) O 1s, (c) N 1s, (d) Cu 2p, and (e) Zn 2p regions, respectively.

Comment: The C 1s region of MSS-Si-Cu-Zn sample (Figure S28a) is typical of adventitious carbon contamination, with binding energies of 284.5, 285.4, and 289.2 eV corresponding to C-C, C-O-C, and O-C=O species, respectively.

The O 1s region of MSS–Si–Cu–Zn sample (Figure S28b) is composed of a single peak representing SiO₂ (532.7 eV). The absence of metal oxide components is attributed to the good dispersion of highly amorphous CuO and ZnO phase, as well as the condensed SiO₂ phase after calcination.

The N 1s signal of MSS–Si–Cu–Zn sample (Figure S28c) fully diminished, due to the complete removal of alkylamine ligands during the calcination treatment.

The Cu 2p region of MSS–Si–Cu–Zn sample (Figure S28d) shows a component typical of Cu²⁺, with Cu 2p_{3/2} component located at 935.5 eV, with characteristic satellite features. However, another Cu 2p_{3/2} component located at 933.2 eV is attributed to Cu⁺ species.

The Zn 2p region of MSS–Si–Cu–Zn sample (Figure S28e) shows a unimodal doublet with Zn 2p_{3/2} located at 1022.4 eV and is representative for ZnO.

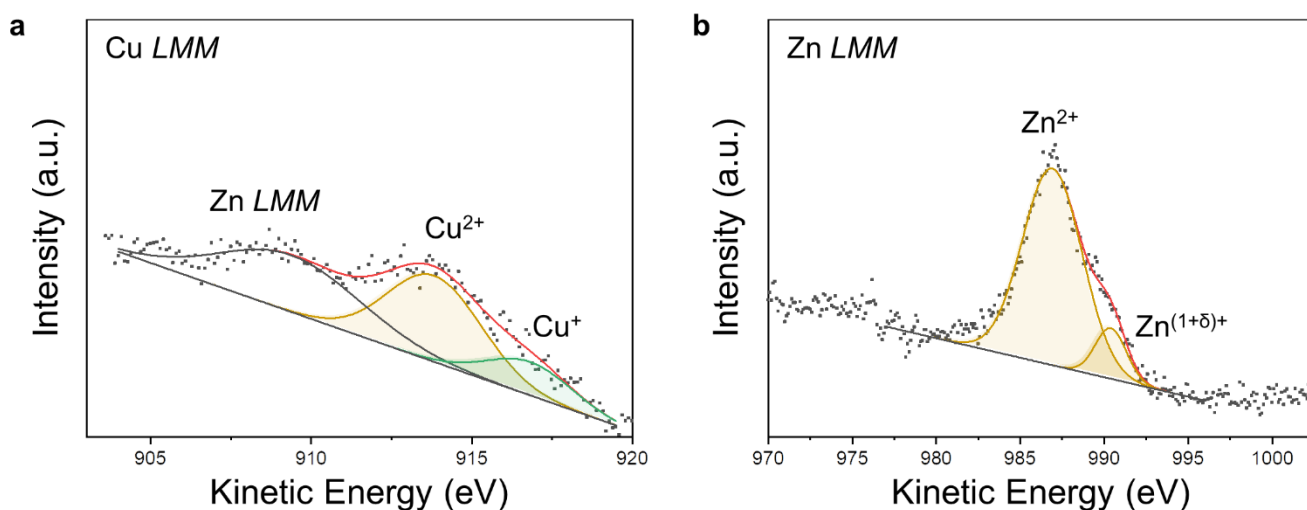


Figure S29. XAES profiles of the MSS–Si–Cu–Zn sample in (a) Cu LMM and (b) Zn LMM regions.

Comment: The valence states of Cu and Zn species in MSS–Si–Cu–Zn are further confirmed with XAES technique. The Cu LMM region were deconvoluted into two peaks and they are accordingly assigned to Cu²⁺ species (913.8 eV) and Cu¹⁺ (916.8 eV), respectively. The Zn LMM region were deconvoluted into a main peak centered at 986.9 eV typical for Zn²⁺, with a shoulder feature located at 990.4 eV attributed to Zn^{(1+δ)+}.

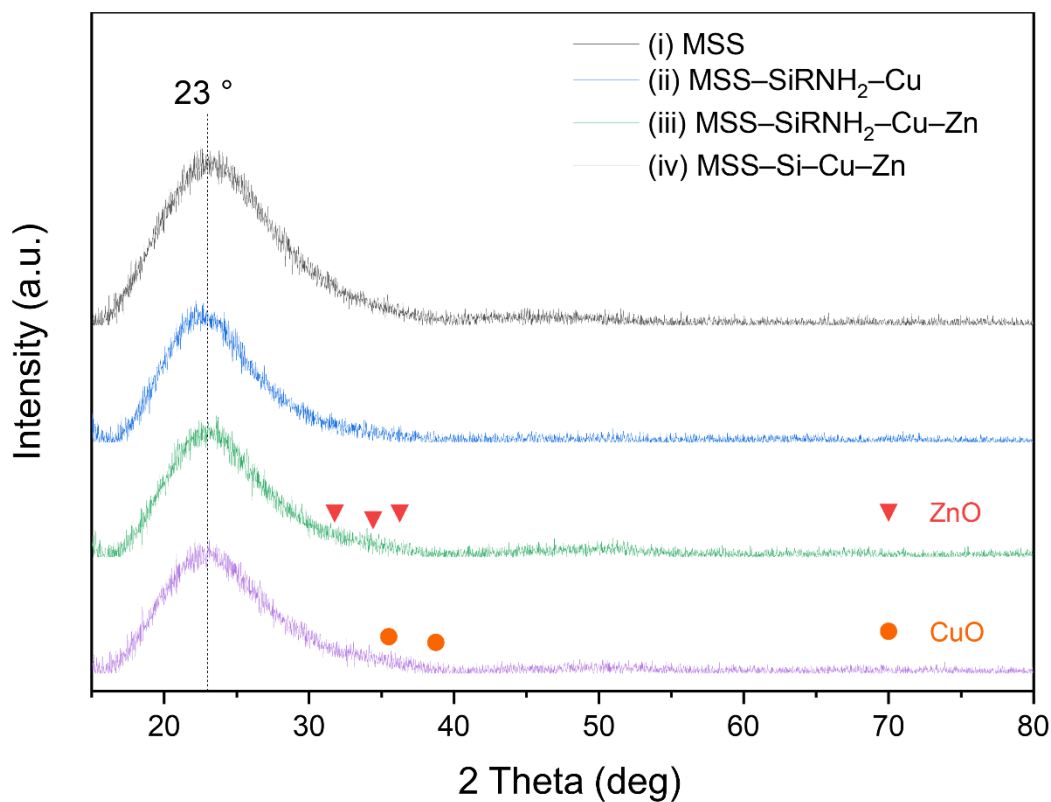


Figure S30. XRD profiles of MSS, MSS-SiRNH₂-Cu, MSS-SiRNH₂-Cu-Zn, and MSS-Si-Cu-Zn samples.

Comment: As discussed at the end of Section 3.2, Figure S30 depicts the XRD profiles of the catalyst samples at various synthetic stages. However, all the profiles only show a broad reflection around $2\theta = 23^\circ$, which is characteristic of amorphous silica materials. Reflections due to ZnO and CuO species found in our previous study with the similar synthetic procedure could not be identified, presumably because of the high dispersion of these phases.

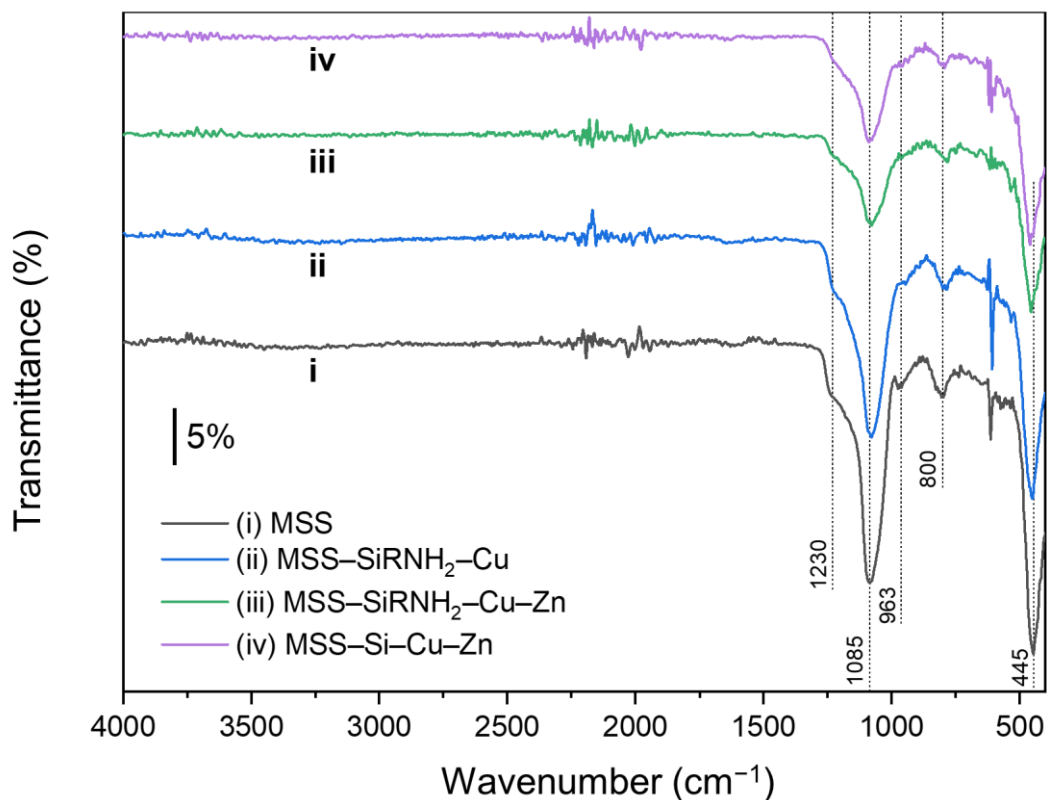


Figure S31. FTIR spectra of MSS, MSS-SiRNH₂-Cu, MSS-SiRNH₂-Cu-Zn, and MSS-Si-Cu-Zn samples.

Comment: As discussed toward the end of Section 3.2, Figure S31 shows the FTIR spectra of the catalyst sample at different synthetic stages. The strong absorption at 1085 cm^{-1} with a shoulder feature at 1230 cm^{-1} is attributed to the asymmetric and symmetric stretching of Si-O-Si in SiO₄ tetrahedra. Absorptions at 963 and 445 cm^{-1} are ascribed to Si-OH stretching and Si-O-Si bending vibrations, respectively. Similar to our XRD characterization, the strong FTIR features of the MSS support largely cover up the characteristic absorptions of the coated shell. Hence, chemical bonding information including C-H and N-H bonds found in our previous work could not be easily resolved here.

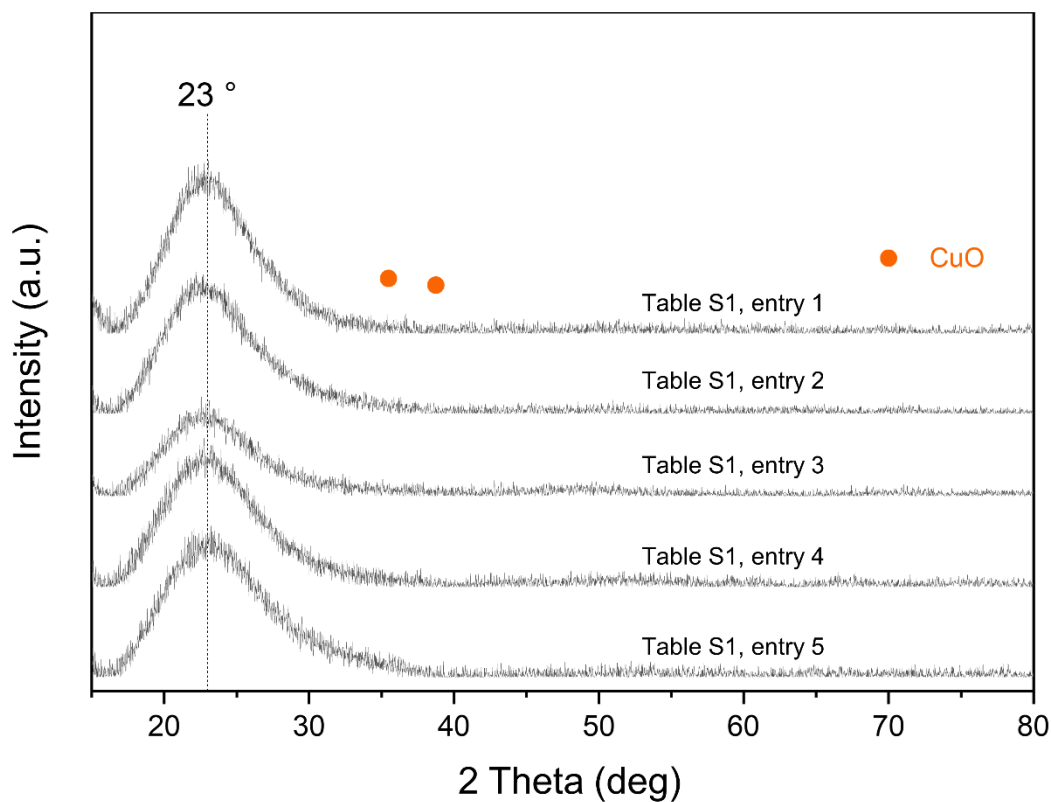


Figure S32. XRD profiles of MSS-SiRNH₂-Cu samples prepared with different amounts of Cu precursor (Table S1, entries 1–5).

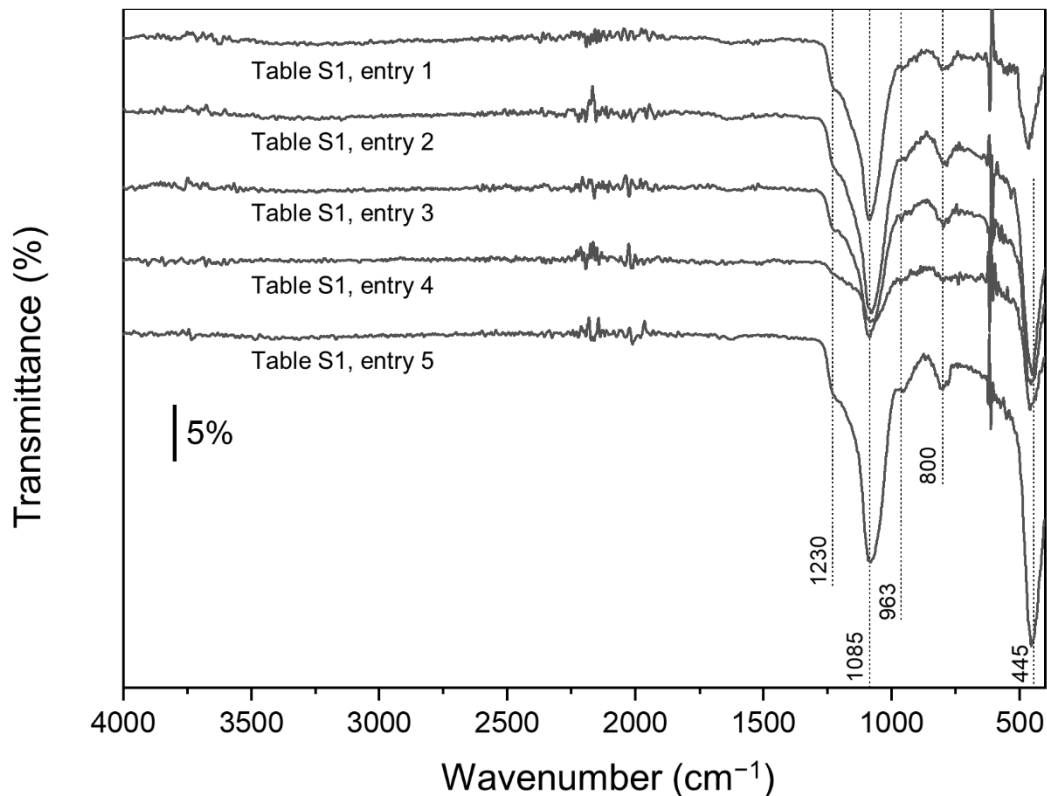


Figure S33. FTIR spectra of MSS-SiRNH₂-Cu samples prepared with different amounts of Cu precursor (Table S1, entries 1–5).

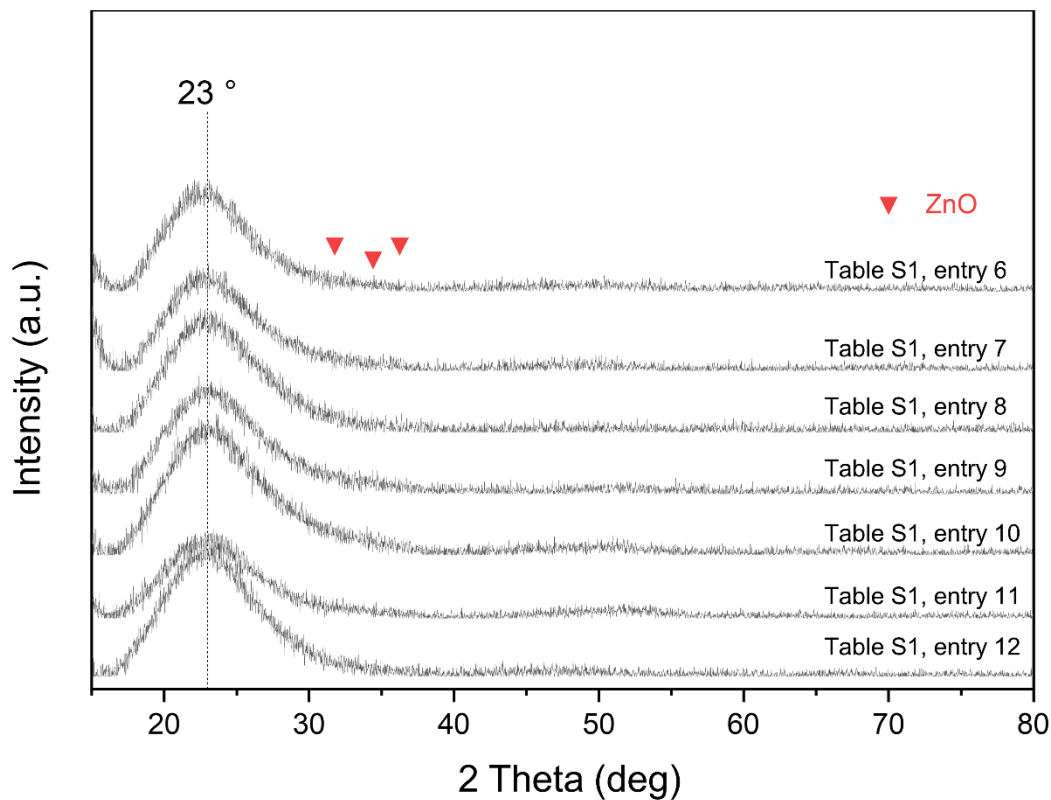


Figure S34. XRD profiles of MSS-SiRNH₂-Cu-Zn samples prepared with different amounts of Cu and Zn precursors (Table S1, entries 6–12).

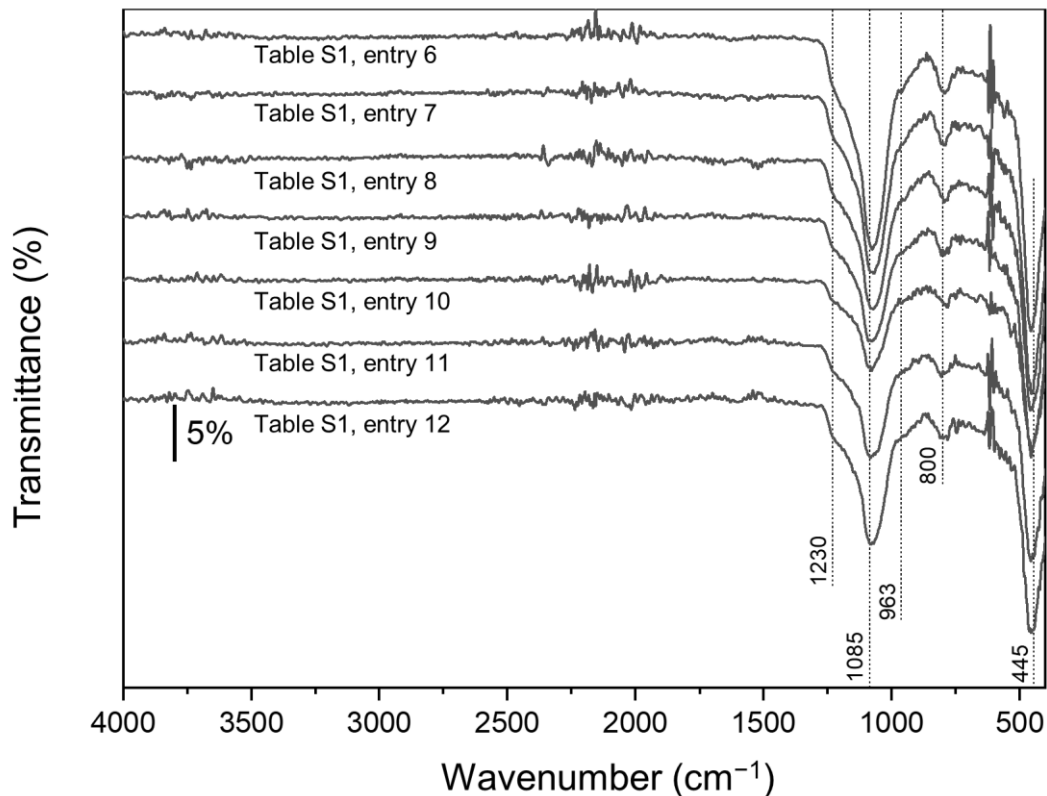


Figure S35. FTIR spectra of MSS-SiRNH₂-Cu-Zn samples prepared with different amounts of Cu and Zn precursors (Table S1, entries 6–12).

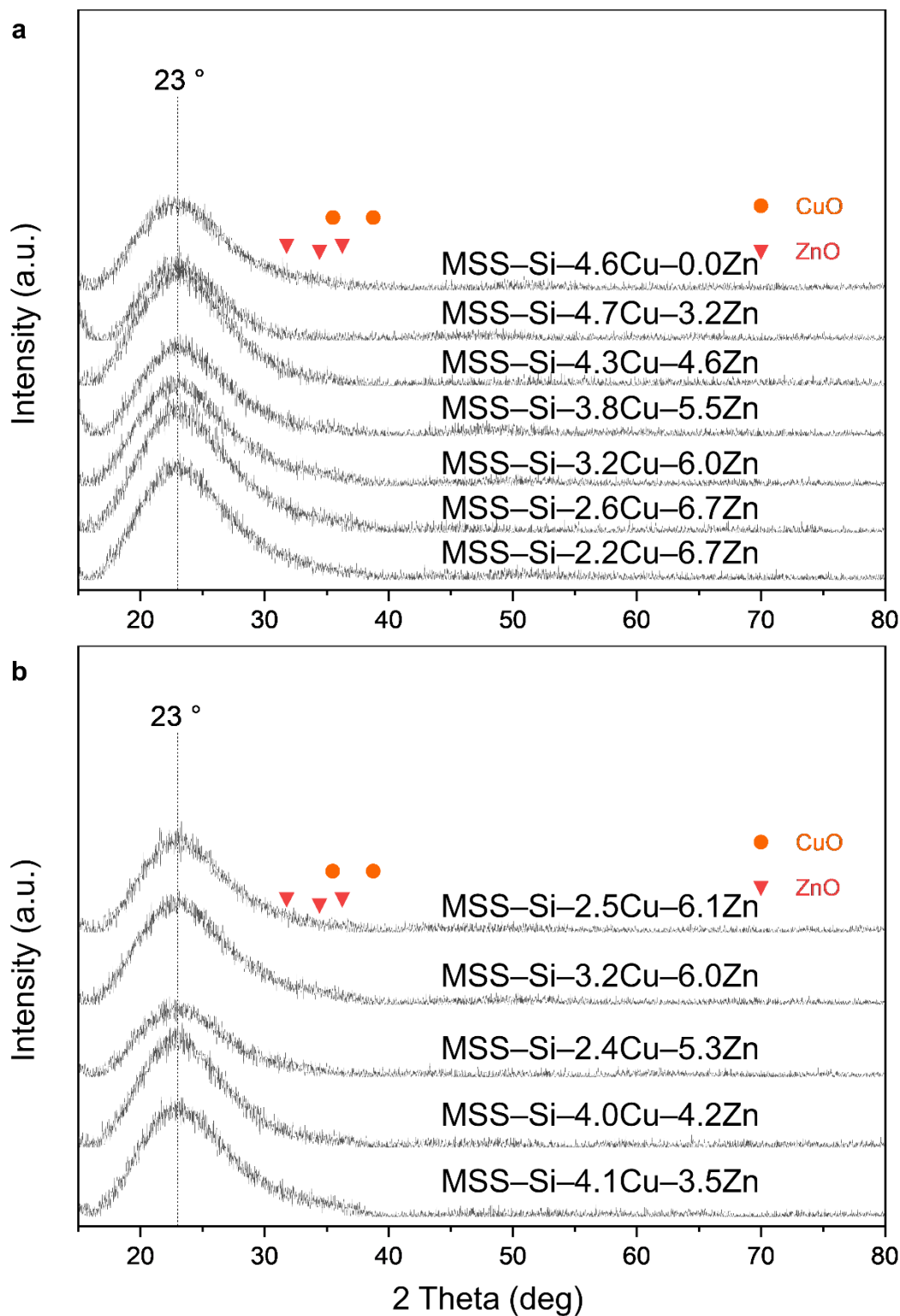


Figure S36. (a, b) XRD profiles of MSS-Si-Cu-Zn samples prepared with different amounts of Cu and Zn precursors (Table S1, entries 6–16).

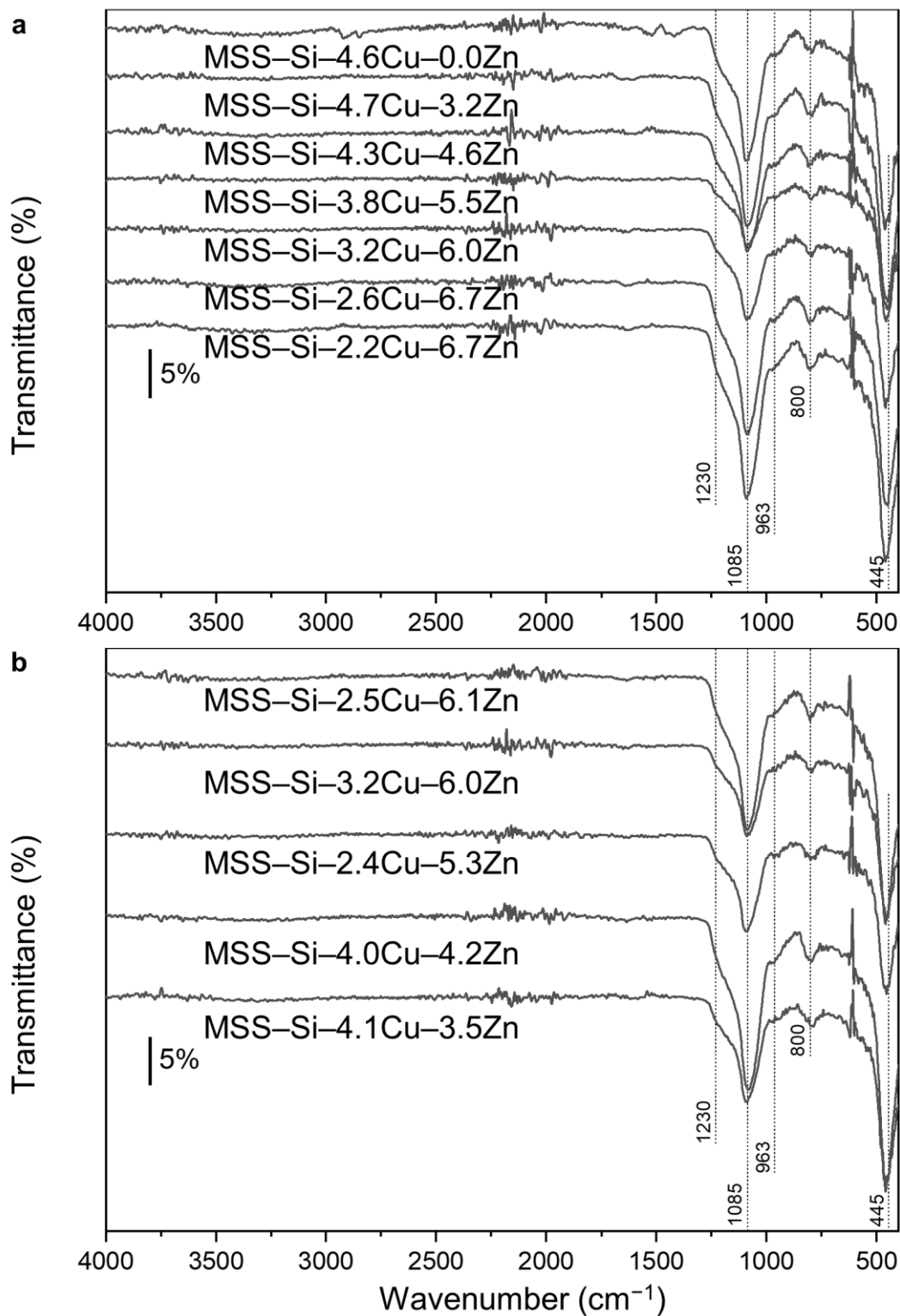


Figure S37. (a, b) FTIR spectra of MSS-Si-Cu-Zn samples prepared with different amounts of Cu and Zn precursors (Table S1, entries 6–16).

Comment: For various MSS-SiRNH₂-Cu-Zn and MSS-Si-Cu-Zn samples, we have similar observations as in Figures S30 and S31, where the strong signals due to the MSS support fully covers up the signals of the dispersed active phase in both XRD and FTIR spectra.

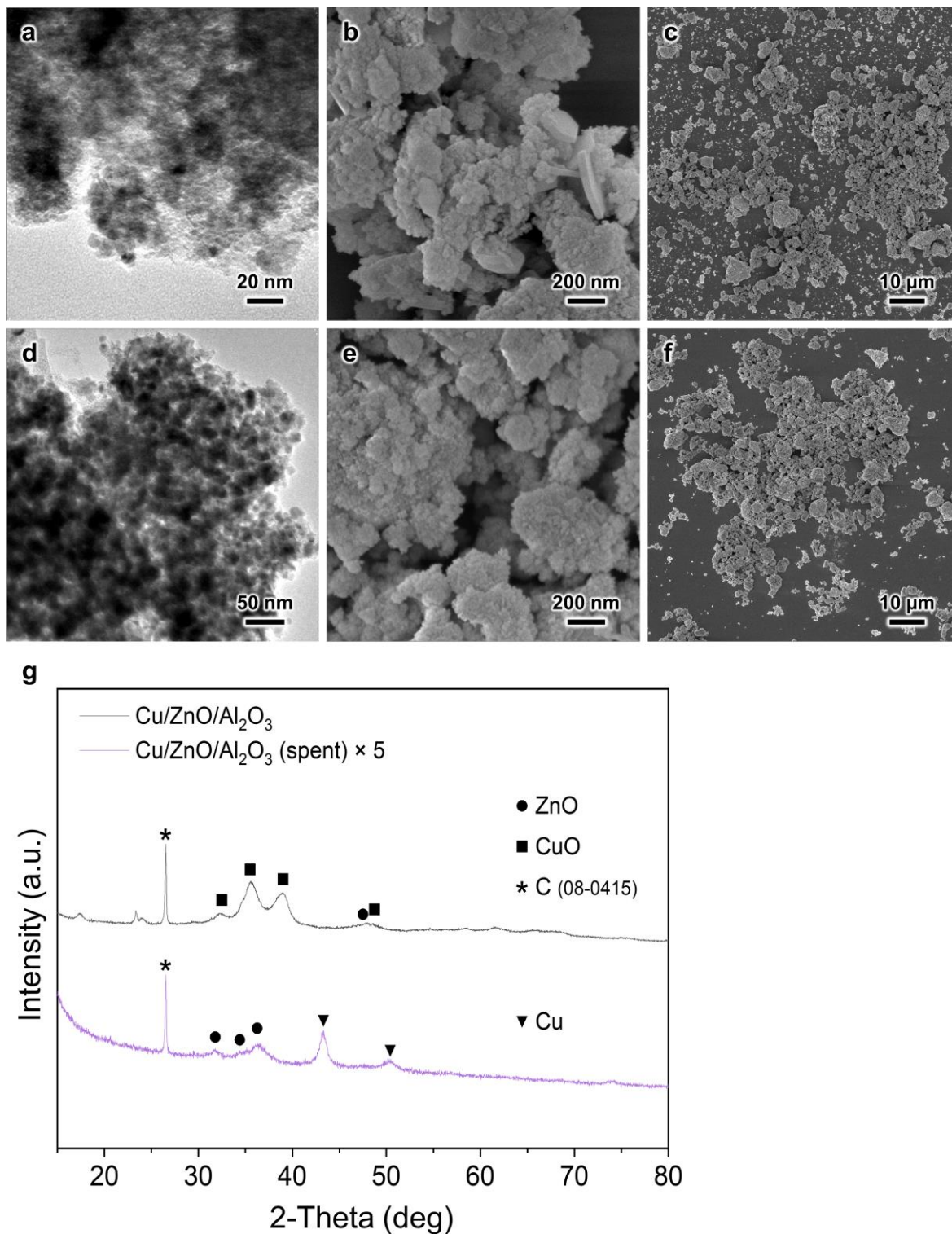


Figure S38. (a–f) TEM and FESEM images of commercial Cu/ZnO/Al₂O₃ catalyst (a–c) before and (d–f) after CO₂ hydrogenation reaction. (g) XRD patterns of commercial Cu/ZnO/Al₂O₃ catalyst before and after CO₂ hydrogenation reaction.

Comment: The commercial Cu/ZnO/Al₂O₃ catalyst for methanol synthesis was purchased from Alfa Aesar (Product number 45776) in the form of pellets. The pellets were ground to fine powder with a mortar before tested with the packed bed reactor. The composition provided by the manufacturer is 60–68 wt % CuO, 22–26 wt % ZnO, 8–12 wt % Al₂O₃, and 1–3 wt % MgO; and the composition was verified with ICP-OES measurement.

Figure S38a–f depicts the fresh and spent forms of the co-precipitation derived mixed oxide. Overall, the commercial catalyst appears as aggregates in both forms, with nano- to microscale fragments. Furthermore, the XRD patterns of the commercial catalyst before and after the reaction manifest characteristic reflections of CuO/Cu and ZnO (Figure S38g). The strong and sharp peaks suggest large crystallite dimensions of the commercial Cu/ZnO/Al₂O₃ catalyst. In fact, the crystallite size of the metallic Cu in the spent Cu/ZnO/Al₂O₃ catalyst (after reaction) was estimated by the Scherrer equation to be 9.5 nm.¹⁵

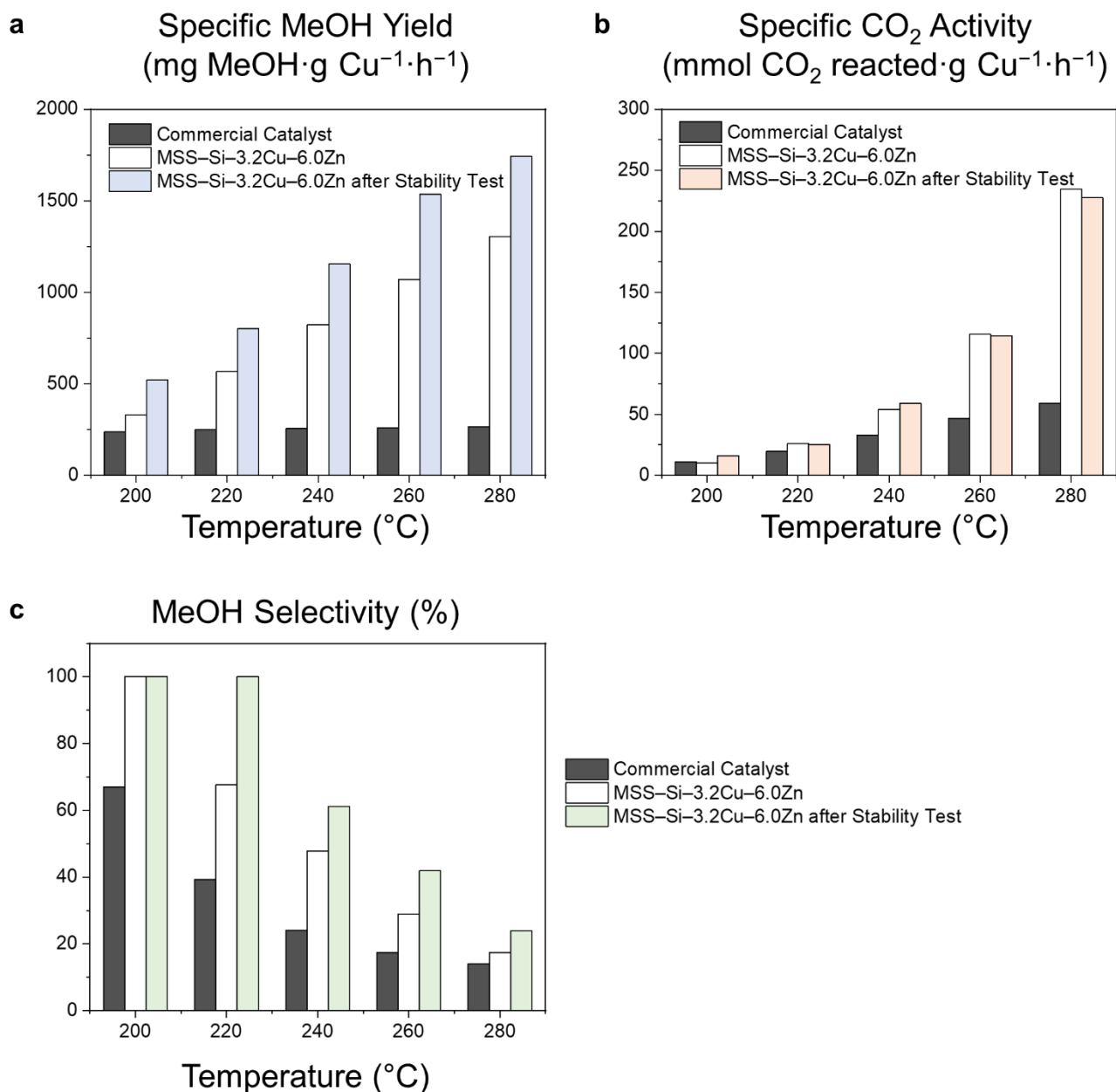


Figure S39. Catalytic performance of the spent MSS-Si-3.2Cu-6.0Zn catalyst after the 200-h stability test, in comparison with fresh catalyst. (a) Cu-specific MeOH yield. (b) MeOH selectivity. (c) Cu-specific CO₂ activity.

Comment: After the 200-h stability test, the reactor was depressurized, cooled down to ambient temperature, and purged with N₂ for 30 min (GC samples were taken to ensure no residual reactant or product). Then the catalyst activity was evaluated again according to procedures in Section 2.7, bypassing the reduction process.

The spent catalyst after 200-h stability test exhibited higher specific MeOH yield, better MeOH selectivity, but slightly reduced specific CO₂ activity (Figure S39). It is inferred that during the stability test, some positive structural reconfiguration occurred, leading to enhanced SMSI in the Cu-ZnO system (e.g., Zn migration to Cu defect sites forming alloy) and resulting in improved MeOH yield. Such structure reconfiguration simultaneously suppresses the RWGS reaction that produces CO, causing an overall slight drop of CO₂ activity.

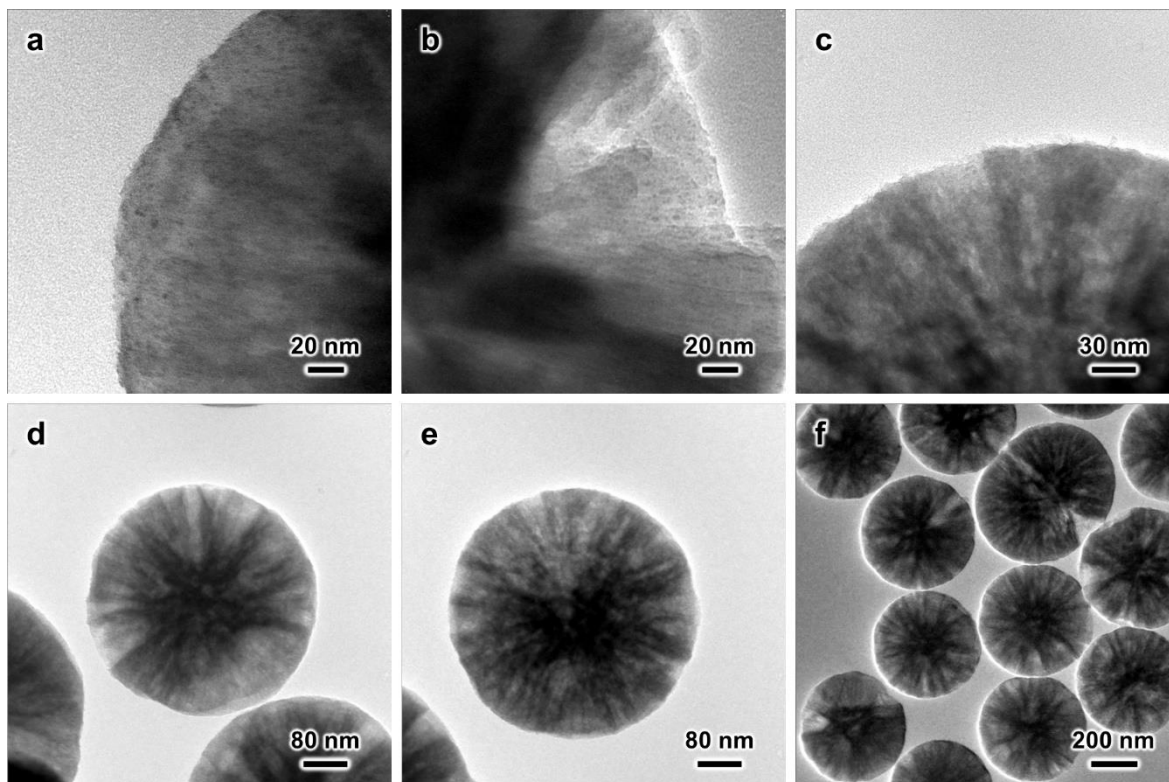


Figure S40. (a-f) TEM images of the spent MSS-Si-4.6Cu-0Zn catalyst (Table S1, entry 6).

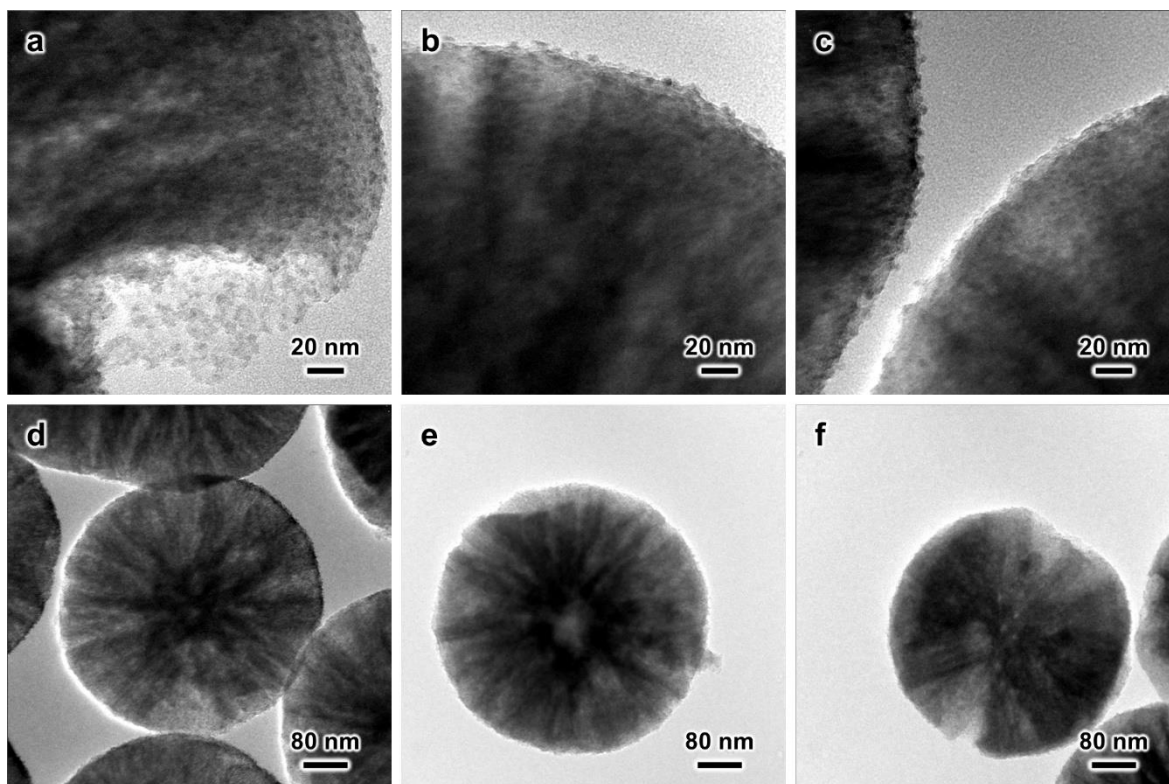


Figure S41. (a-f) TEM images of the spent MSS-Si-4.7Cu-3.2Zn catalyst (Table S1, entry 7).

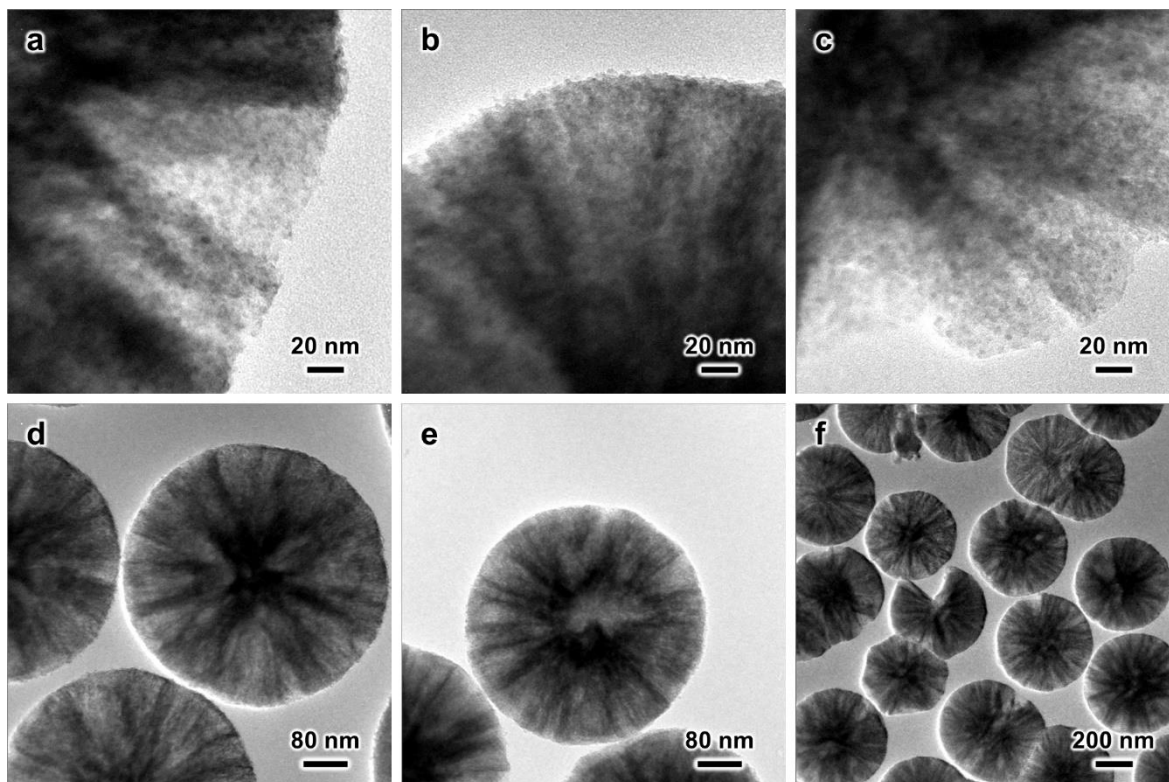


Figure S42. (a-f) TEM images of the spent MSS-Si-4.3Cu-4.6Zn catalyst (Table S1, entry 8).

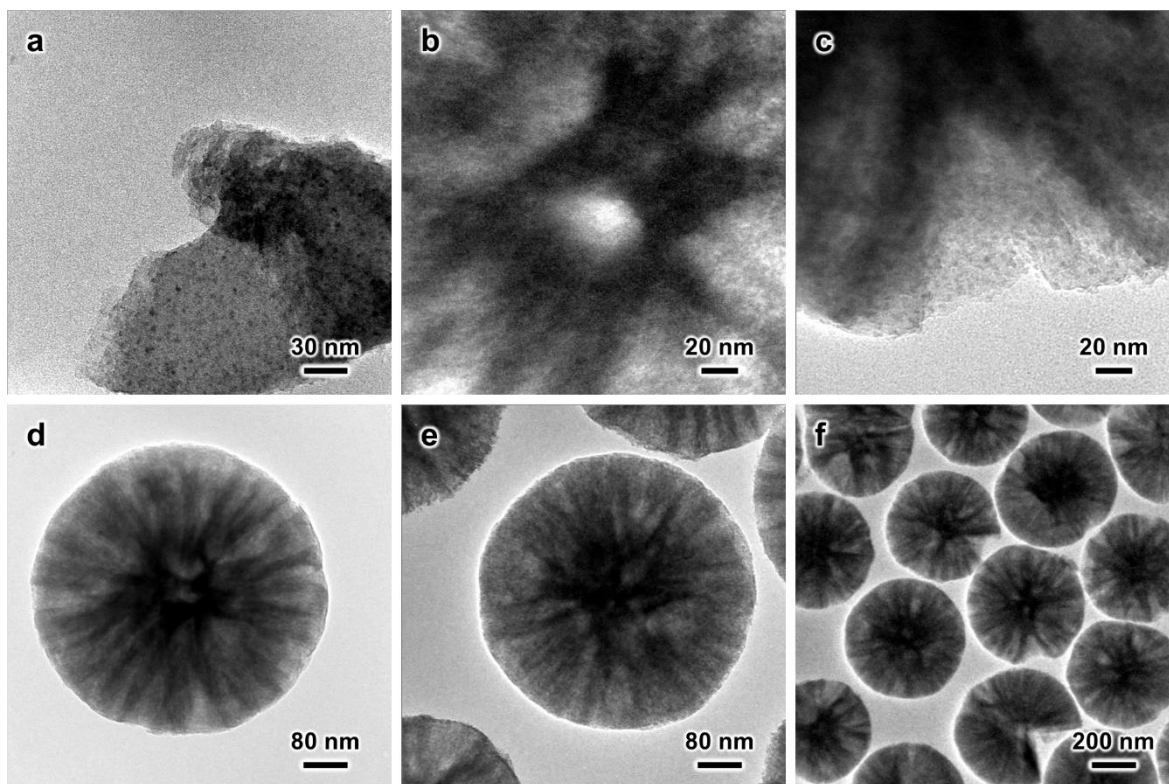


Figure S43. (a-f) TEM images of the spent MSS-Si-3.8Cu-5.5Zn catalyst (Table S1, entry 9).

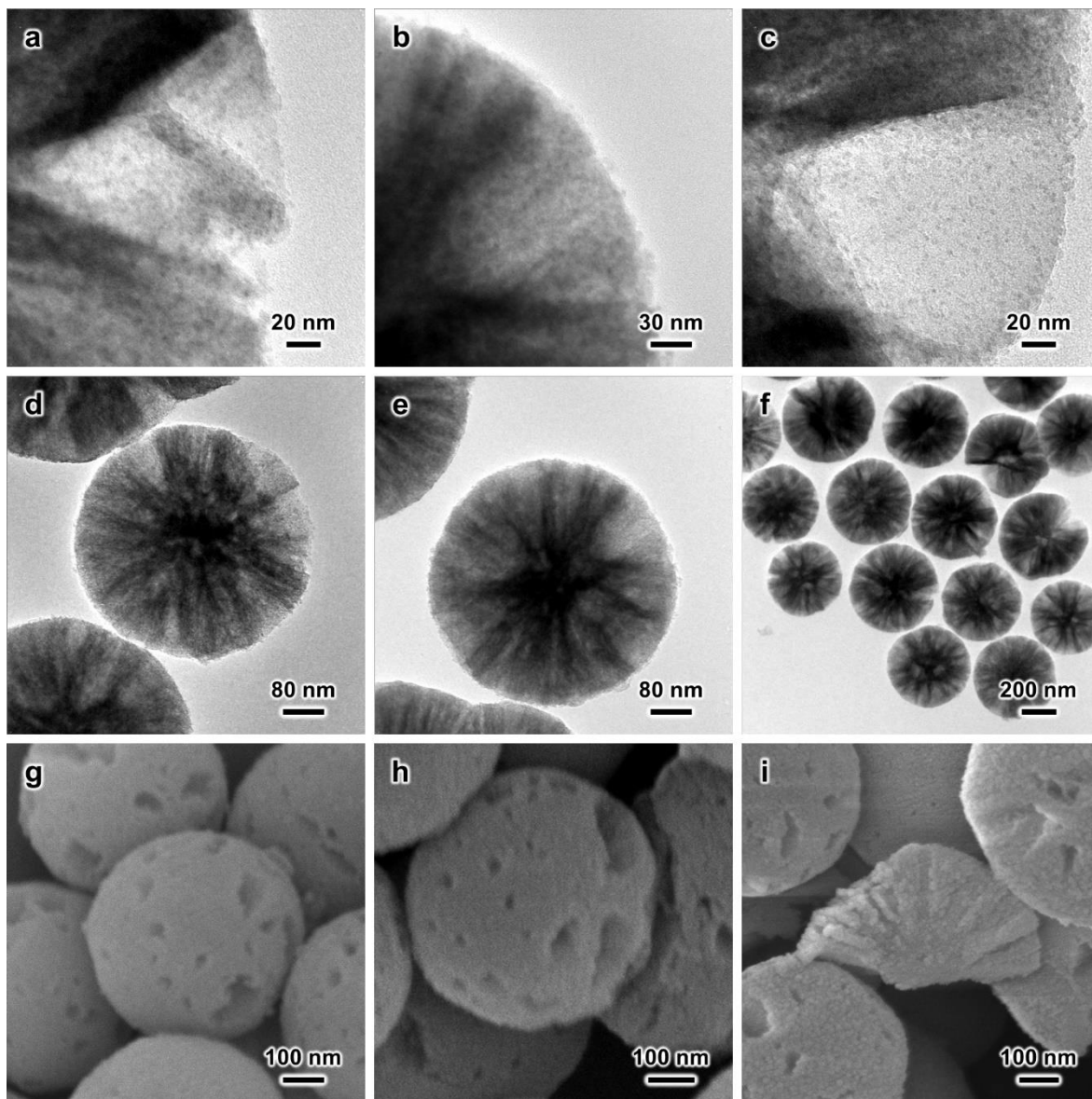


Figure S44. (a-f) TEM and (g-i) FESEM images of the spent MSS-Si-3.2Cu-6.0Zn catalyst (Table S1, entry 10).

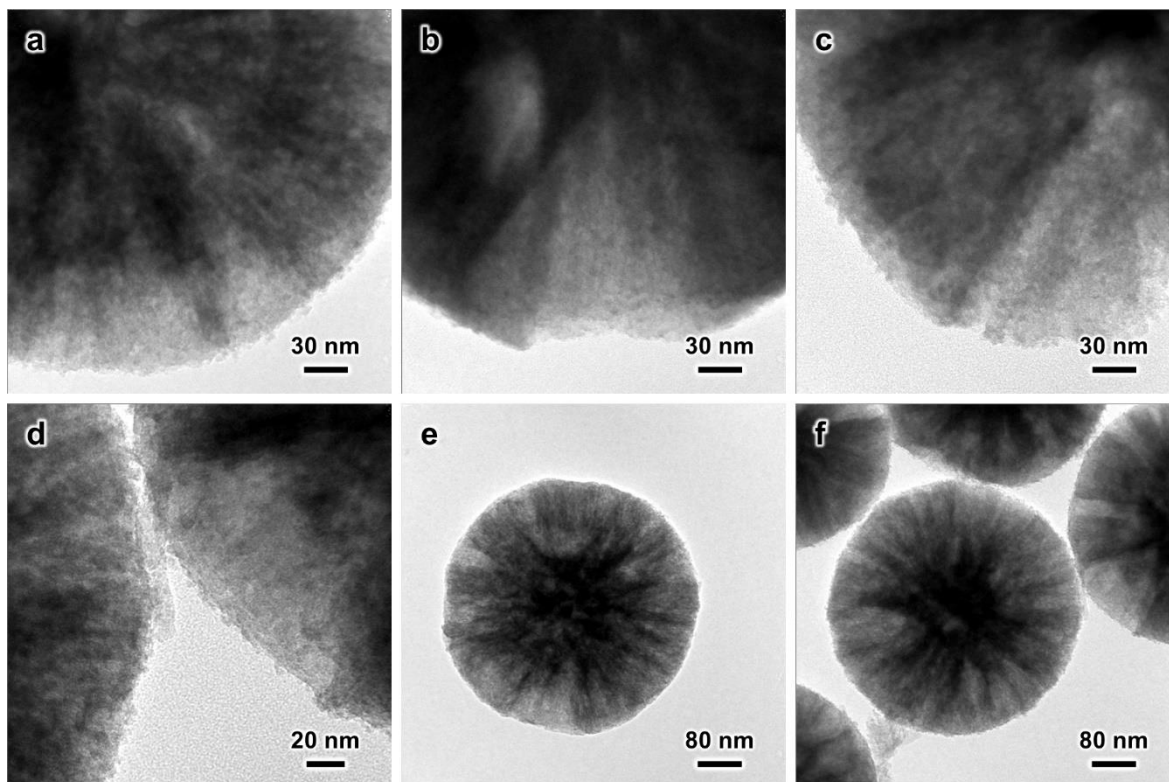


Figure S45. (a–f) TEM images of the spent MSS-Si-2.6Cu-6.7Zn catalyst (Table S1, entry 11).

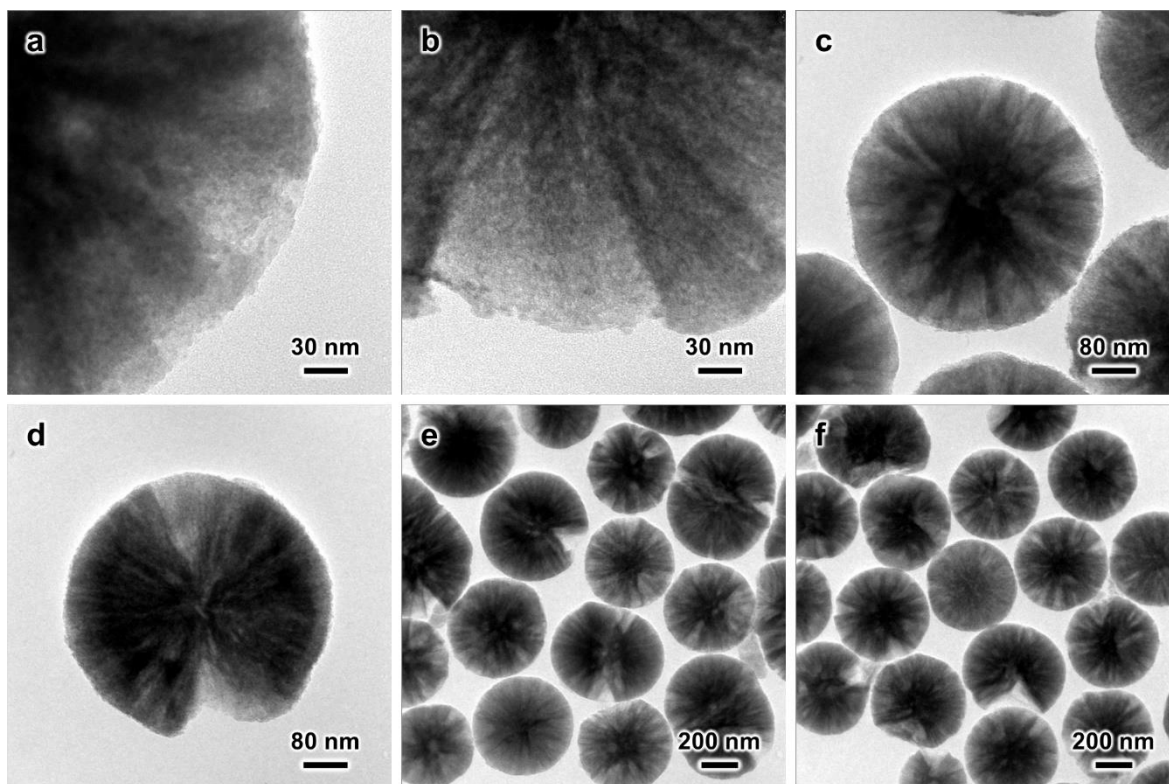


Figure S46. (a–f) TEM images of the spent MSS-Si-2.2Cu-6.7Zn catalyst (Table S1, entry 12).

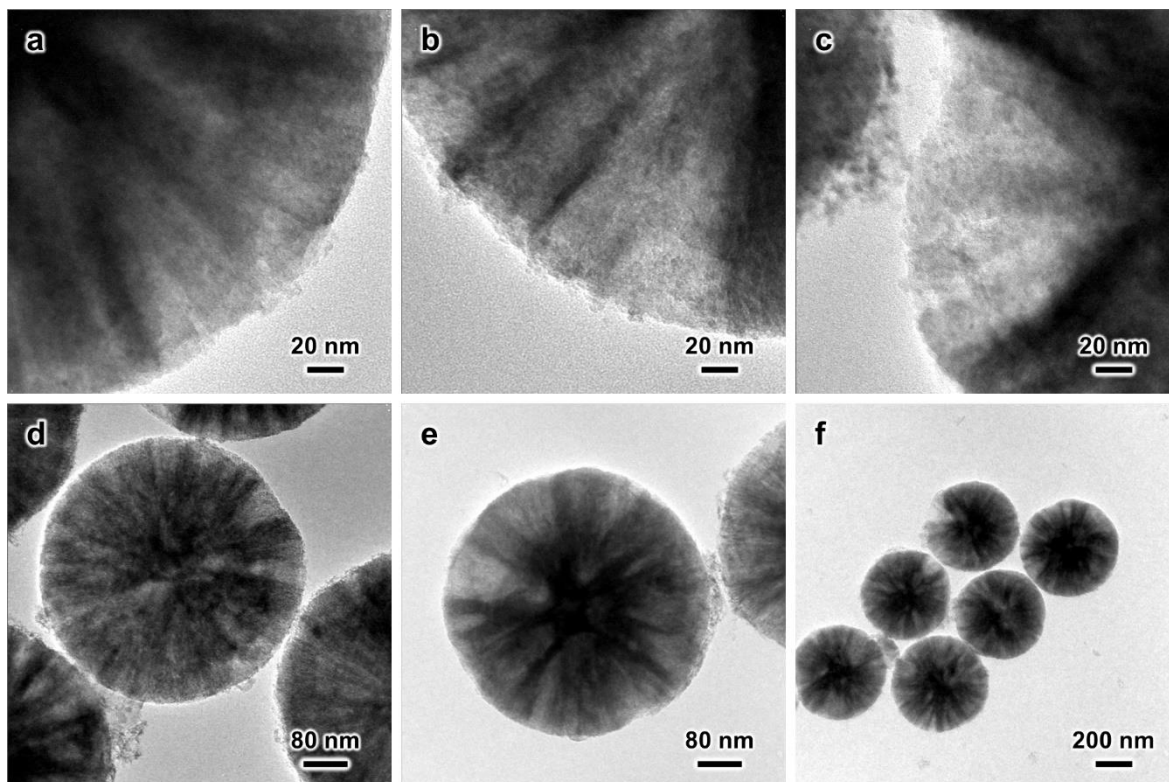


Figure S47. (a-f) TEM images of the spent MSS-Si-2.5Cu-6.1Zn catalyst (Table S1, entry 13).

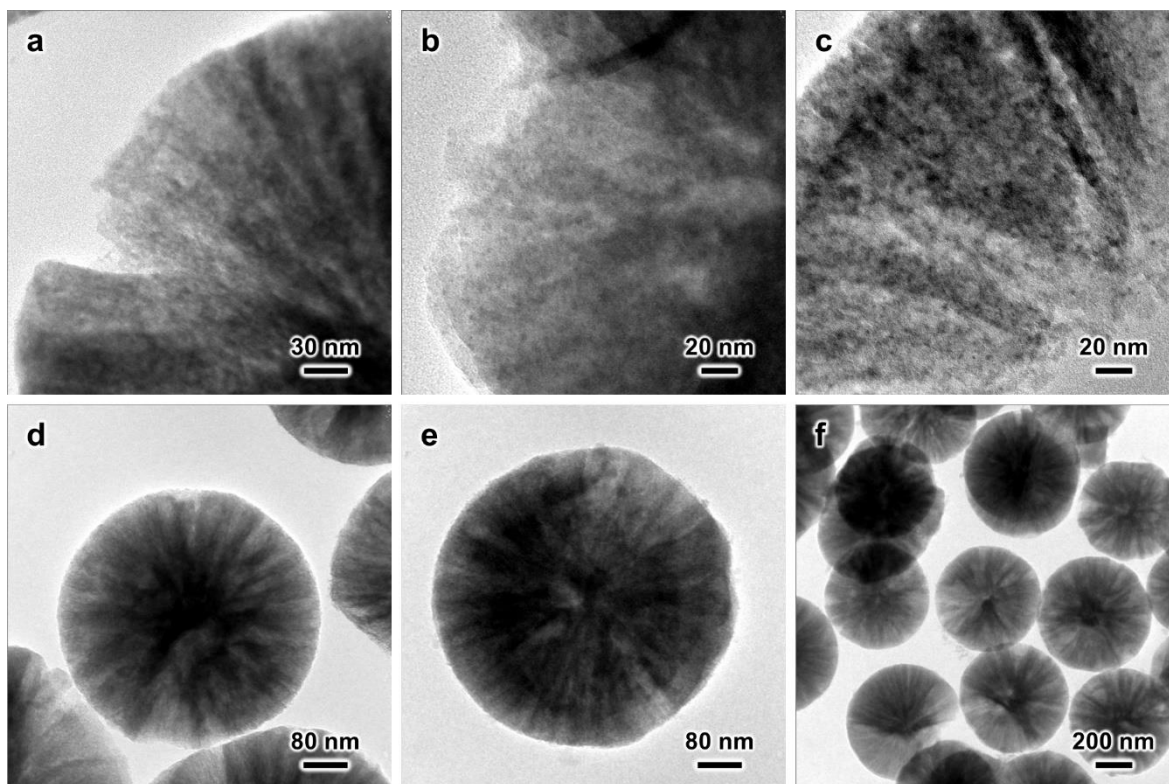


Figure S48. (a-f) TEM images of the spent MSS-Si-2.4Cu-5.3Zn catalyst (Table S1, entry 14).

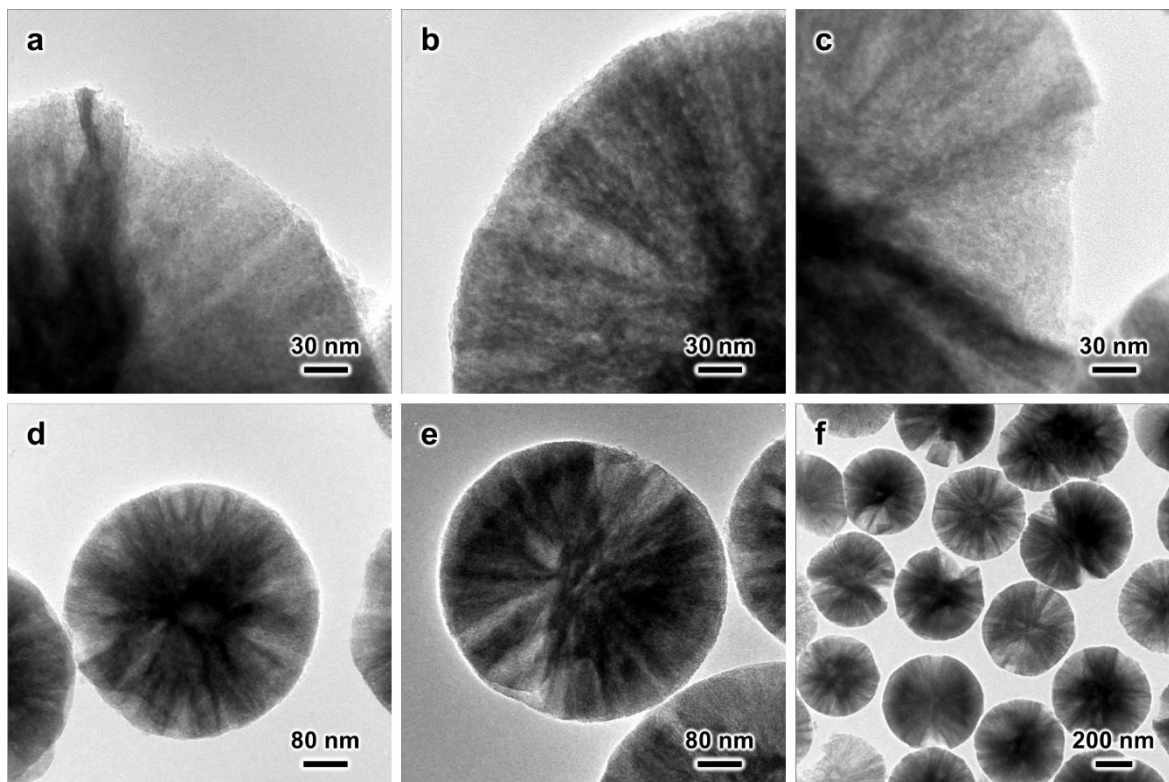


Figure S49. (a–f) TEM images of the spent MSS-Si-4.0Cu-4.2Zn catalyst (Table S1, entry 15).

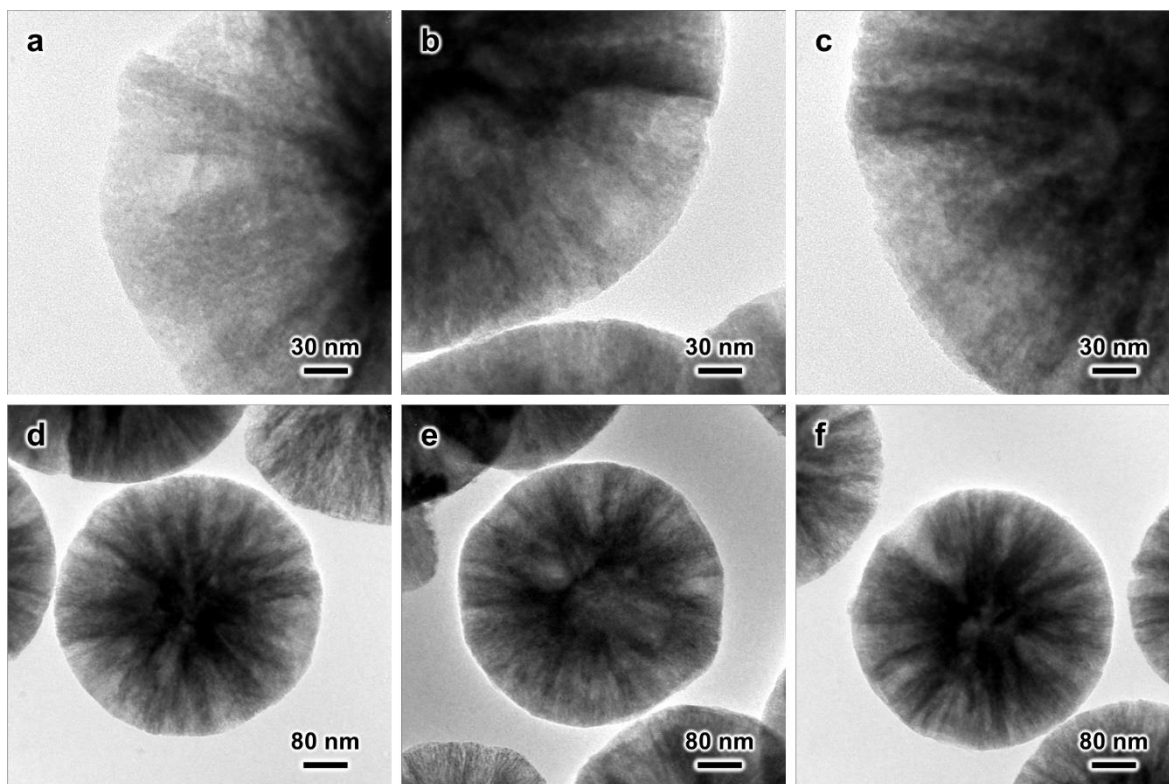


Figure S50. (a–f) TEM images of the spent MSS-Si-4.1Cu-3.5Zn catalyst (Table S1, entry 16).

Comment: Regardless of the Cu and Zn content in the MSS-Si-Cu-Zn catalyst, only small nanoparticles could be observed in the spent catalysts (Figures S40–S50). Recognized by their characteristic lattice fringe patterns, these nanoparticles were identified to be metallic Cu

nanoparticles (high image contrast) and ZnO nanoparticles (low image contrast). No agglomeration of active species was spotted amongst the spent catalysts with various compositions. Besides, the metal nanoparticles show an even distribution, with Cu and ZnO nanoparticles well dispersed and mixed in close vicinity. Along with the close examination of the neighboring Cu and ZnO particles, it is expected such nanoparticle distribution should favor the SMSI.

Moreover, the large mesopore structure was well preserved after the catalytic reaction and no pore blockage was detected (Figure S44i). This further demonstrated the superiority of the MSS support over $m\text{SiO}_2$ support with small mesopores (<5 nm), where the mesopores might be blocked by the metal nanoparticles.

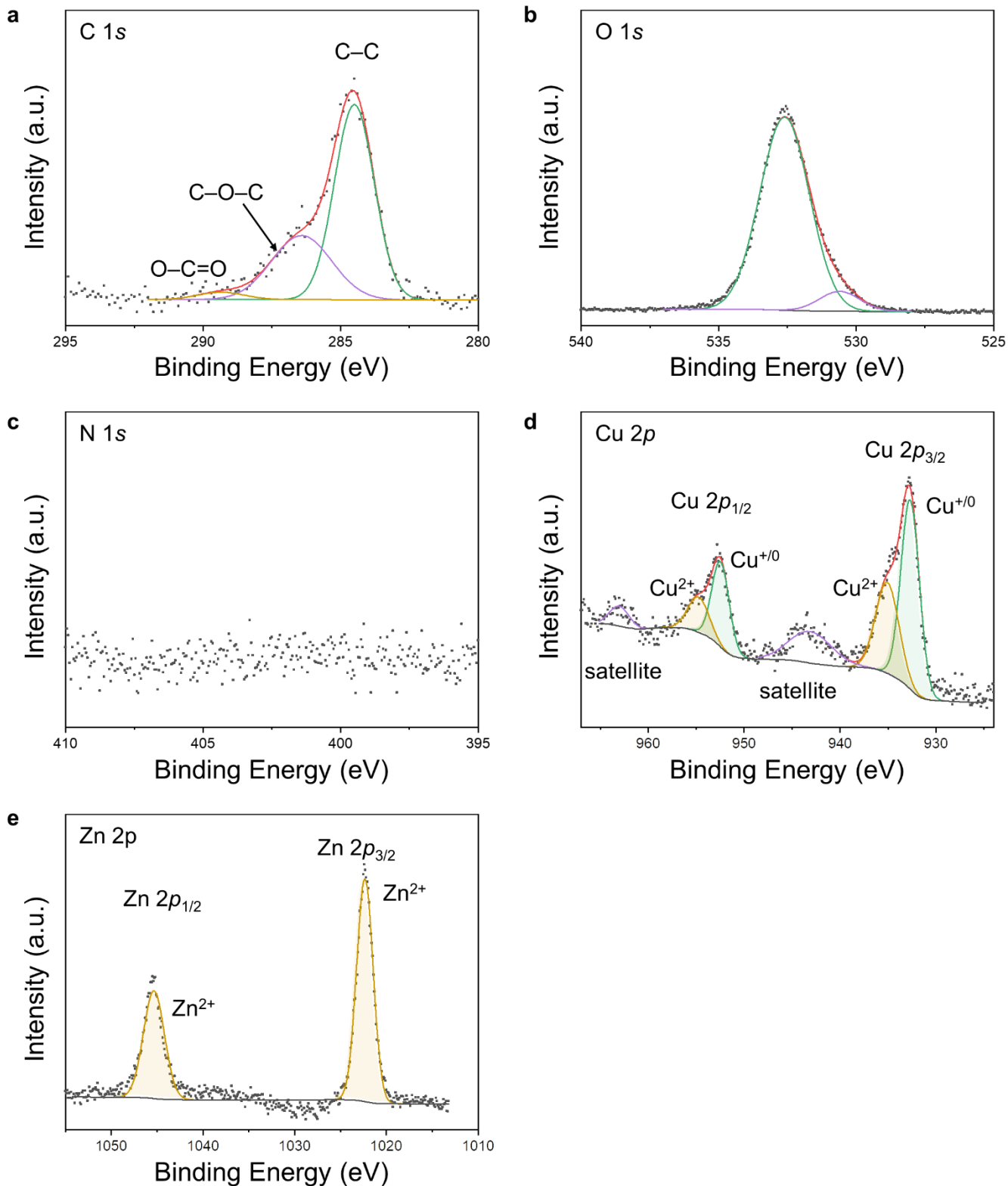


Figure S51. XPS profiles of the spent MSS-Si-Cu-Zn sample in (a) C 1s, (b) O 1s, (c) N 1s, (d) Cu 2p, and (e) Zn 2p regions, respectively.

Comment: The C 1s region of the spent MSS-Si-Cu-Zn sample (Figure S51a) is typical of adventitious carbon contamination, with binding energies of 284.5, 286.4, and 289.4 eV corresponding to C-C, C-O-C, and O-C=O species, respectively.

The O 1s region of the spent MSS–Si–Cu–Zn sample (Figure S51b) is composed of a peak representing SiO₂ (532.6 eV) and a minor peak located at 530.6 eV indicating metal oxides or surface silanol group.

The N 1s signal of the spent MSS–Si–Cu–Zn sample (Figure S51c) is not found, due to the complete removal of alkylamine ligands during the calcination treatment.

The Cu 2p region of the spent MSS–Si–Cu–Zn sample (Figure S51d) shows a component typical of Cu²⁺, with Cu 2p_{3/2} component located at 935.1 eV, with characteristic satellite features. However, another Cu 2p_{3/2} component located at 932.7 eV is attributed to Cu⁺ and/or metallic Cu⁰.

The Zn 2p region of the spent MSS–Si–Cu–Zn sample (Figure S51e) shows a unimodal doublet with Zn 2p_{3/2} located at 1022.4 eV and is representative for ZnO.

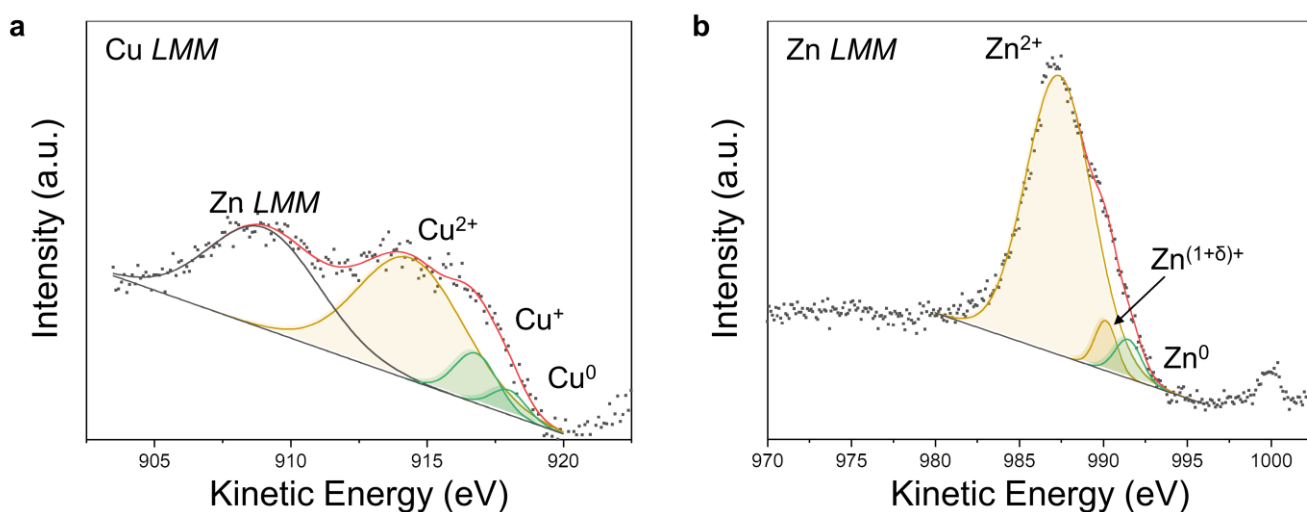


Figure S52. XAES profiles of the spent MSS–Si–Cu–Zn sample in (a) Cu LMM and (b) Zn LMM regions.

Comment: The valence states of Cu and Zn species in MSS–Si–Cu–Zn are further confirmed with XAES technique. The Cu LMM region were deconvoluted into three peaks and they are accordingly assigned to Cu²⁺ species (914.4 eV), Cu⁺ species (916.8 eV), and metallic Cu (918 eV), respectively. The Zn LMM region were deconvoluted into a main peak centered at 987.4 eV typical for Zn²⁺, with a shoulder feature located at 990.1 eV attributed to partially reduced Zn^{(1+δ)+}. Moreover, the minor peak centered at 991.4 eV should represent metallic Zn, incorporated into the Cu edges and steps of the Cu nanoparticles. An additional minor peak emerged at 1000 eV is characteristic for metallic Zn.

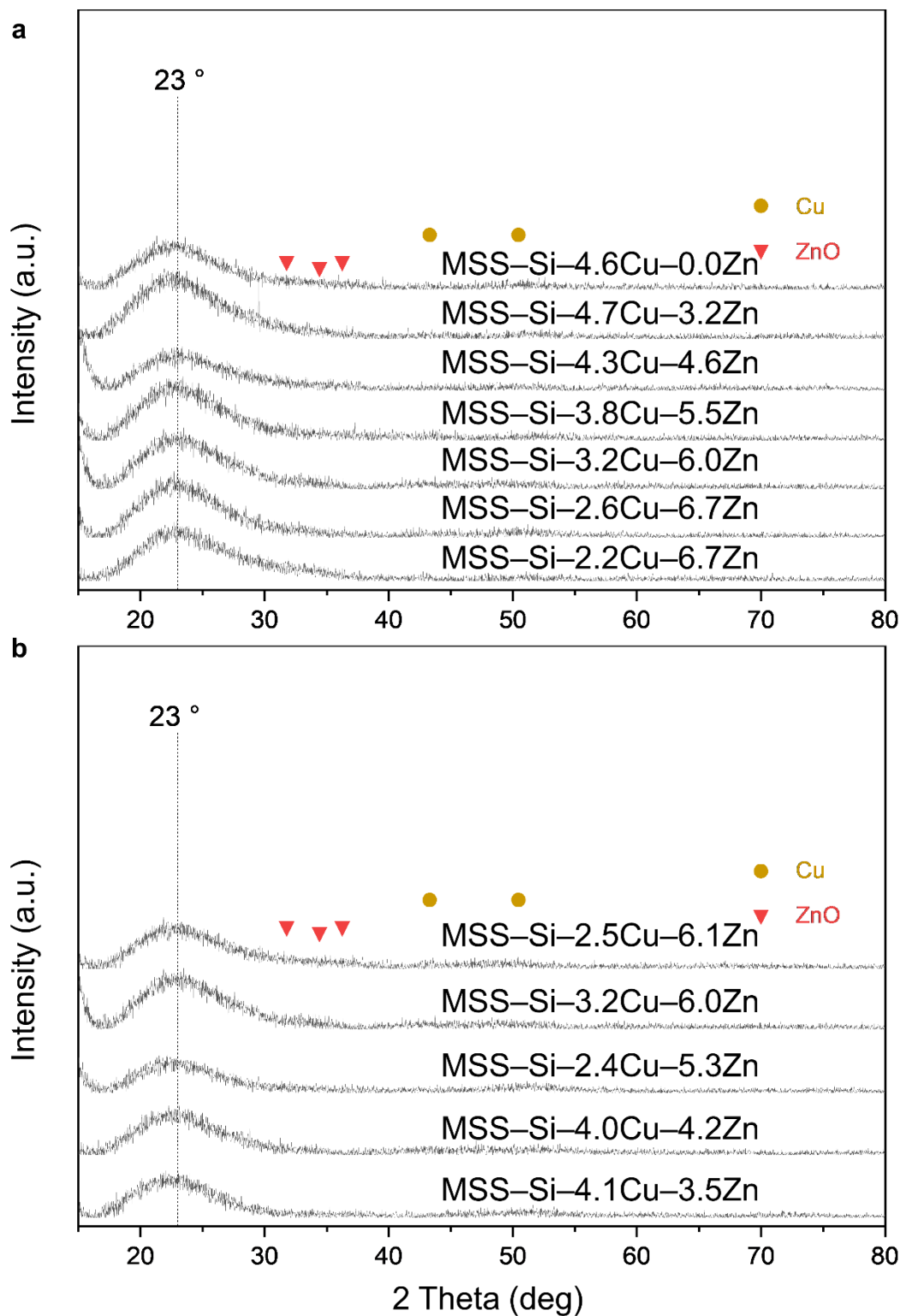


Figure S53. (a, b) XRD profiles of spent MSS-Si-Cu-Zn samples prepared with different amounts of Cu and Zn precursors (Table S1, entries 6–16).

Comment: Similar to our conclusion for Figure S30, the XRD signals due to the MSS support largely cover the signals due to the highly dispersed active phase. Although Cu and ZnO nanoparticles are quite recognizable in the TEM images of the spent catalyst, their XRD reflections cannot be resolved, unlike those in our previous work.

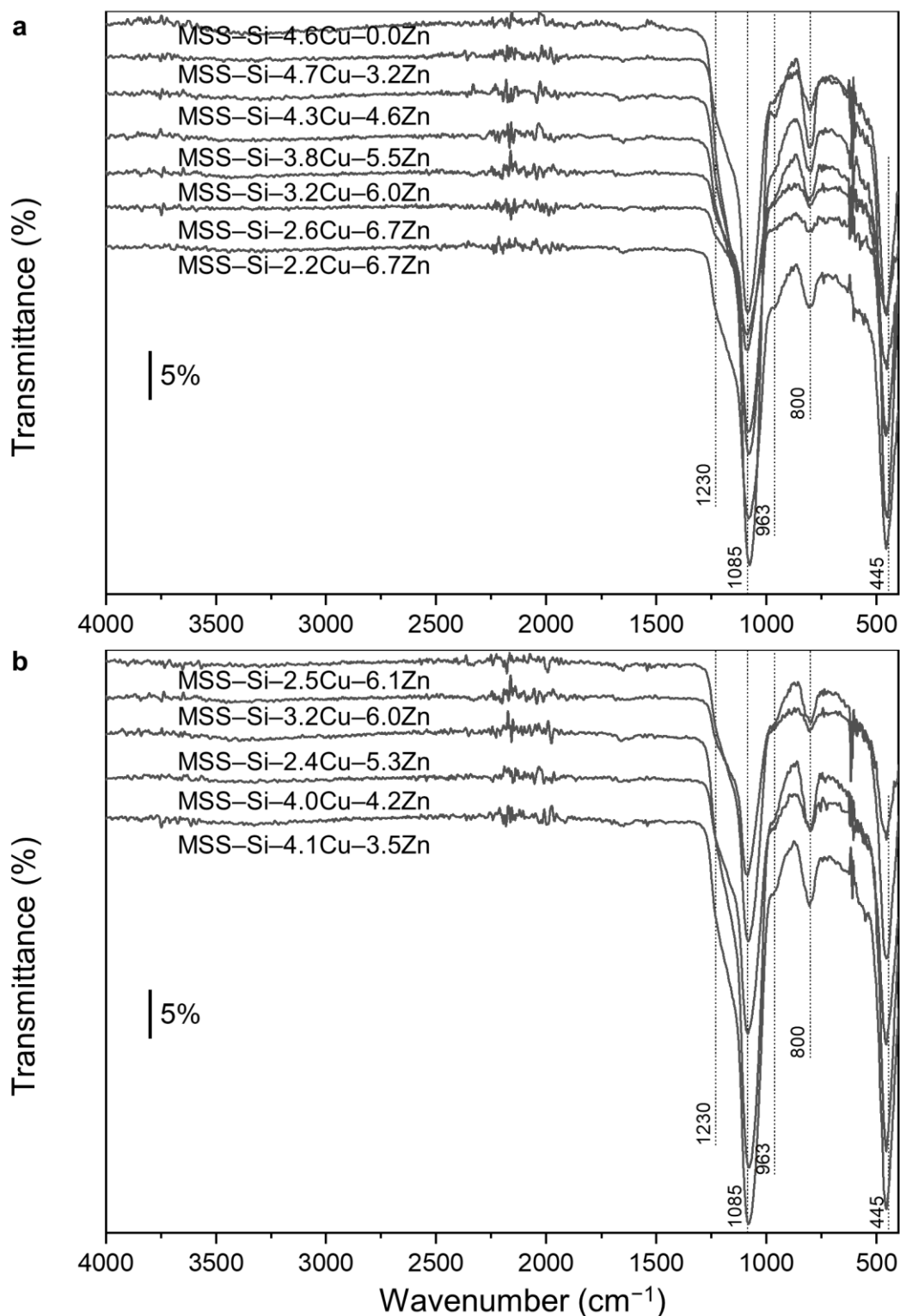


Figure S54. (a, b) FTIR spectra of spent MSS-Si-Cu-Zn samples prepared with different amounts of Cu and Zn precursors (Table S1, entries 6–16).

Comment: Like the conclusion made for Figure S31, only characteristic absorption bands located at 1085 (with a shoulder feature at 1230 cm⁻¹), 963, 800, and 445 cm⁻¹ due to the silica support can be readily identified. These peaks are accordingly assigned to asymmetric and symmetric stretching of Si-O-Si, Si-OH stretching, and Si-O-Si bending, respectively.

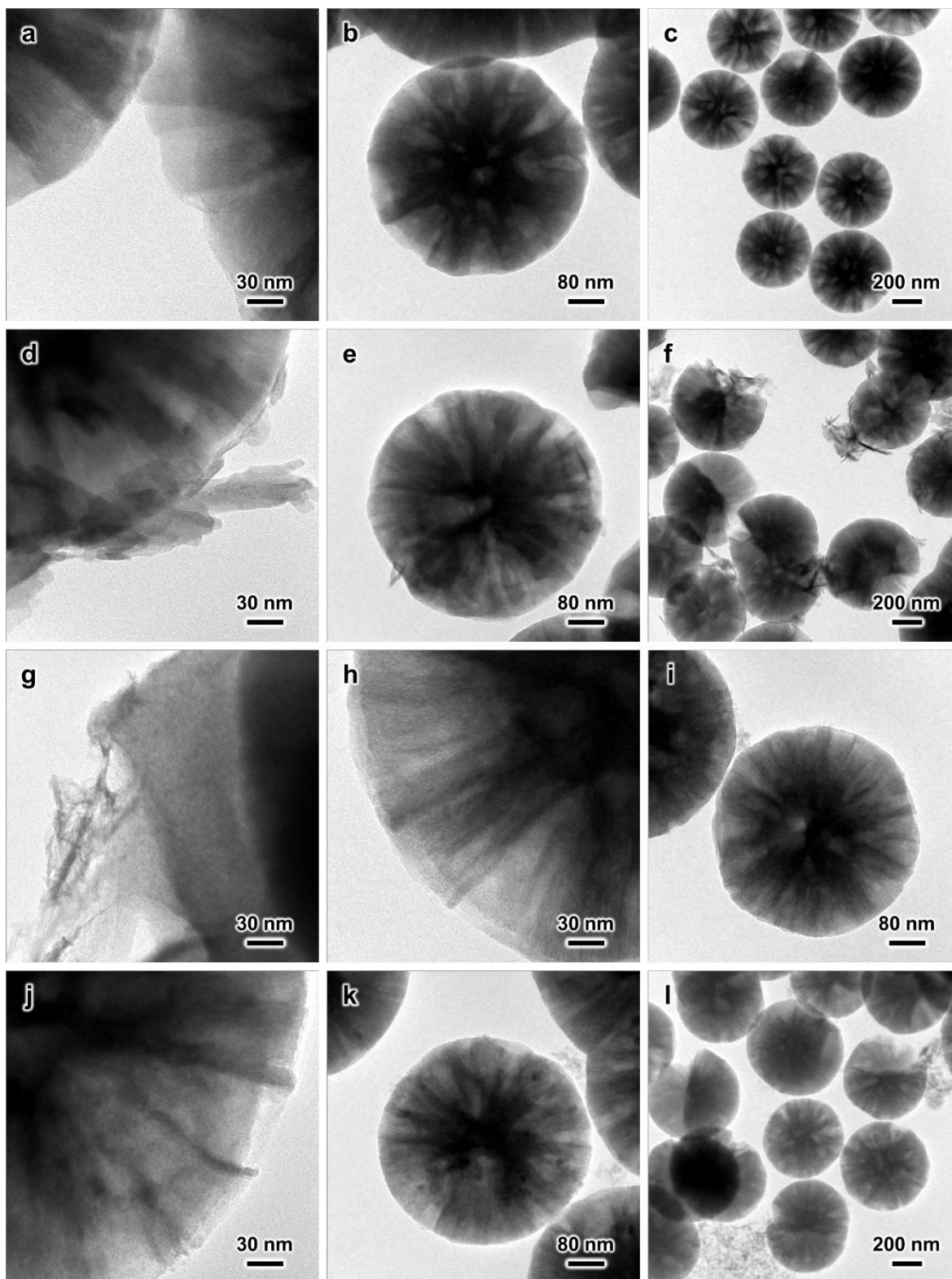


Figure S55. TEM images of (a–c) amine-functionalized MSS-NH₂, (d–f) MSS-NH₂-CuZn with Cu and Zn loaded via incipient wetness impregnation method, (g–i) MSS-CuZn after calcination treatment, and (j–l) spent MSS-CuZn catalyst.

Synthetic Procedures for SiO₂-CuZn and MSS-CuZn:

First, we prepared amine functionalized SiO₂ NS and MSS (SiO₂/MSS-NH₂).¹⁸ In brief, 400 mg of SiO₂/MSS was dispersed into 15 mL of toluene and 1 mL of ethanol, via 15 min of ultrasonication.

520 μL of APTMS was dissolved into the suspension. The mixture was refluxed at 110 $^{\circ}\text{C}$ for 12 h. The product was collected via centrifugation, washed with ethanol twice, and dried in an electric oven at 60 $^{\circ}\text{C}$ overnight.

Second, Cu and Zn were introduced via an incipient wetness impregnation method ($\text{SiO}_2/\text{MSS-NH}_2\text{-CuZn}$).³ In a typical synthesis, 300 mg of the prepared $\text{SiO}_2/\text{MSS-NH}_2$ was dispersed in 1.5 mL of ethanol and 1.5 mL of deionized water inside a 30-cc crucible to form a paste, via 5 min of ultrasonication. Thereafter, $\text{Cu}(\text{NO}_3)_2$ and $\text{Zn}(\text{NO}_3)_2$ solutions were introduced with nominal loadings of 3 wt % Cu and 6 wt % Zn (75 μL of 2 M $\text{Cu}(\text{NO}_3)_2$ aq solution and 277 μL of 1 M $\text{Zn}(\text{NO}_3)_2$ aq solution). The paste was subjected to another 10 min of ultrasonication and dried in an electric oven at 80 $^{\circ}\text{C}$ for several hours.

Lastly, the dried sample was calcined at 500 $^{\circ}\text{C}$ for 4 h in static laboratory air, with a ramp rate of 10 $^{\circ}\text{C}\cdot\text{min}^{-1}$.

Comment: As discussed in Section 3.5, Figure S55 shows the TEM images obtained at different synthetic stages of MSS-CuZn catalyst. The amine surface modification led to no distinguishable change to the surface texture and the original small mesopores and micropores were readily identifiable (Figure S55a-c), hence it is not likely a surface layer was coated via polycondensation of APTMS like that in $\text{MSS-SiRNH}_2\text{-Cu}$. Judged by the TEM images and our previous studies,¹⁵ only the surface composition was altered by grafting with some alkylamine groups and no organosilica shell was formed.

Despite of a relatively low nominal metal loading of 3 wt % Cu and 6 wt % Zn, it still resulted in excess Cu and Zn species in the dried products of the impregnation method (Figure S55d-f). They ended up as nanorods and nanoflakes of metal hydroxides/oxides. Nevertheless, these nanorods/nanoflakes largely disappeared after the calcination treatment. Some of them ended up as nanowire-like mixed oxides while the other Cu and Zn species ended up as a uniform layer of oxide nanoparticles on MSS (Figures 8a, b and S55g-i).

After the CO_2 hydrogenation reaction, the morphology of MSS was well preserved and the active Cu and Zn species ended up in three forms: (i) networked nanowires of Cu/ZnO, (ii) small nanoparticles, and (iii) large nanoparticles (Figures 8c, d and S55j-l). According to our understanding, small nanoparticles should contribute the most to the specific catalyst activity as they have the highest specific surface area, exposed atoms, and defect sites due to their small sizes. The large nanoparticles and nanowires of Cu-ZnO are less desirable in this catalytic application. Therefore, an inferior specific catalytic activity is expected for MSS-CuZn , in comparison to MSS-Si-Cu-Zn , in terms of specific MeOH yield and CO_2 activity (Figure 8e, f).

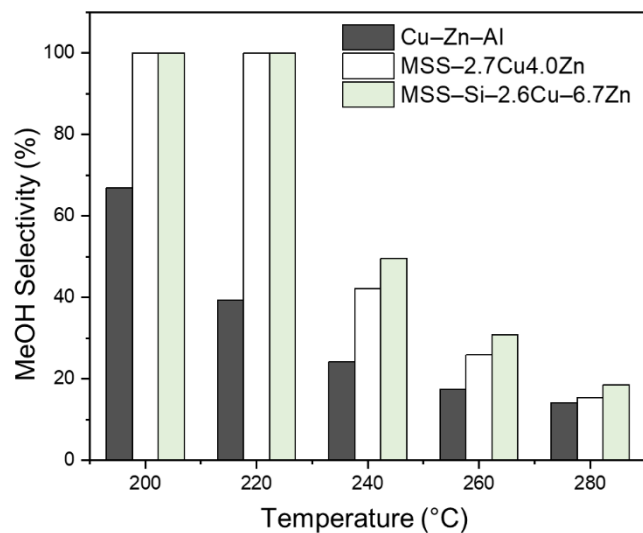


Figure S56. Comparison of MeOH selectivity among commercial catalyst, MSS-CuZn (simple impregnation), and MSS-Si-Cu-Zn (Cu-organosilicate derived).

Comment: In agreement with our TEM observation of the spent catalysts (Figures 7a-h and 8c, d), the smaller Cu-ZnO nanoparticles in MSS-Si-Cu-Zn led to higher MeOH selectivity than MSS-CuZn catalyst prepared by incipient wetness impregnation.

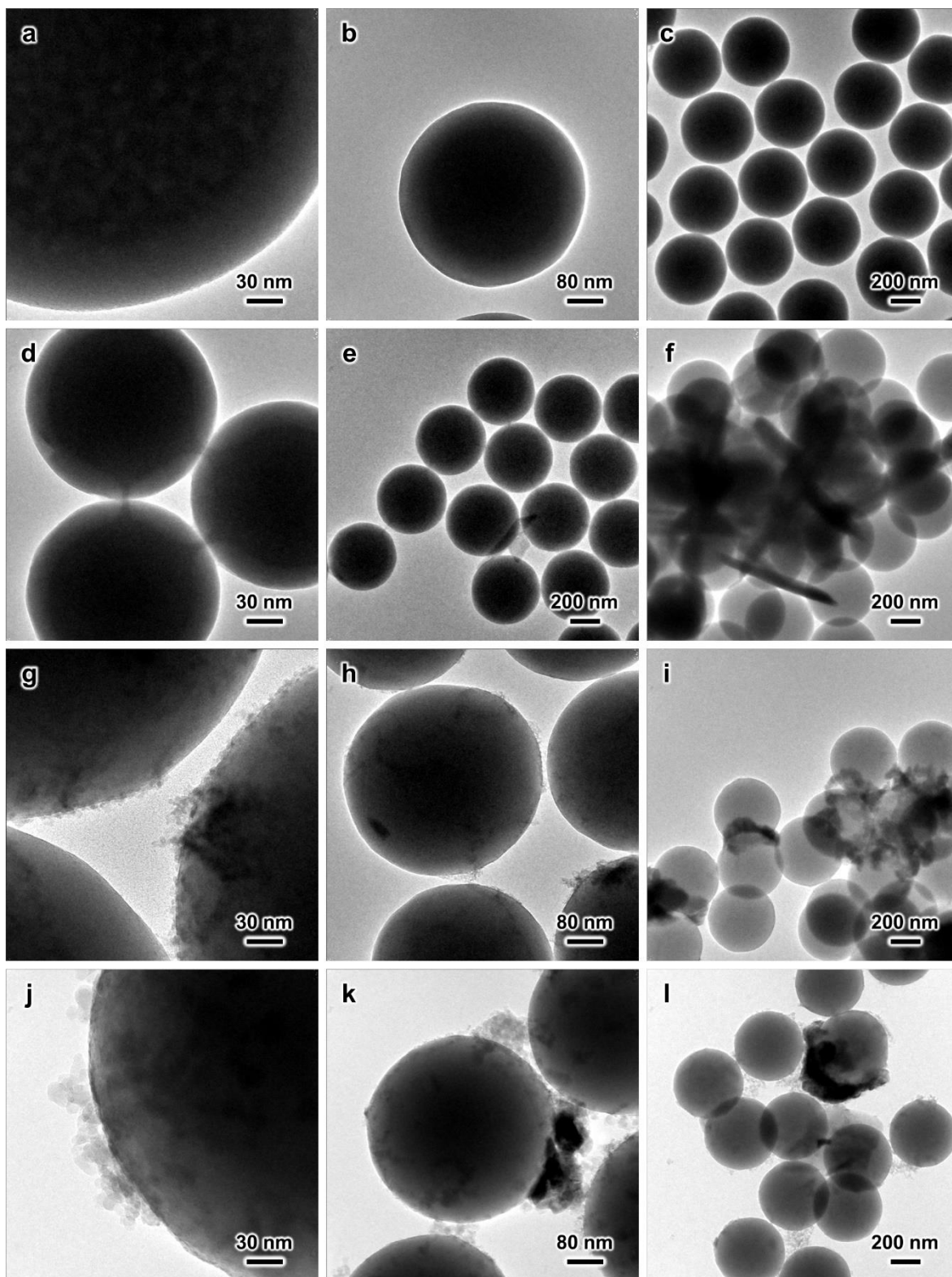


Figure S57. TEM images of (a–c) amine-functionalized $\text{SiO}_2\text{-NH}_2$, (d–f) $\text{SiO}_2\text{-NH}_2\text{-CuZn}$ with Cu and Zn loaded via incipient wetness impregnation method, (g–i) $\text{SiO}_2\text{-CuZn}$ after calcination treatment, and (j–l) spent $\text{SiO}_2\text{-CuZn}$ catalyst.

Comment: As discussed in Section 3.5 and as a complementary study, $\text{SiO}_2\text{-CuZn}$ catalyst was prepared from rigid SiO_2 NS following the same incipient wetness impregnation method. Similar to our observation in Figure S55a–c, the amine surface modification should only alter the surface chemistry but not the surface texture of the support (Figure S57a–c).

After introduction of 3 wt % Cu and 6 wt % Zn via incipient wetness impregnation, oxide nanorods were observed due to the excess amounts of Cu and Zn (Figure S57d–f). However, a larger portion of the metal species ended up as aggregates or oxide nanowires after the calcination treatment (Figure S57g–i), due to the smaller surface area of SiO₂ NS compared to MSS. In addition, large aggregates (>100 nm) of metal oxides were detected.

After CO₂ hydrogenation reaction, the agglomeration of active metal species became more severe and large aggregates >400 nm were found in the TEM images (Figure S57j–l). According to our understanding, these large aggregates are detrimental to the catalytic activity.

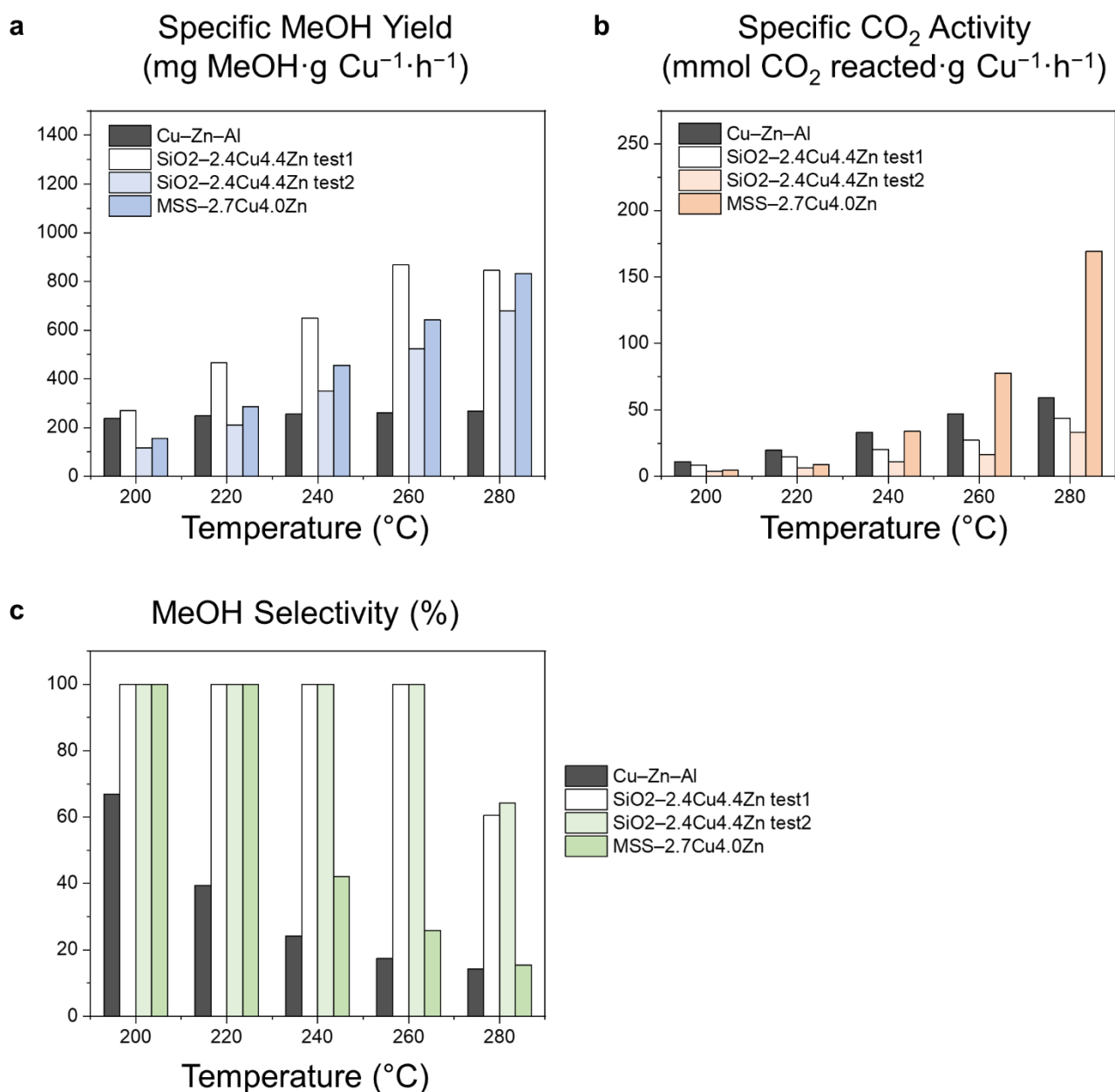


Figure S58. Catalytic performance of commercial catalyst, SiO₂-CuZn (simple impregnation), and MSS-CuZn (simple impregnation). (a) Cu-specific MeOH yield. (b) MeOH selectivity. (c) Cu-specific CO₂ activity.

Experimental Procedure: The SiO₂-CuZn catalyst was tested according to procedures described in Section 2.7 except that it was operated at each temperature (200–280 °C, 20 °C steps) for only *ca.*

40 min before switching to another temperature to obtain results denoted as “test1”. The catalyst was then operated at 280 °C for 3 h. Thereafter, the reactor was depressurized and cooled down to ambient temperature. The reactor was purged with N₂ until no reactant or product signal was detectable by GC. The same procedure (Section 2.7) was then repeated to obtain results denoted as “test2”.

Comment: As discussed in Section 3.5 and Figure S57 above, the large metal aggregates observed in the TEM images of calcined and spent SiO₂-CuZn are unfavorable for good catalytic performance. Interestingly, the SiO₂-CuZn initially displayed higher specific MeOH yield than MSS-CuZn (Figure S58a test1). However, the catalytic activity drastically declined during the operation. Therefore, we quickly captured the initial catalytic performance and performed the reaction again to obtain data when the performance stabilized (Figure S58a test2, see experimental procedure above). The stabilized specific MeOH yield of SiO₂-CuZn was lower than that of MSS as expected. Moreover, the specific CO₂ activity of SiO₂-CuZn was significantly lower than that of MSS-CuZn for both tests (Figure S58b). The MeOH selectivity was less informative as the CO production from SiO₂-CuZn catalyzed reaction was so low that fell below the GC detection/integration limit and hence could not be captured correctly (Figure S58c). This catalyst showcased the rapid decline of catalytic activity due to the low stability of impregnation derived CuZn catalysts.

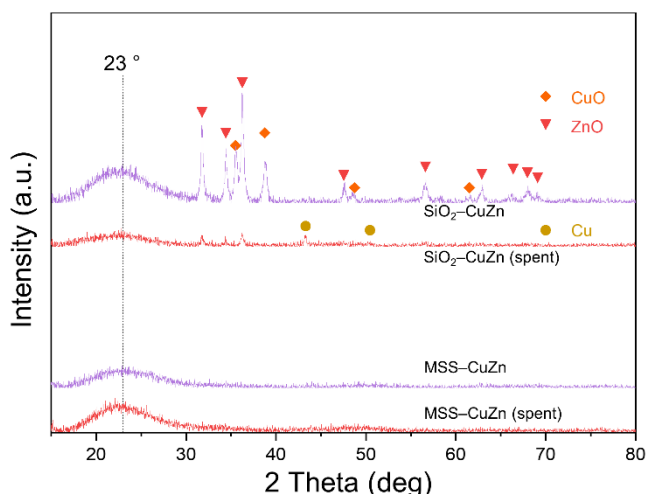


Figure S59. XRD profiles of the fresh and spent SiO₂-CuZn and MSS-CuZn catalysts (both prepared with simple impregnation).

Comment: The XRD patterns of the fresh and spent SiO₂-CuZn and MSS-CuZn catalysts further corroborate the TEM observations. Unlike what we observed in other samples (Figure S30), strong reflections peaks corresponding to CuO and ZnO phase are detected in the calcined SiO₂-CuZn sample. The signals became less evident in the spent SiO₂-CuZn catalyst, with the CuO peaks diminished and metallic Cu peaks emerged. On the other hand, for the calcined and spent MSS-CuZn sample, none of the characteristic reflections could be identified due to the better dispersion of the active phase.

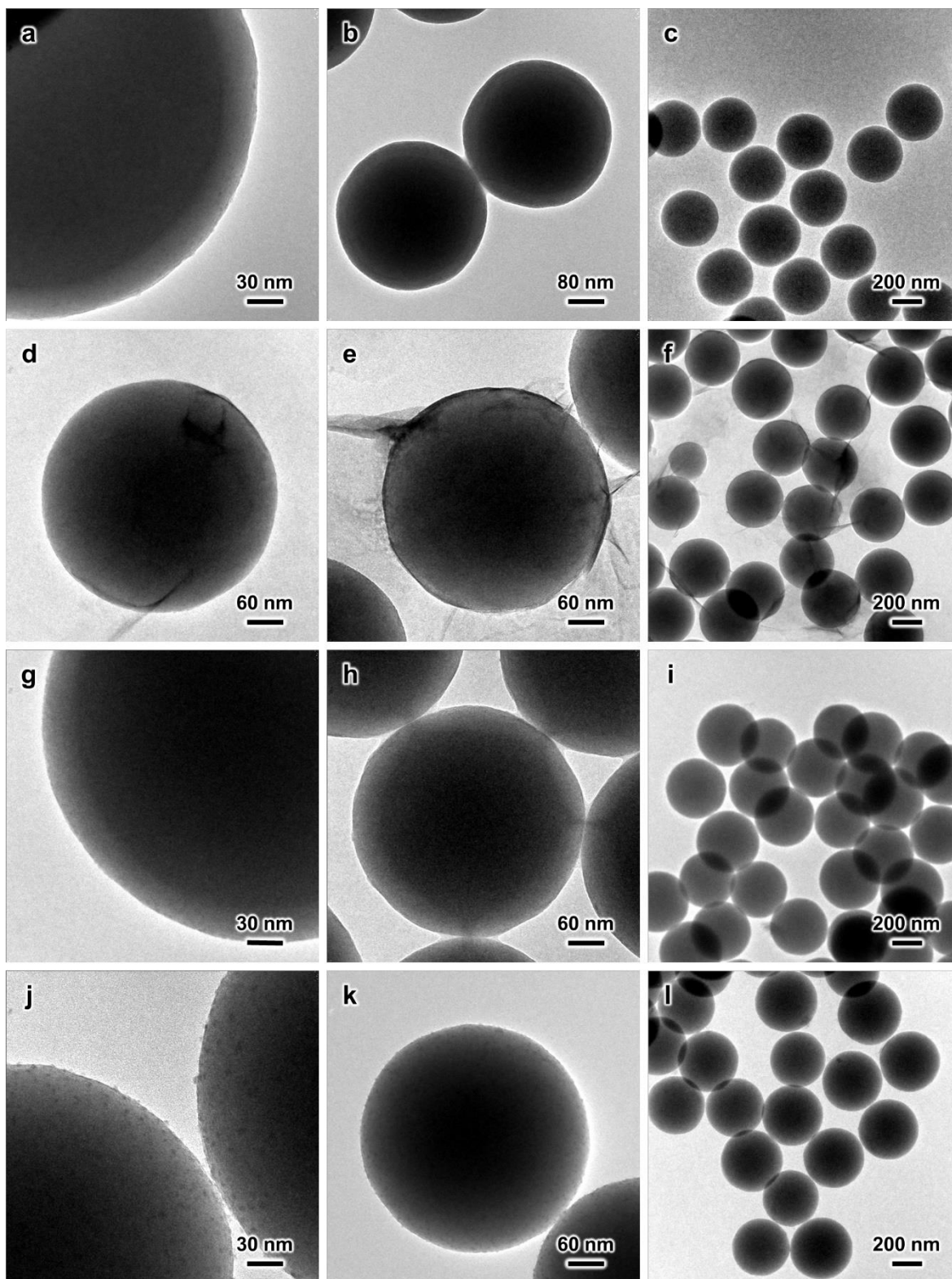


Figure S60. TEM images of (a–c) $\text{SiO}_2\text{-SiRNH}_2\text{-Cu}$ prepared following protocol C (**Figure S6**), (d–f) $\text{SiO}_2\text{-SiRNH}_2\text{-Cu-Zn}$, (g–i) $\text{SiO}_2\text{-Si-Cu-Zn}$, and (j–l) spent $\text{SiO}_2\text{-Si-Cu-Zn}$.

Synthetic Procedure of $\text{SiO}_2\text{-SiRNH}_2\text{-Cu}$: Please refer to *Protocol C* in the discussion of Figure S6.

Synthetic Procedure of $\text{SiO}_2\text{-SiRNH}_2\text{-Cu-Zn}$: A modified procedure of Section 2.4 was followed, except that 1200 mg of 0.74 wt % Cu $\text{SiO}_2\text{-SiRNH}_2\text{-Cu}$ was used instead of 200 mg of 4.5 wt % Cu MSS- $\text{SiRNH}_2\text{-Cu}$ in the synthesis. 1200 mg of the synthesized $\text{SiO}_2\text{-SiRNH}_2\text{-Cu}$ sample was

dispersed into 40 mL of deionized water via 15 min of ultrasonication. 750 mg of $\text{Zn}(\text{NO}_3)_2 \cdot 6\text{H}_2\text{O}$ was dissolved into the suspension in a 80 mL Teflon liner. The mixture was then sealed in an autoclave and heat treated at 80 °C for 6.5 h. The product was collected via centrifugation, washed with ethanol twice, and dried in an electric oven at 60 °C overnight.

Synthetic Procedure of $\text{SiO}_2\text{-Si-Cu-Zn}$: The $\text{SiO}_2\text{-SiRNH}_2\text{-Cu-Zn}$ prepared above was ground into fine powder and calcined at 500 °C for 2 h in static laboratory air, with a ramp rate of 3 °C·min⁻¹.

Comment: As discussed in Section 3.1 and Figure S6, we prepared $\text{SiO}_2\text{-SiRNH}_2\text{-Cu}$ with a modified synthetic procedure. A shell of the $\text{SiRNH}_2\text{-Cu}$ was coated and the surface in general appeared smooth, while some *ca.* 5 nm nodes could be ambiguously observed (Figure S60a-c).

When introducing Zn species via heat treatment, the excess Zn formed hydroxide/oxide nanosheets instead of ZnO nanoparticles on the external surfaces (Figure S60d-f). Nevertheless, these nanosheets disappeared after the calcination treatment and similar to that in MSS-Si-Cu-Zn , the ZnO species became better dispersed and more amorphous (Figure S60g-i).

After the CO_2 hydrogenation reaction, the Cu and Zn active phase ended up as small nanoparticles like what we observed in spent MSS-Si-Cu-Zn samples (Figure S60j-l).

Based on these observations, we may conclude that MSS-Si-Cu-Zn and $\text{SiO}_2\text{-Si-Cu-Zn}$ catalysts have the identical active phase but different support. As a result, we could make reasonable comparison between the two supports with different morphology in Section 3.6.

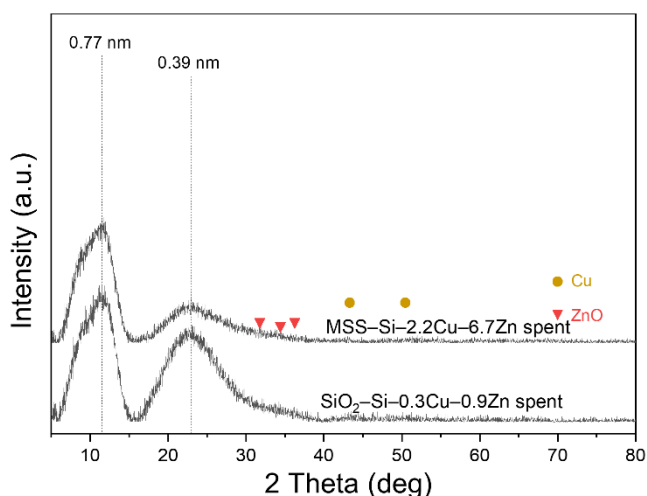


Figure S61. XRD profiles of the spent MSS-Si-Cu-Zn and $\text{SiO}_2\text{-Si-Cu-Zn}$ (both prepared with Cu-organosilicate method).

Comment: Similar to our observation in Figure S53, only a broad reflection of amorphous silica could be identified and the characteristic peaks of expected ZnO and Cu phase could not be found due to their high dispersion and crystallinity.

References

1. H. Yang, P. Gao, C. Zhang, L. Zhong, X. Li, S. Wang, H. Wang, W. Wei and Y. Sun, *Catal. Commun.*, 2016, **84**, 56-60.
2. Y. Jiang, H. Yang, P. Gao, X. Li, J. Zhang, H. Liu, H. Wang, W. Wei and Y. Sun, *J. CO₂ Util.*, 2018, **26**, 642-651.

3. M. Kosari, U. Anjum, S. Xi, A. M. H. Lim, A. M. Seayad, E. A. J. Raj, S. M. Kozlov, A. Borgna and H. C. Zeng, *Adv. Funct. Mater.*, 2021, **31**, 2102896.
4. O. Tursunov, L. Kustov and Z. Tilyabaev, *J. Taiwan Inst. Chem. Eng.*, 2017, **78**, 416-422.
5. Y. Sheng and H. C. Zeng, *Chem. Mater.*, 2015, **27**, 658-667.
6. R.-P. Ye, Y. Chen, T. R. Reina, Z. Cao, T. Xu, X. Chen, Y. Jin, X. L. Zhang and J. Liu, *Adv. Energy Sustainability Res.*, 2021, **2**, 2100082.
7. K. Stangeland, H. H. Navarro, H. L. Huynh, W. M. Tucho and Z. Yu, *Chem. Eng. Sci.*, 2021, **238**, 116603.
8. E. Lam, G. Noh, K. Larmier, O. V. Safonova and C. Copéret, *J. Catal.*, 2021, **394**, 266-272.
9. N. J. Divins, D. Kordus, J. Timoshenko, I. Sinev, I. Zegkinoglou, A. Bergmann, S. W. Chee, S. Widrinna, O. Karslioglu, H. Mistry, M. Lopez Luna, J. Q. Zhong, A. S. Hoffman, A. Boubnov, J. A. Boscoboinik, M. Heggen, R. E. Dunin-Borkowski, S. R. Bare and B. R. Cuenya, *Nat. Commun.*, 2021, **12**, 1435.
10. J. Yu, M. Yang, J. Zhang, Q. Ge, A. Zimina, T. Pruessmann, L. Zheng, J.-D. Grunwaldt and J. Sun, *ACS Catal.*, 2020, **10**, 14694-14706.
11. J. Gao, P. E. Boahene, Y. Hu, A. Dalai and H. Wang, *Catalysts*, 2019, **9**, 922.
12. B. Li and H. C. Zeng, *Chem. Mater.*, 2019, **31**, 5320-5330.
13. D. M. Grant and R. Kollrack, *J. Inorg. Nucl. Chem.*, 1961, **23**, 25-29.
14. J. Bjerrum, C. J. Ballhausen, C. K. Jørgensen and N. A. Sørensen, *Acta Chem. Scand.*, 1954, **8**, 1275-1289.
15. Y. Shao, M. Kosari, S. Xi and H. C. Zeng, *ACS Catal.*, 2022, **12**, 5750-5765.
16. S. Zander, E. L. Kunkes, M. E. Schuster, J. Schumann, G. Weinberg, D. Teschner, N. Jacobsen, R. Schlögl and M. Behrens, *Angew. Chem. Int. Ed.*, 2013, **52**, 6536-6540.
17. S. Natesakhawat, J. W. Lekse, J. P. Baltrus, P. R. Ohodnicki, B. H. Howard, X. Deng and C. Matranga, *ACS Catal.*, 2012, **2**, 1667-1676.
18. B. Xi, Y. C. Tan and H. C. Zeng, *Chem. Mater.*, 2015, **28**, 326-336.